The Dissertation Committee for Kwang Seok Lee certifies that this is the approved version of the following dissertation:

WATER-DISPERSIBLE, CONDUCTIVE POLYANILINE FOR ORGANIC THIN-FILM ELECTRONICS

Committee:

Yueh-Lin Loo, Supervisor

Issac C. Sanchez, Supervisor

Ananth Dodabalapur

Brian A. Korgel

Keith J. Stevenson

C. Grant Willson

WATER-DISPERSIBLE, CONDUCTIVE POLYANILINE FOR ORGANIC THIN-FILM ELECTRONICS

by

Kwang Seok Lee, B.S.; M.S.

Dissertation

Presented to the Faculty of the Graduate School of
The University of Texas at Austin
in Partial Fulfillment
of the Requirements
for the Degree of

Doctor of Philosophy

The University of Texas at Austin
December 2007

Dedication

To my family.

Acknowledgements

I am very grateful to all those people who have helped me to complete the thesis. First, I would like to thank my advisor, Lynn, for her support from the first day in her group until now. Not only her encouragement but also criticism has enabled me to envision the big picture of science. I would like to thank former and current group members, Dr. Kimberly Dickey and Reken Patel for fruitful discussion about device fabrication and characterization, Dmitry Krapchetov for his help with NEXAFS and FTIR experiment, Joung Eun Yoo for providing me PANI-PAAMPSA, and Tracy Bulcholz and Kyle Guice for having discussions with me about materials chemistry.

I would like to acknowledge all the collaborators who have contributed to work presented in this thesis. Special thanks to Dr. Keith Stevenson and Timothy Smith for helping me with SSPM measurements and Dr. Chris Zangmeister for helping me with UPS experiments. I am grateful to Drs. Graciela Blanchet, Feng Gao, and Hong Meng for providing me the materials used in my research. I am also grateful to Dr. Yangming Sun for having fruitful discussion about our XPS results.

I would like to thank Drs. Ananth Dodabalapur, Brian Korgel, Keith Stevenson, and Grant Willson for providing me guidelines to my research as my committee members and for allowing me to use their facilities for my research.

I would also like to thank my family in Korea for their unconditional love and prayers for me. I am deeply indebted my lovely wife, Jinhee, who has been always supportive and positive from the day I decided to study in the U.S. Without her beside me, I could not have made it through my study in the U.S.

Finally, I would like to thank Il-Ju Academic Foundation in Korea of Overseas Graduate Student Fellowship. I would also like to thank these funding agencies: the DuPont Young Professor Grant, the Camille and Henry Dreyfus New Faculty Award, the National Science Foundation (DMR 0314707), Ricoh Innovations and the Beckman Young Investigator Award.

WATER-DISPERSIBLE, CONDUCTIVE POLYANILINE FOR ORGANIC THIN-FILM ELECTRONICS

Publication No._____________

Kwang Seok Lee, PhD
The University of Texas at Austin, 2007

Supervisors: Yueh-Lin Loo and Issac C. Sanchez

Water-dispersible, conductive polyaniline is an attractive candidate for organic thin-film electronics due to its solution-processability which facilitates low-cost processing. The successful incorporation of water-dispersible, conductive polyaniline into organic electronic applications relies on the development of proper processing techniques for material deposition and the elucidation of how processing conditions affect structural development and macroscopic properties of the material. This thesis focuses on understanding the processing-structure-property relationships of a water-dispersible, conductive polyaniline that is doped with poly(2-acryl-amido-2-methyl-1-propanesulfonic acid), or PANI-PAAMPSA. Such understanding has facilitated the incorporation of PANI-PAAMPSA into functional organic thin-film transistors (TFTs).

We have developed simple, direct patterning techniques by exploiting the wetting and adsorption characteristics of PANI-PAAMPSA. Conductive PANI-PAAMPSA features can be selectively patterned in the hydrophilic regions on a molecular template.

Conductive PANI-PAAMPSA features, which are directly patterned on insulating substrates, can be used as functional electrical components immediately after patterning. PANI-PAAMPSA features as small as 5μm can be routinely created with average electrical conductivity of 0.2S/cm.

The patterned PANI-PAAMPSA features effectively function as source and drain electrodes in pentacene thin-film transistors (TFTs). Specifically, bottom-contact pentacene TFTs with PANI-PAAMPSA electrodes exhibit an average mobility of 0.2cm^2/V-s and on/off current ratios of 10^4, which are on par with the requirements for backplane circuits for driving display applications. In bottom-contact devices, PANI-PAAMPSA makes efficient electrical contact to pentacene by promoting growth of continuous pentacene grains across the channel/electrode interface. Pentacene at such an interface adopts upright orientation, i.e., the fused rings of pentacene are oriented perpendicular to the surface, which leads to more efficient charge injection and extraction at the pentacene/PANI-PAAMPSA interface compared to a pentacene/gold interface.

Despite the fact that PANI-PAAMPSA has enhanced charge injection and extraction at the channel/electrode interface in pentacene TFTs, the bulk resististivity of this material remains high (≅5Ωcm). We have successfully reduced the bulk resistivity of PANI-PAAMPSA by more than two orders of magnitude through a simple dichloroacetic acid (DCA) treatment. Our characterization reveals that DCA induces drastic structural changes of PANI-PAAMPSA. DCA moderates the ionic interactions between PANI and PAAMPSA. PANI-PAAMPSA chains can thus rearrange from the “compact-coil” to the “extended chain” conformation. Efficient charge transport is thus enabled through such "extended chain" PANI-PAAMPSA conformation. The use of DCA-treated PANI-PAAMPSA as functional electrodes increases device performance (i.e., mobilities and on/off currnet ratios) of TFTs utilizing functionalized acenes by more than an order of magnitude. Specifically, bottom-contact triisopropylsilyl pentacene TFTs with DCA-treated PANI-PAAMPSA electrodes exhibit mobilities and on/off current ratios as high as 0.12 cm^2/V-s and 10^5, respectively.

Lastly, we show that the molecular structure of vacuum-deposited organic semiconductor molecules, i.e., pentacene and dihexylthiophene anthracene (DHT-ANT) can be drastically different depending on the nature of the surface chemistry of the substrates. Specifically, pentacene and DHT-ANT grow two-dimensional (2D) grains when the molecule-substrate interactions are weak. In these 2D grains, the fused rings of the molecules are generally oriented upright on the substrate surface. On the other hand, if the molecule-substrate interactions are strong, the molecules tend to grow one-dimensional (1D) grains. The fused rings of the molecules are generally parallel to the substrate surface. The details of the molecular orientation in turn significantly influence the electronic band structures of the organic semiconductors. Specifically, molecules with fused rings lying flat on substrate surfaces exhibit higher work functions compared to molecules with fused rings oriented upright.

We demonstrated several examples showing how the processing-structure-property relationships of PANI-PAAMPSA facilitate its incorporation in organic TFTs. Such relationships are beneficial for organic electronics as the field moves towards real applications on a commercial scale.

Table of Contents

List of Tables

List of Figures

Chapter 1: Introduction

MOTIVATION

Polyaniline (PANI), a conducting polymer, has been the subject of study for the past 100 years.[1] Despite its long history, the conducting properties of PANI have not been extensively investigated until the early 1980s. Since then, research on conductive PANI has accelerated, in large part due to several attractive attributes including inexpensive aniline monomer, straightforward synthesis, the ability to achieve metallic conductivity through a proton doping mechanism and excellent redox stability.[1-3]

PANI can exist in various distinct oxidation states.[1] Figure 1.1 shows the oxidation states of PANI. The fully reduced state is known as leucoemeraldine base (Figure 1.1a), the half oxidized and half reduced form shown in Figure 1.1b is known as emeraldine base, and the fully oxidized form is known as pernigraniline base (Figure 1.1c).[1, 2] While none of these base forms are electrically conductive, conductive PANI can be obtained by converting emeraldine base to emeraldine salt through a process called by "protonic acid doping".[1] The mechanism of protonic acid doping of PANI was elucidated by the late Prof. MacDiarmid and colleagues in the 1980s.[1] The doping process starts with emeraldine base, which contains equal moles of reduced (benzenoid) and oxidized units (quinoid), as shown in Figure 1.2a (or Figure 1.1b).[2, 3] By adding an acid, such as hydrochloric acid, the imine nitrogen atoms in the emeraldine base are protonated (Figure 1.2b). As a result, the emeraldine base is converted into an emeraldine salt (Figure 1.2c). In the salt form, the charges are delocalized along the

PANI backbone thus enabling charge transport through PANI.[2, 3] The PANI emeraldine salt typically exhibits a conductivity ranging from 1 to 10^4S/cm, which is significantly higher than the conductivity of PANI emeraldine base (10^{-10}S/cm) which, for all practical purposes, is considered as insulator.[1]

In the early years following the discovery of conductive PANI, as well as other conducting polymers, such as polyacetylene[4], conductive PANI doped with small-molecule acids (e.g., HCl) was regarded as "intractable",[5] i.e., it is not readily soluble in any common solvents which severely limits processability. Such intractability stems from the strong inter-chain interactions of conducting polymers. In conducting polymers, the inter-chain interactions are dominated by electron transfer, which is stronger than van der Waals or hydrogen bonding that typically exist in saturated polymers.[3] Yet, solution-processable PANI was successfully demonstrated in the early 1990s.[5] In this specific case, PANI was doped with bifunctional counter ions. These ions have an acid group at one end that can protonate PANI and a long alkyl chain at the other end that can impart solubility of the doped product in non-polar or weakly polar organic solvents.[5] The final conductive PANI is thus solution-processable.[5] More recently, aqueous dispersions of conductive PANI have been demonstrated through the synthesis of aniline in the presence of a polymer acid template.[6] In this process, PANI is protonated by the acid pendant groups in the polymer acid template and excess acid groups in the polymer acid render the final PANI-polymer acid complex water-dispersible.[6]

The development of solution-processable, conductive PANI has lead researchers to investigate PANI as a promising candidate for a wide spectrum of applications including polymer coatings,[7] chemical sensing,[8] microelectronics,[9, 10] and organic electronics.[11, 12] For example, conductive PANI that can be processed from organic solvents has been incorporated as functional electrodes and wires in organic electronic devices on flexible substrate platforms.[11, 12] Despite these demonstrations, suitable process techniques for solution-processable, conductive PANI are still limited. More seriously, the elucidation of processing-structure-property relationships of such PANI formulations is lacking. Such relationships are critical in order for organic and polymer electronic materials to be successfully incorporated in electronic devices, as this field moves towards commercialization.[13]

This thesis focuses on establishment of an understanding the processing-structure-property relationships of our particular water-dispersible, conductive PANI. We show that such understanding facilitates the incorporation of PANI into organic thin-film transistors (TFTs). The water-dispersible, conductive PANI used in our research is PANI-PAAMPSA, which is PANI that is template synthesized in the presence of poly(2-acryl-amido-2-methyl-1-propanesulfonic acid), PAAMPSA.[14, 15] PANI-PAAMPSA is of particularly interest because it exhibits the highest conductivity of the water-dispersible, conductive PANI's, such as PANI synthesized with poly(styrene sulfonic) acids, PSS.[14] PANI-PAAMPSA also exhibits enhanced wetting and adsorption behavior on hydrophilic surfaces compared to other water-dispersible, conductive PANI analogs.[14] We successfully exploited the selective wetting property of PANI-PAAMPSA in developing direct patterning techniques to incorporate PANI-PAAMPSA in organic TFT devices.[15]

BACKGROUND

During the last decade, there has been tremendous progress in the field of organic TFTs.[16-19] Such progress has been driven by the promise of organic TFTs in low-cost, large-area, and flexible electronic applications, such as backplane active-matrix circuits for driving flexible displays,[20, 21] inexpensive radio-frequency identification tags,[22, 23] and disposable sensors.[8, 24] As such, organic TFTs aim to fill niches that are not easily accomplished by current silicon-based TFT devices.[18]

Figure 1.3 shows schematics of two typical organic thin-film transistor device geometries, the top- (Figure 1.3a) and bottom-contact architecture (Figure 1.3b).[25] Both device geometries consist of multiple layers of conductors (source, drain, and gate electrodes), an insulator (gate dielectric layer), and an organic semiconductor (active layer). In most research that investigates the electrical properties of organic semiconductors, noble metals, such as gold and platinum are used as the source and drain electrodes. A silicon platform in which highly doped silicon serves as gate and silicon dioxide gate dielectric is commonly used in conjunction. In this thesis, emphasis is placed on replacing the metal source and drain electrodes with PANI-PAAMPSA. For ease of comparison, the same Si/SiO_2 platform was used.

The primary function of the organic TFT is a switching operation in which "on" and "off" states are controlled by a bias applied at the gate electrode.[26, 27] For example, in an active-matrix display, each of the organic TFTs in the backplane circuit controls the "on" and "off" states of individual pixels in the emissive layer.[27] Applying a voltage between the gate and the source electrodes accumulates charges within the first 5nm of the organic semiconductor layer near the organic semiconductor/gate dielectric interface.[26, 28] These charges in turn enable current to flow between the source and the drain electrodes, thereby turning on the TFT. For organic TFTs to be successfully used in the previously mentioned applications, such as backplane circuits for driving displays, the organic semiconductor layer when incorporated in devices needs to exhibit a mobility of $>0.1 cm^2/V\text{-}s$, on/off current ratio of $> 10^4$, and threshold voltage close to 0V.[19, 25, 29] The definitions and extractions of these parameters are provided in Chapter 2.

While the performance of some organic TFTs, such as pentacene thin-film transistors (TFTs) has been demonstrated to meet, or even exceed, the requirements listed above, these devices are frequently fabricated using conventional high-vacuum deposition and photolithographic patterning techniques, which can be costly from both capital and operational standpoints.[17, 19] The success of organic TFTs in low-cost, large-area, flexible electronic applications will have to rely on the development of organic and polymer electronic materials that can be easily processed with straightforward solution-deposition techniques while yielding high electrical peformance.[18, 19] This goal can be achieved by the development of inexpensive patterning and fabrication processes through maximizing the unique properties of solution-processable organic and polymer electronic materials, such as self assembly, surface wetting and adsorption properties.

In Chapter 3, we discuss the direct patterning techniques we have developed for making PANI-PAAMPSA features. As mentioned earlier, solution-processable conductive PANI was first demonstrated in the early 1990s.[5, 6] The development of prior patterning techniques have to focused on PANI doped with hydrochloric acid.[30-33] Despite the lack of processability stemming from their limited solubility, several techniques have been developed to pattern PANI-HCl and/or PANI-H_2SO_4.[30-33] These techniques typically exploit the area-selective electropolymerization of aniline onto specific regions of a previously-patterned molecular template on a bare gold surface. These molecular templates can be created by selectively depositing n-alkylthiols or functionalized thiols with $-CF_3$, $-OH$, $-NH_2$, and $-COOH$ end groups, on gold via microcontact printing.[30, 31] During electropolymerization of aniline in aqueous acidic media, these thiol layers serve as blocking layers to inhibit electron transfer between aniline and the gold surface. While n-alkylthiols are poor blocking layers, functionalized thiols effectively provide a barrier that inhibits the electropolymerization of anilines.[30, 31] PANI-H_2SO_4 features as small as 6μm can be "grown" on regions of bare gold using this technique.[30, 31] PANI-H_2SO_4 lines grown in this fashion exhibit a conductivity of 0.01S/cm.[30, 31] Alternatively, a molecular template can be created by selectively photo-patterning a pre-coated molecular layer, e.g., bis[11-[(4-azidobenzoyl)oxy]-1-undecyl] disulfide on a gold surface.[32] When this molecular layer is irradiated through a photomask in the presence of various amines, the molecules in the irradiated regions become amine terminated.[32] Similar to the functionalized thiols, these amine-terminated molecules effectively serve as barrier for the electropolymerization of aniline. Electropolymerization of aniline in an aqueous H_2SO_4 medium thus only takes place in the non-irradiated regions resulting in PANI-H_2SO_4 features in the dimension and geometry of the molecular template.[32] A major drawback, however, exists in these techniques. In order for electropolymerization to occur, a high conductive substrate (e.g., gold) is needed. The final PANI features must thus be removed and transferred onto an insulating substrate to eliminate lateral shorts between individual PANI features through the underlying gold substrate.

Electroless polymerization of aniline was demonstrated using a molecular template created on insulating substrates, such as glass and silicon with native oxide.[33] In this technique, the molecular template is created by selectively depositing alkyltrichlorosilane on a hydrophilic surface (–SiO_x) using microcontact printing.[33] The regions that were exposed to alkyltrichlorosilane treatment become hydrophobic. During the polymerization of aniline in an aqueous HCl medium, PANI-HCl grows preferentially in the hydrophobic (alkyltrichlorosilane-treated) regions likely due to surface energy difference. As a result, a much thicker PANI film is created in the hydrophobic regions compared to that in the hydrophilic regions. PANI features with lateral size as small as 2μm in the hydrophobic regions can then be transferred onto an adhesion tape[33]. Although this technique does not require conductive gold substrates, like the others, it still requires the polymerization of aniline during patterning. As such, there is little control over the synthesis conditions, which necessarily changes the conductivity of PANI.

In the late 1990s, a Phillips research group[11] demonstrated a technique to pattern PANI that is doped with camphor sulfonic acid (CSA); bifunctional dopant.[5, 34] Because PANI-CSA can be dispersed and directly patterned from m-cresol, conductive features can be generated without any need for *in-situ* polymerization. A photo-patterning technique has been employed to pattern a spun-cast PANI-CSA film from its m-cresol solution.[11] Specifically, a photoinitiator, 1-hydroxycyclohexylphenylketone, is added to the PANI-CSA solution in m-cresol before spin-casting. The film is exposed to deep ultraviolet irradiation through a photomask under nitrogen atmosphere. In the regions of irradiation, conductive PANI (the emeraldine salt form) is reduced to the non-conductive form (leucoemeraldine base).[11] The non-conductive PANI regions can thus electrically isolate conductive PANI in the non-irradiated regions. The photoinitiator in the non-irradiated regions is then removed by heating the film at 110°C. The conductivities of non-irradiated regions and irradiated regions in the final film are 50 and 5×10^{-10} S/cm, respectively.[11] This technique yields conductive PANI features as small as 1-2 μm on a flexible polyimide foil glued onto 3 inch wafer.[11] However, this technique can be potentially complicated by the requirement of additional chemistry to enables photo-patterning.

Recently, a DuPont research group[12] demonstrated the direct patterning of conductive PANI that is doped with dinonylnaphthalene sulfonic acid (DNNSA) using laser thermal transfer imaging. In this technique, conductive PANI is coated on a flexible donor substrate. The donor substrate, along with a flexible receiver substrate, is loaded into a commercial-scale laser printer. Focusing the laser light onto the donor substrate locally transfers PANI in the exposed regions onto the receiver substrate.[12] While this process allows the transfer of individual PANI features onto a flexible substrate, the heat produced during the transfer process inevitably damages the PANI. For example, PANI-CSA cannot withstand the heat generated by the laser exposure as it is dedoped during this process.[12] PANI-DNNSA can be laser printed without dedoping. While PANI-DNNSA is solution-processable, it exhibits an inherently low conductivity of 10^{-4}S/cm.[12] To circumvent the reduction in electrical conductivity, PANI-DNNSA is mixed with single-wall carbon nanotubes (SWNT) and the mixture is printed on plastic. The resulting conductivity of the printed mixture is 3S/cm.[12] Although this technique enables the direct patterning of conductive PANI/SWNT features on a flexible substrate, the utility of this technique is limited by the scarcity of materials having sufficient thermal stability with a high electrical conductivity and the need of an expensive commercial laser printer. In contrast, the patterning techniques we developed for PANI-PAAMPSA described in Chapter 3 are simple, inexpensive, and exploit the selective wetting and adsorption characteristics of PANI-PAAMPSA.[15] Features as small as 5μm with average conductivities of 0.2S/cm can be routinely made.

Once suitable patterning techniques for PANI-PAAMPSA were developed, it was important to assess how PANI-PAAMPSA components function and whether they are compatible with other components in functional organic TFTs. The performance of organic TFTs with PANI-PAAMPSA electrodes also need be within the requirements for typical organic TFT applications. The following paragraphs describe some important factors that govern the performance of typical organic TFTs.

Generally, the performance of organic TFTs is greatly influenced by the molecular structure and the morphology of the organic semiconductor film. A highly ordered crystalline film generally yields high mobility.[25, 26] Highly-ordered crystalline organic semiconductor films can be frequently obtained by thermally evaporating small-molecule organic semiconductor, such as pentacene, in a high-vacuum chamber (10^{-6} to 10^{-8} Torr). In general, films with larger grains also tend to exhibit higher mobilities.[26] The size of organic semiconductor grains is significantly influenced by the surface roughness of the gate dielectric.[25] A high surface roughness increases the nucleation density. As a result, the grain size is decreased while the number of grain boundaries is increased in organic semiconductor films that are deposited on rough gate dielectrics. The gate dielectric surface can be modified to improve the growth of larger and well-connected organic semiconductor grains. The modification of gate dielectric surface can also reduce interfacial trap densities.[26] For example, SiO_2 dielectric surface is often treated with either hexamethyl disilazane (HMDS)[35] or octadecyl trichlorosilane (OTS)[36]. These molecules not only promote grain growth, they also reduce charge trapping by Si-OH.[26] In this vein, we have thus used these molecules to create molecular templates for our patterning.

The performance of organic semiconductors in TFT devices can also be influenced by the device geometry. The performance of top-contact device (Figure 1.3a) is typically superior to that of bottom-contact devices (Figure 1.3b).[26] Such disparity is attributed to a difference in the growth habit of the organic semiconductors on the substrate surfaces. In top-contact devices, a uniform organic semiconductor film is first deposited on the gate dielectric surface. The source and drain electrodes are subsequently defined on top of the uniform organic semiconductor layer. As a result, the grains are continuous at the organic semiconductor/electrode interfaces (see Figure 1.3a).[37-39] In bottom-contact devices, the source and drain electrodes are pre-patterned prior to the deposition of the organic semiconductor layer. The organic semiconductor is thus deposited on two different surfaces, i.e., the gate dielectric surface and the gold electrode surface. It has been shown that most organic semiconductors tend to form smaller grains on gold electrodes compared to that on the gate dielectric (i.e., SiO_2).[26, 40] Such different growth behavior is frequently manifested as a discontinuity in the grain morphology at the interface between dielectric and electrode surfaces. Given that this interface governs charge injection and charge extraction in organic TFTs, a discontinuity in the morphology of the organic semiconductor across this interface necessarily introduces defects that can trap charges, which in turn causes degradation of device performance.[25, 40] The growth of organic semiconductors on gold electrode needs to be optimized to improve the performance of bottom-contact devices. Large pentacene grains on gold electrode can be achieved by treating gold electrode surface with hexadecanethiol; this leads to improved mobility of bottom-contact pentacene devices.[40]

Recent reports suggest that the use of conducting polymer electrodes can also improve device performance in bottom-contact pentacene TFTs.[12, 41, 42] For example, the DuPont research group[12] showed that PANI-DNNSA/SWNT composite electrodes make efficient contacts to the pentacene active layer in the bottom-contact TFTs. Their bottom-contact devices exhibit a saturation mobility of 0.3cm^2/V-s, which is two times higher than that of the control devices with gold electrodes having the channel dimensions and the device geometry.[12] Similarly, we find that PANI-PAAMPSA electrodes make efficient electrical contact to pentacene in the bottom-contact TFTs. Charge injection and extraction at the pentacene/PANI-PAAMPSA interface is improved compared to those at pentacene/gold interface in control TFTs having the same device dimensions and geometry. Chapter 4 provides detailed structural characterization of the pentacene/PANI-PAAMPSA interface as a step towards to the elucidation of its enhanced performance. Specifically, we find that the morphology and molecular orientation of pentacene thin film are favorable for charge injection and extraction at PANI-PAAMPSA/pentacene interface compared to the gold/pentacene interface.

While PANI-PAAMPSA provides ease of processing and patterning compared to other conductive PANI, its average electrical conductivity is only 0.2S/cm.[15] Such low bulk conductivity of PANI-PAAMPSA can significantly hamper its functionality as interconnects and wires that connect individual TFTs in circuits. As a result, there is a need to improve the conductivity of PANI-PAAMPSA. It has been shown that the conductivity of PANI can vary drastically depending on the solvent from which PANI is processed.[43-45] For example, PANI-CSA cast from chloroform exhibits a conductivity of 0.2S/cm.[45] The same PANI-CSA cast from m-cresol, on the other hand, exhibits conductivities as high as 300S/cm.[45] Similar conductivity improvements can also be achieved by exposing/immersing PANI-CSA films cast from chloroform to m-cresol. This conductivity improvement is termed "secondary doing" and is attributed to changes in PANI chain conformation induced by the solvent.[34, 43, 44] This solvent should have strong interactions with both PANI and the dopant. Such interactions increase the distance between PANI and its dopant. As a result, PANI chain conformation changes drastically. Specifically, the "compact coil" conformation[43, 44] of PANI chains is converted to an "extended chain" conformation,[43, 44] as illustrated in Figure 1.4. The "extended chain" conformation greatly reduces any structural defects that can hamper charge transport, thereby increasing the conductivity.[43, 44] Such conductivity improvements for PANI doped with polymer acids (templated synthesized) have not been reported and this indicates the complexity of secondary doping in PANI doped with polymer acids. Recently, we have improved the conductivity of PANI-PAAMPSA by more than two orders of magnitude using a dichloroacetic acid (DCA) treatment. A mechanism for the conductivity improvement is proposed based on the electrical and structural characterization of DCA-treated PANI-PAAMPSA in Chapter 5. We will also show that the use of DCA-treated PANI-PAAMPSA source and drain electrodes increases current output from bottom-contact pentacene TFTs and improves the performance of TFTs utilizing functionalized acene organic semiconductors.

Elucidating and manipulating the molecular structure of PANI-PAAMPSA is important to maximize its conductivity. In the same vein, understanding the molecular structure of organic semiconductors is critical to improve device performance when the organic semiconductors are incorporated in functional devices. For example, the morphology[46-50] and molecular orientation[50-52] of organic semiconductor films have been shown to significantly affect device performance, e.g., mobility, when these films are used as the active layer in organic TFTs. Additionally, it is also important to elucidate how the molecular structures can be related to the electronic structures, e.g., ionization energy and work function, of organic semiconductors for further improving device performance. Significant efforts have been made to understand the relationship between the molecular structures and the electronic structures of organic semiconductors. These studies, however, have focus on either on characterizing the molecular structures[53-55], or on elucidating interfacial electronic band structures.[56-58] How the molecular structures are correlated with the electronic structures of organic semiconductors is still not well understood.

In Chapter 6, we report a direct correlation between the morphology, molecular orientation, and work function of two small-molecule organic semiconductors, i.e., pentacene and DHT-ANT. Our results suggest that controlling electronic structures is possible through manipulating the molecular structure the organic semiconductors.

THESIS OVERVIEW

Chapter 2 describes the templated synthesis of PANI-PAAMPSA. This chapter also provides brief descriptions of experimental techniques used in our research.

Chapter 3 details the direct patterning techniques for PANI-PAAMPSA. These techniques exploit the selective wetting and adsorption properties of PANI-PAAMPSA. As a consequence, our patterning techniques of PANI-PAAMPSA do not require any in-situ polymerization and therefore eliminate the high capital and operational costs associated with patterning. We also demonstrate the utility of our patterning techniques in fabricating pentacene TFTs.

Chapter 4 details the structural characterization of pentacene thin films at the pentacene/PANI-PAAMPSA interface in TFTs to assess the compatibility of PANI-PAAMPSA with the pentacene active layer. For comparison, we characterized the pentacene/gold interface in control TFTs that have the same channel dimensions and device geometry. In each device, the components that limit device performance are identified by collecting surface potential profiles during device operation. We provide an example showing how contact resistance can be suppressed in pentacene TFTs with PANI-PAAMPSA electrodes to improve the device performance.

Chapter 5 reports the electrical conductivity improvement in PANI-PAAMPSA derived from dichloroacetic (DCA) treatment. The development of such post-processing techniques is essential to maximize the conductivity of PANI-PAAMPSA for expanding their functionality in interconnects and wires for TFT applications. The mechanism of conductivity improvement by DCA treatment is proposed based detailed structural characterization. We also demonstrate the performance (mobility and on/off current ratios) of TFTs utilizing functionalized acenes can be improved by more than an order of magnitude using DCA-treated PANI-PAAMPSA source and drain electrodes.

Chapter 6 summarizes our examinations of two vapor-deposited organic semiconductors, i.e., pentacene and dihexylthiophene anthracene (DHT-ANT). The morphology and molecular orientation of the organic semiconductor films vary drastically depending on the subtle details of substrate preparation. These molecular structures are shown to greatly influence the work functions of the organic semiconductors. As a consequence, we establish a direct correlation between the morphology, molecular orientation, and work functions of the organic semiconductors.

Finally, Chapter 7 summarizes the major achievements of our research and provides suggestions for future work.

FIGURES

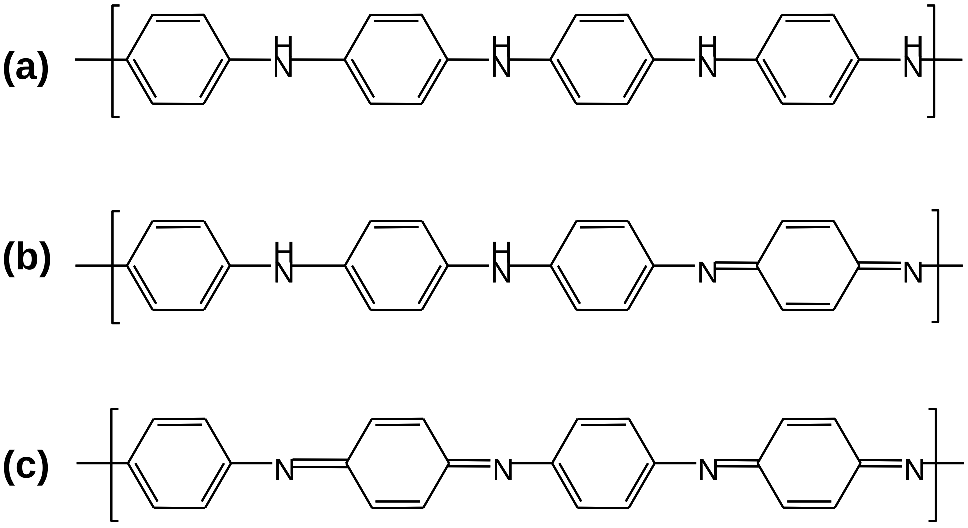

Figure 1.1. The three distinct oxidation states of PANI: (a) the fully reduced form, which is known as leucoemeraldine base, (b) the half oxidized and reduced form, which is known as emeraldine base, and (c) the fully oxidized form, also known as pernigraniline base.

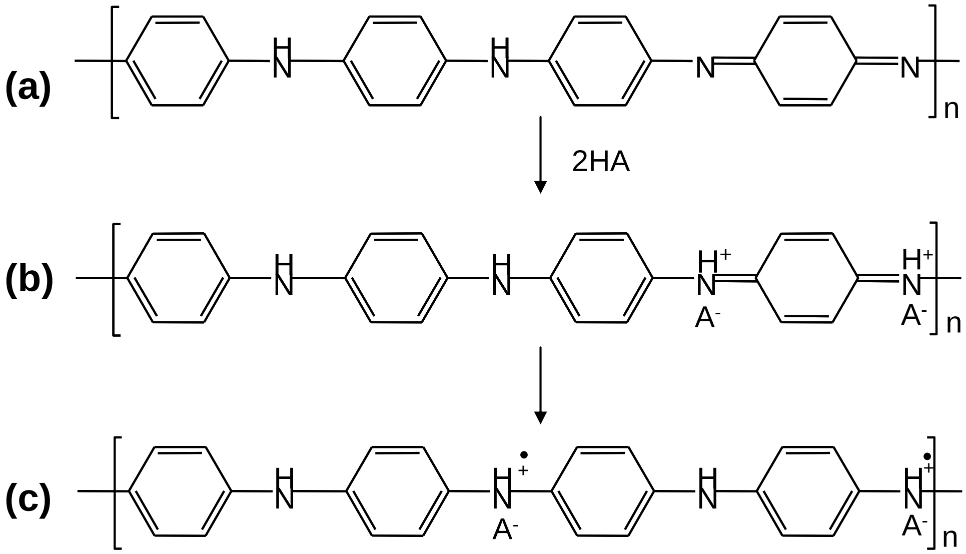

Figure 1.2. “Protonic acid doping” of PANI emeraldine base (a). PANI emeraldine base is protonated when exposed to an acid (HA) (b). Charge delocalization (c) allows for charge transport along the PANI backbone.

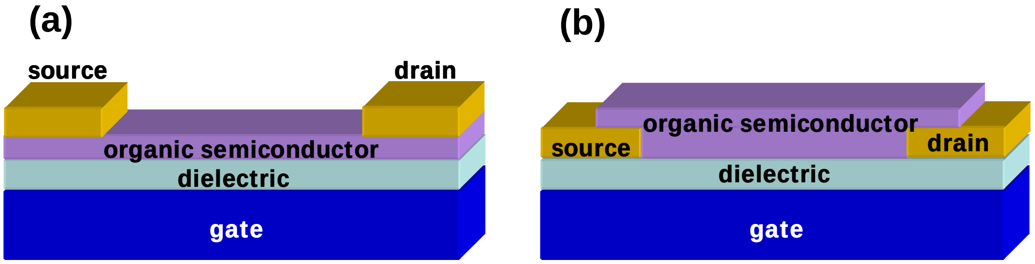

Figure 1.3. Typical organic thin-film transistor geometries: (a) top-contact (b) bottom-contact.

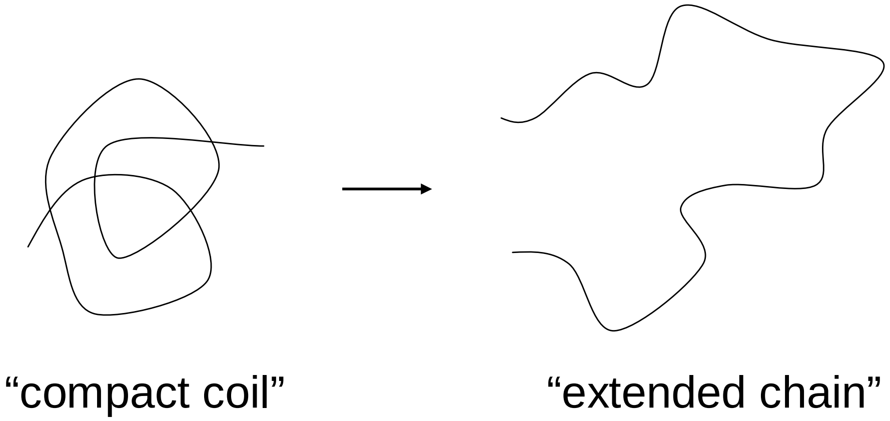

Figure 1.4. Illustrations of two distinct PANI conformations: (a) "compact coil" and (b) "extended chain" .[43, 44]

REFERENCES

1. J. C. Chiang, A. G. Macdiarmid, *Synthetic Metals* **1986**, *13*, 193.
2. A. G. MacDiarmid, *Angewandte Chemie-International Edition* **2001**, *40*, 2581.
3. A. J. Heeger, *Angewandte Chemie-International Edition* **2001**, *40*, 2591.
4. H. Shirakawa, *Angewandte Chemie-International Edition* **2001**, *40*, 2575.
5. Y. Cao, P. Smith, A. J. Heeger, *Synthetic Metals* **1992**, *48*, 91.
6. L. Sun, S. C. Yang, *Polymer Preprints* **1992**, *33*, 379.
7. P. Zarras, N. Anderson, C. Webber, D. J. Irvin, J. A. Irvin, A. Guenthner, J. D. Stenger-Smith, *Radiation Physics and Chemistry* **2003**, *68*, 387.
8. J. Janata, M. Josowicz, *Nature Materials* **2003**, *2*, 19.
9. M. Angelopoulos, N. Patel, *Polymeric Materials Science and Engineering* **1994**, *71*, 222.
10. M. Angelopoulos, *IBM Journal of Research and Development* **2001**, *45*, 57.
11. C. J. Drury, C. M. J. Mutsaers, C. M. Hart, M. Matters, D. M. de Leeuw, *Applied Physics Letters* **1998**, *73*, 108.
12. G. B. Blanchet, Y.-L. Loo, J. A. Rogers, F. Gao, C. R. Fincher, *Applied Physics Letters* **2003**, *82*, 463.
13. www.plasticlogic.com.
14. J. E. Yoo, J. L. Cross, T. L. Bucholz, K. S. Lee, M. P. Espe, Y.-L. Loo, *Journal of Materials Chemistry* **2007**, *17*, 1268.
15. K. S. Lee, G. B. Blanchet, F. Gao, Y.-L. Loo, *Applied Physics Letters* **2005**, *86*, 074102.
16. Z. N. Bao, *Advanced Materials* **2000**, *12*, 227.
17. J. R. Sheats, *Journal of Materials Research* **2004**, *19*, 1974.
18. S. R. Forrest, *Nature* **2004**, *428*, 911.

19. J. E. Anthony, *Chemical Reviews* **2006**, *106*, 5028.

20. J. A. Rogers, Z. Bao, K. Baldwin, A. Dodabalapur, B. Crone, V. R. Raju, V. Kuck, H. Katz, K. Amundson, J. Ewing, P. Drzaic, *Proceedings of the National Academy of Sciences of the United States of America* **2001**, *98*, 4835.

21. G. H. Gelinck, H. E. A. Huitema, E. van Veenendaal, E. Cantatore, L. Schrijnemakers, J. B. P. H. van der Putten, T. C. T. Geuns, M. Beenhakkers, J. B. Giesbers, B.-H. Huisman, E. J. Meijer, E. M. Benito, F. J. Touwslager, A. W. Marsman, B. J. E. van Rens, D. M. de Leeuw, *Nature Materials* **2004**, *3*, 106.

22. P. F. Baude, D. A. Ender, M. A. Haase, T. W. Kelley, D. V. Muyres, S. D. Theiss, *Applied Physics Letters* **2003**, *82*, 3964.

23. R. Rotzoll, S. Mohapatra, V. Olariu, R. Wenz, M. Grigas, K. Dimmler, O. Shchekin, A. Dodabalapur, *Applied Physics Letters* **2006**, *88*.

24. B. K. Crone, A. Dodabalapur, R. Sarpeshkar, A. Gelperin, H. E. Katz, Z. Bao, *Journal of Applied Physics* **2002**, *91*, 10140.

25. C. D. Dimitrakopoulos, P. R. L. Malenfant, *Advanced Materials* **2002**, *14*, 99.

26. M. M. Ling, Z. Bao, *Chemistry of Materials* **2004**, *16*, 4824.

27. Y. L. Loo, *Aiche Journal* **2007**, *53*, 1066.

28. M. A. Alam, A. Dodabalapur, M. R. Pinto, *Ieee Transactions on Electron Devices* **1997**, *44*, 1332.

29. G. W. Neudeck, A. K. Malhotra, *Solid-State Electronics* **1976**, *19*, 721.

30. D. M. Collard, C. N. Sayre, *Synthetic Metals* **1997**, *84*, 329.

31. C. N. Sayre, D. M. Collard, *Journal of Materials Chemistry* **1997**, *7*, 909.

32. L. F. Rozsnyai, M. S. Wrighton, *Chemistry of Materials* **1996**, *8*, 309.

33. Z. Huang, P.-C. Wang, A. G. MacDiarmid, Y. Xia, G. Whitesides, *Langmuir* **1997**, *13*, 6480.

34. Y. Cao, J. Qiu, P. Smith, *Synthetic Metals* **1995**, *69*, 187.

35. H. Yang, T. J. Shin, M.-M. Ling, K. Cho, C. Y. Ryu, Z. Bao, *Journal of the American Chemical Society* **2005**, *127*, 11542.

36. A. Salleo, M. L. Chabinyc, M. S. Yang, R. A. Street, *Applied Physics Letters* **2002**, *81*, 4383.

37. P. V. Necliudov, M. S. Shur, D. J. Gundlach, T. N. Jackson, *Solid-State Electronics* **2002**, *47*, 259.

38. Y. Roichman, N. Tessler, *Applied Physics Letters* **2002**, *80*, 151.

39. K. P. Puntambekar, P. V. Pesavento, C. D. Frisbie, *Applied Physics Letters* **2003**, *83*, 5539.

40. I. Kymissis, C. D. Dimitrakopoulos, S. Purushothaman, *IEEE Transactions on Electron Devices* **2001**, *48*, 1060.

41. H. Sirringhaus, T. Kawase, R. H. Friend, T. Shimoda, M. Inbasekaran, W. Wu, E. P. Woo, *Science* **2000**, *290*, 2123.

42. M. Lefenfeld, G. Blanchet, J. A. Rogers, *Advanced Materials* **2003**, *15*, 1188.

43. A. G. MacDiarmid, A. J. Epstein, *Synthetic Metals* **1994**, *65*, 103.

44. A. G. MacDiarmid, A. J. Epstein, *Synthetic Metals* **1995**, *69*, 85.

45. Y. N. Xia, J. M. Wiesinger, A. G. Macdiarmid, A. J. Epstein, *Chemistry of Materials* **1995**, *7*, 443.

46. D. J. Gundlach, Y. Y. Lin, T. N. Jackson, S. F. Nelson, D. G. Schlom, *IEEE Electron Device Letters* **1997**, *18*, 87.

47. R. Ye, M. Baba, Y. Ohishi, K. Mori, K. Suzuki, *Molecular Crystals and Liquid Crystals* **2003**, *407*, 543.

48. X. L. Chen, A. J. Lovinger, Z. Bao, J. Sapjeta, *Chemistry of Materials* **2001**, *13*, 1341.

49. J. Chen, D. C. Martin, J. E. Anthony, *Journal of Materials Research* **2007**, *22*, 1701.

50. K. S. Lee, T. J. Smith, K. C. Dickey, J. E. Yoo, K. J. Stevenson, Y.-L. Loo, *Advanced Functional Materials* **2006**, *16*, 2409.

51. H. Sirringhaus, P. J. Brown, R. H. Friend, M. M. Nielsen, K. Bechgaard, B. M. W. Langeveld-Voss, A. J. H. Spiering, R. A. J. Janssen, E. W. Meijer, P. Herwig, D. M. De Leeuw, *Nature (London)* **1999**, *401*, 685.

52. D. M. DeLongchamp, S. Sambasivan, D. A. Fischer, E. K. Lin, P. Chang, A. R. Murphy, J. M. J. Frechet, V. Subramanian, *Advanced Materials* **2005**, *17*, 2340.

53. W. S. Hu, Y. T. Tao, Y. J. Hsu, D. H. Wei, Y. S. Wu, *Langmuir* **2005**, *21*, 2260.

54. D. Kafer, L. Ruppel, G. Witte, *Physical Review B: Condensed Matter and Materials Physics* **2007**, *75*, 085309/1.

55. S. Lukas, S. Soehnchen, G. Witte, C. Woell, *ChemPhysChem* **2004**, *5*, 266.

56. H. Ishii, K. Sugiyama, E. Ito, K. Seki, *Advanced Materials (Weinheim, Germany)* **1999**, *11*, 605.

57. I. G. Hill, A. Rajagopal, A. Kahn, Y. Hu, *Applied Physics Letters* **1998**, *73*, 662.

58. N. Koch, A. Elschner, J. Schwartz, A. Kahn, *Applied Physics Letters* **2003**, *82*, 2281.

Chapter 2: Experimental Techniques

SYNTHESIS OF WATER-DISPERSIBLE POLYANILINE

The water-dispersible polyaniline (PANI) used in the initial stages of this work was provided by Dr. Feng Gao at DuPont Central Research and Development in Wilmington, DE. The synthesis expertise has since been brought in house; later materials were synthesized and characterized by Joung Eun Yoo in our group before they were used for this project.

The synthesis of conductive PANI begins with addition of aniline monomer (Fisher Scientific, 99.9%) to an aqueous solution of poly(2-acrylamido-2-methyl-1-propane-sulfonic acid), PAAMPSA (Scientific Polymer Products Inc., 10wt% in water, $M_{w,PEO}$=724kg/mol).[1] PAAMPSA is a water-soluble polymer acid and serves two roles: it provides a template on which aniline is polymerized, and its sulfonic acid groups dopes PANI upon synthesis thereby rendering PANI conductive. The molar feed ratio of aniline to sulfonic acid in PAAMPSA is 1:1.[1] Aniline monomers are then oxidatively polymerized by addition of ammonium persulfate to this aqueous medium that is kept at ≅0°C for the initial six hours of the reaction and is slowly warmed up to room temperature.[1] The reactant medium is vigorously stirred during the course of polymerization.[1] The molar ratio of ammonium persulfate to aniline is 1:0.9.[1] The resulting material is a polymer complex of PANI and PAAMPSA that is ionically associated.[1] PANI-PAAMPSA was then precipitated to remove unreacted monomer by slowly adding acetone and then redispersed in water for patterning.[1]

ORGANIC THIN-FILM TRANSISTOR FABRICATION AND CHARACTERIZATION

An organic thin-film transistor (TFT) is a three terminal device that consists of a gate, a source, and a drain. These devices typically adopt one of two typical geometries, i.e., top- or bottom-contact device geometry depending on how source and drain electrodes make electrical contact to the organic semiconductor layer, as shown in Figure 1.3. In the top-contact device geometry, the organic semiconductor layer is first deposited on the gate dielectric. The source and drain electrodes are subsequently defined on top of the organic semiconductor layer (Figure 1.3a). In contrast, the source and drain electrodes are pre-defined on the gate dielectric layer followed by the deposition of the organic semiconductor layer (Figure 1.3b) in bottom-contact TFTs. In our research, the bottom-contact device geometry is used. Specifically, PANI-PAAMPSA electrodes are pre-defined on Si/SiO_2 substrates using the patterning scheme described in Chapter 3. We used highly-doped silicon (n-doped, $0.004\Omega cm^{-1}$) as the gate electrode. A 100 or 300nm thick layer of thermally-grown silicon dioxide serves as the gate dielectric. For comparison, we also built reference TFTs with gold electrodes in the same bottom-contact geometry. In these reference devices, gold electrodes can be defined either by directly evaporating gold through a shadow mask onto the same Si/SiO_2 substrates, or by photolithography and lift-off. To complete bottom-contact organic TFTs, either 20-50nm of pentacene or 40nm dihexylthiophene anthracene (DHT-ANT)[2] is thermally evaporated through a shadow mask onto the channel regions (at 0.05-0.1nm/s). To ensure consistency, the organic semiconductor is evaporated on both batches of electrodes during the same evaporation run. The substrate temperature is held at 60 and 100°C during pentacene and DHT-ANT evaporation, respectively. The chemical structures of pentacene and DHT-ANT are shown in Figure 2.1a and b, respectively. These organic semiconductors typically exhibit p-channel characteristics as they have the tendency to transport holes.

To evaluate the device characteristics of these TFTs, we performed current-voltage (I-V) measurements using a probe station equipped with an Agilent 4156C Precision Semiconductor Parameter Analyzer. To turn on the organic TFTs, the source-drain electrodes are biased. Simultaneously, the gate electrode is biased to the source electrodes. The output currents from organic TFTs can be modulated by the gate bias. Biasing the gate electrode accumulates charge carriers at the organic semiconductor/dielectric interface thereby enabling current to flow between the source and drain electrodes. Several parameters are used to characterize these devices: the mobility (μ) measures how efficient charge carriers travel through the active organic semiconductor layer. We estimate the mobility of these devices using the equations below. Equations 2.1 and 2.2 describe the linear and saturations regimes of TFTs, respectively:[3]

In the linear regime, $|V_{sd}|<|V_g-V_t|$,

$$I_{sd} = \frac{W}{L}\mu_{lin}C_i(V_g - V_t)V_{sd} \qquad (2.1),$$

In the saturation regime, $|V_{sd}|>|V_g-V_t|$,

$$I_{sd} = \frac{W}{2L}\mu_{sat}C_i(V_g - V_t)^2 \qquad (2.2),$$

where V_{sd}, V_g and V_t are the source-drain, gate and threshold voltages, respectively; I_{sd} is the source-drain current; W and L represent the channel width and length, respectively; and C_i the capacitance of the gate dielectric. Typical mobilities for top- and bottom-contact pentacene TFTs are ≅1 and ≅0.1cm^2/V-s, respectively.[4] Top-contact DHT-ANT TFTs exhibit mobilities as high as 0.5cm^2/V-s.[2] The on/off current ratio (I_{on}/I_{off}) is a measure of contrast between the on an off states of the devices, and is defined as the ratio of the maximum and minimum source-drain currents in the gate voltage operation range. The threshold voltage (V_t) represents the voltage at which the TFT turns on. The threshold voltage can be extracted from the Equations 2.1 and 2.2 for the respective regimes. We can extract the mobility, on/off current ratio, and threshold voltage using the I-V characteristics. Figure 2.2a shows representative I-V characteristics of a pentacene TFT. Since pentacene has p-channel characteristics, negative V_{sd} and V_g are applied. Specifically, V_{sd} is increased from 0 to -20V while V_g is increased from 5 to -20V in increments of -5V. I_{sd} increases linearly when $|V_{sd}| < |V_g-V_t|$ ($V_t \cong 0$V for this device) and is saturated when $|V_{sd}| > |V_g-V_t|$. The I_{sd} and its square root at V_{sd} = -20V are plotted as a function of V_g in blue and black dots, respectively, as shown in Figure 2.2b. These plots are typically referred to as "transfer characteristics".[3] From the transfer characteristics, we obtain the on/off current ratio from I_{max} and I_{min}, as indicated. The mobility is estimated from the slope of the plot of the square root of I_{sd} as a function of V_g and is indicated with a red line in Figure 2.2 (Equation 2.2). The threshold voltage is extracted from the intercept of the slope with the axis of the gate voltage.

SCANNING ELECTRON MICROSCOPY (SEM)

We used a LEO 1530 SEM with low operating voltage capabilities and an in-lens annular detector to characterize the morphology of PANI-PAAMPSA and organic semiconductor thin films. SEM images were acquired at 1-2kV with typical working distances of 4-5mm using the in-lens detector.

ATOMIC FORCE MICROSCOPY (AFM)

The topography and morphology of PANI-PAAMPA and organic semiconductor thin films were characterized using a Digital Instruments Dimension 3100 AFM. The topography and root mean square (r.m.s) roughness of PANI-PAAMPSA and organic semiconductor thin films were acquired in tapping mode. The r.m.s roughness was quantified using NanoScope software ver.6.12r1.

SCANNING SURFACE POTENTIAL MICROSCOPY (SSPM)

A Veeco Instruments Bioscope AFM interfaced with a Nanoscope IV controller and operated in SSPM mode was used to directly measure the local surface potentials of the organic TFTs in operation. All measurements were conducted with phosphorous-doped (n-type, doping level$\cong 10^{17}$cm^{-3}) Si cantilevers (MikroMasch, Ultrasharp tips, length 125 μm, tip radius < 35 nm, resonance frequency ca. 325 kHz, force constant ca. 40 N/m). Electrical contact to the tip was made by applying conductive silver paint (Ted Pella, Inc., No. 16034) to a fresh scratch in the oxide layer.[5] The gate bias was only applied to the TFT during surface potential scans, and not during topography scans, to minimize any electrostatic effects on the scan resolution when obtaining surface topography.[6, 7] Since SSPM measurements can only be obtained on lengths < 100μm, each contact region was scanned sequentially to span the entire channel region greater than 100μm. SSPM experiments were conducted in collaboration with Timothy Smith in Prof. Keith Stevenson's group in the Department of Chemistry and Biochemistry.

ULTRAVIOLET-VISIBLE NEAR-INFRA-RED SPECTROSCOPY (UV-VIS-NIR)

UV-Vis-NIR spectra of PANI-PAAMPSA films on glass slides were collected using a Cary 5000 UV-Vis-NIR spectrometer equipped with a double-beam, rapid-scanning, high-performance spectrometer. A glass slide was used as background. Sample spectra were collected from 200 to 3300nm with a resolution of 1nm.

X-RAY DIFFRACTION (XRD)

X-ray diffraction experiments were conducted with a Scintag X1 θ-θ diffractometer equipped with a Cu Kα X-ray source and a solid-state detector. Samples were analyzed from $2\theta = 5$ to 50° with a resolution of 0.04° and a dwell time of 5 seconds.

NEAR-EDGE X-RAY ABSORPTION FINE STRUCTURE SPECTROSCOPY (NEXAFS)

To quantify the ensemble-average molecular orientation of the organic semiconductor thin films, we performed near edge X-ray absorption fine structure spectroscopy (NEXAFS) experiments at the NIST/Dow soft x-ray materials characterization facility located at beam line U7A at the National Synchrotron Light Source at Brookhaven National Laboratories (Upton, NY).[8] Partial electron yield (PEY) was obtained at the carbon K-edge. Scan steps of 0.1eV and 0.2eV were used to scan the regions of interest (280-310eV) and the pre- and post-edge regions, respectively.[9] The data were collected in vacuum ($\cong 1\times10^{-8}$Torr) at room temperature. The spectra obtained were pre- and post-edge normalized but not background-corrected. By examining the spectral changes as a function of x-ray incident angles, we were able to qualitatively determine the molecular orientation of pentacene and DHT-ANT.[9] NEXAFS experiments were conducted in collaboration with Dr. Kimberly Dickey and Dmitry Krapchetov in our group.

FOURIER TRANSFORM INFRARED SPECTROSCOPY (FTIR)

Fourier transform infrared spectroscopy (FTIR) was carried out using a dry-air-purged Nicolet Magna-IR 860 spectrometer equipped with a liquid-nitrogen-cooled MCT detector. The transmission FTIR spectra of PANI-PAAMPSA films on test Si substrates in Chapter 5 were collected from 400 to 4000cm^{-1} for 300 scans. In Chapter 6, reflection-absorption infrared spectroscopy (RAIRS) and angle-resolved transmission FT-IR with p-polarized light were carried out in collaboration with Dmitry Krapchetov to quantify the molecular orientation of organic semiconductor thin films. Organic semiconductor films on gold substrates were characterized in the reflection absorption mode. A VeeMax II variable-angle grazing accessory with the grazing incidence angle fixed at 80° relative to the substrate normal was used for all RAIRS studies. All the RAIRS spectra were recorded at 2cm^{-1} for 1000 scans. A corresponding bare gold substrate was used as background. Organic semiconductor thin films on Si substrates were characterized in transmission mode at 0° (normal) and 68° (near-grazing) IR incident angles relative to the substrate normal. All transmission spectra were recorded with a 2cm^{-1} resolution for 1000 scans. We used a bare Si substrate as background. Multipoint baseline correction was applied to all spectra using GRAMS/AI commercial software. As for the isotropic references, we acquired a transmission IR spectrum of DHT-ANT powder dispersed in KBr (1:150 mg). The isotropic reference spectrum of pentacene was obtained from literature.[10] All RAIRS and transmission IR spectra are reported in absorbance units, A, where $A = -\log R/R_0$, R is the power reflectivity of the IR beam, and R_0 is the reflectivity of the reference sample.

X-RAY PHOTOELECTRON SPECTROSCOPY (XPS)

XPS was conducted at the Texas Materials Institute Central Facilities using a Physical Electronics ESCA 5700 spectrophotometer equipped with a monochromatic Al Kα X-ray source, a hemispherical electron analyzer. Samples were introduced through a preparation chamber before being transferred into the analysis chamber at 2×10^{-10} Torr. The samples were typically analyzed at a takeoff angle of 45 or 75°, defined as the angle between the sample and the detector. High-resolution scans were collected to quantitatively identify specific binding environments. In the data analysis, the binding energy of the core level C1s peak was set at 284.5eV to compensate for surface charging effects and all elemental spectra were shifted accordingly. Each elemental spectrum was then baseline-subtracted using a Shirley background[11] and deconvoluted using Gaussian functions. The elemental compositions were determined by the ratios of peak areas corrected by the elements' sensitivity factors.

ULTRAVIOLET PHOTOEMISSION SPECTROSCOPY (UPS)

UPS was performed with the help of Dr. Chris Zangmeister at the National Institutes of Standard and Technology in Gaithersburg, MD. Samples were mounted on a vacuum chuck and were placed in a load lock and pumped down until the pressure was

$\approx 1 \times 10^{-8}$Torr (1 to 2 hrs), after which they were moved into the analysis chamber maintained at 1×10^{-9}Torr. UPS spectra were obtained using a He(I) source (21.22eV). The incident angle of the light source is at 45° from the surface normal, and photoelectrons were collected at normal emission with a hemispherical electrostatic analyzer. The reference bare gold substrate was cleaned with ultraviolet light/ozone and rinsed with water before being transferred into the vacuum chamber, and then sputtered in vacuum before its photoemission spectrum was acquired. The measured work function (Φ) of clean gold was 5.38eV.

Three quantities were extracted from the UPS spectra: the work function, the highest occupied molecular orbital (HOMO, Φ_h), and the interfacial dipole (Δ). Figure 2.3a shows representative UPS spectra of gold (black curve) and pentacene on gold (red curve). The work functions of pentacene and gold (Φ) are determined by subtracting the width of the photoemission spectrum from the source photon energy ($h\upsilon$) as follows:

$$\Phi = h\upsilon - (E_{B,\,max} - E_F) \qquad (2.3)$$

where $E_{B,max}$ are E_F are the half-maximum of high biding energy cutoff and the half-maximum of Fermi edge, respectively. The HOMO level of pentacene (Φ_h) is defined as the difference between E_F of gold and the location of the peak maximum in the pentacene spectrum corresponding to the highest occupied orbital of the organic semiconductor molecules, as illustrated in Figure 2.3b. The position of the peak maximum is determined by fitting the appropriate energy interval with a Gaussian for the peak and a polynomial for background. The interfacial dipole (Δ) between gold and pentacene is defined as the difference in the work functions of pentacene and gold, as shown in Figure 2.3c.

ORGANIC SEMICONDUCTOR THIN FILM PREPARATION

The preparation of the organic semiconductor thin films used in Chapter 6 begins with cleaning test Si substrates with native oxide in a piranha solution (2:1 v/v H_2SO_4:H_2O_2) for 10min. The substrates were then rinsed thoroughly with DI water and dried in N_2 stream. Hexamethyldisilazane (HMDS) was then vapor-deposited on the substrates in a prime chamber (YES-3) at 150°C for 2min. PANI-PAAMPSA-coated Si substrates were fabricated by spin-coating PANI-PAAMPSA onto clean Si substrates at 5000rpm for 1min from a 2.5wt% PANI-PAAMPSA aqueous dispersion.

During organic thin-film device fabrication, the gold electrodes were either cleaned with organic solvents or treated with HMDS.[12] To examine how these treatments affect the structure of the organic semiconductor that was subsequently deposited on such substrates, we prepared three different types of gold substrates involving bare gold, HMDS-treated gold, and solvent-cleaned gold. We began by depositing 2nm titanium and 50nm gold onto test Si substrates using e-beam evaporation. These gold substrates were either stored in air until use (bare gold) or surface treated with HMDS or organic solvents. To create HMDS-treated gold substrates, we cleaned the bare gold substrates in a piranha solution for 10min. These gold substrates were then thoroughly rinsed with DI water, and dried in N_2 stream. HMDS was vapor-deposited onto the gold substrates in the prime chamber at 150°C for 2min. Solvent-cleaned gold substrates were prepared by immersing the bare gold substrates in n-methylpyrrolidone (NMP) for 20min at 60°C. These substrates were subsequently sonicated in acetone and in isopropanol for 3min each.

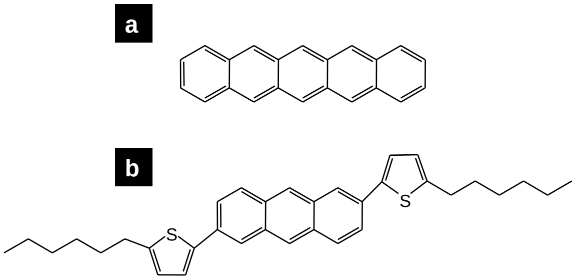

Figure 2.1. Chemical structures of (a) pentacene and (b) DHT-ANT.

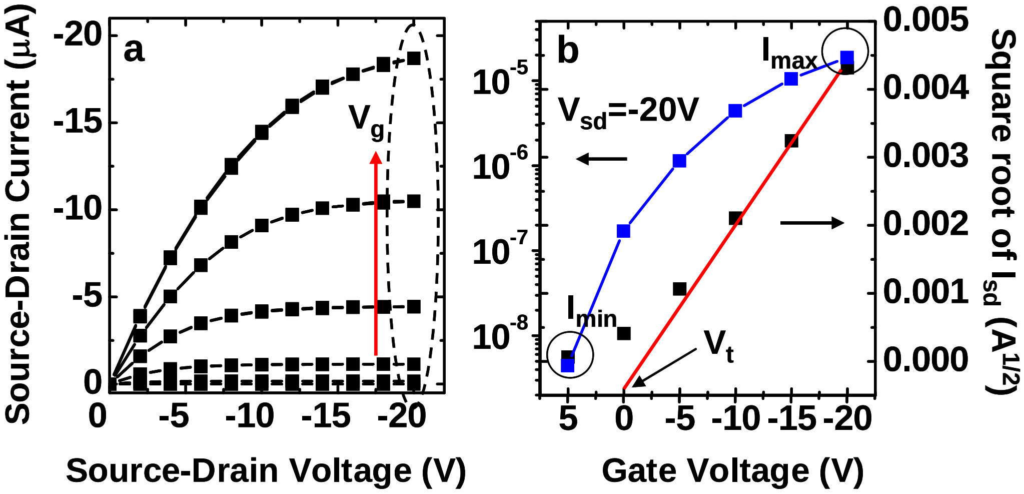

Figure 2.2. (a) Representative I-V characteristics of a pentacene TFT with dichloroacetic acid-treated PANI-PAAMPSA electrodes (L≅100μm; W≅1000μm). Since pentacene has p-channel characteristics, negative V_{sd} and V_g are applied. (b) Transfer characteristics of the TFT. The I_{sd} and its square root at V_{sd} = -20V are plotted as a function of V_g in blue and black dots, respectively. We obtain the on/off current ratio from I_{max} and I_{min} as indicated. The mobility is estimated from the slope of the plot of the square root of I_{sd} as a function of V_g that is indicated with a red line (Equation 2.2). The threshold voltage is extracted from the intercept of the slope with the axis of the gate voltage.

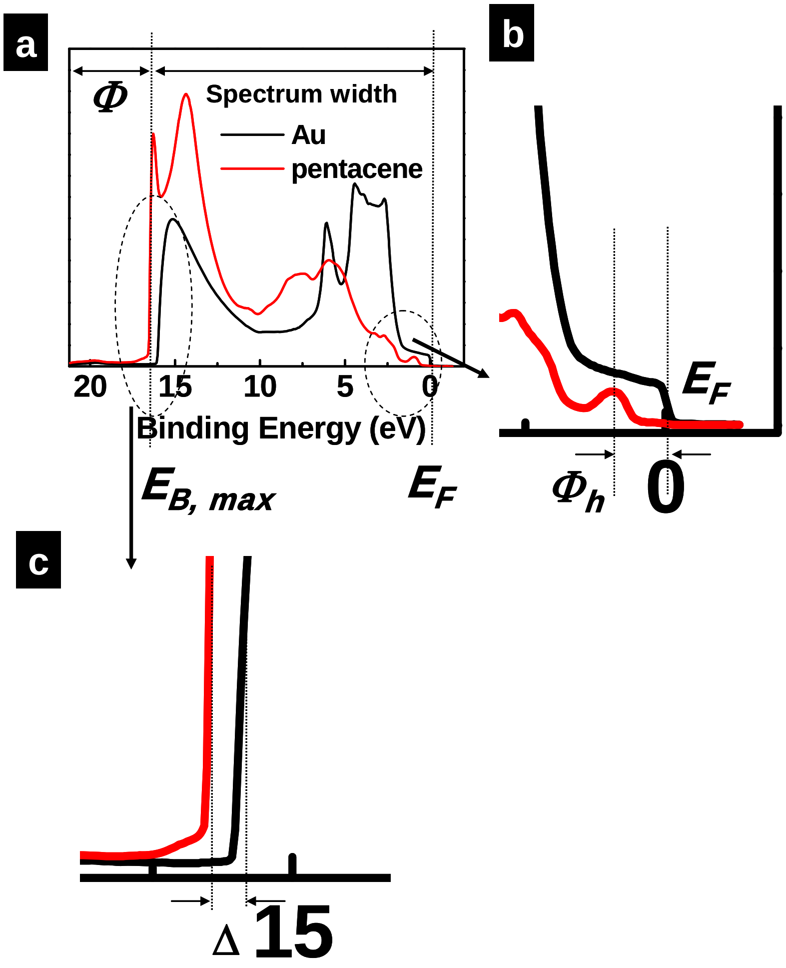

Figure 2.3. (a) Representative UPS spectra of gold (black curve) and pentacene on gold (red curve), (b) The HOMO level of pentacene (Φ_h) is defined as the difference between E_F and the location of the peak maximum in the pentacene spectrum. The position of the peak maximum is determined by fitting the appropriate energy interval with a Gaussian for the peak and a polynomial for background. (c) The interfacial dipole (Δ) between gold and pentacene is defined as the difference in the work functions between gold and pentacene thin film.

REFERENCES

1. J. E. Yoo, J. L. Cross, T. L. Bucholz, K. S. Lee, M. P. Espe, Y.-L. Loo, *Journal of Materials Chemistry* **2007**, *17*, 1268.

2. H. Meng, F. Sun, M. B. Goldfinger, G. D. Jaycox, Z. Li, W. J. Marshall, G. S. Blackman, *Journal of the American Chemical Society* **2005**, *127*, 2406.

3. S. M. Sze, *Physics of Semiconductor Devices*, John Wiley & Sons, Inc., New York **1981**.

4. C. D. Dimitrakopoulos, P. R. L. Malenfant, *Advanced Materials* **2002**, *14*, 99.

5. H. O. Jacobs, H. F. Knapp, A. Stemmer, *Rev. Sci. Instrum.* **1999**, *70*, 1756.

6. S. Sadewasser, M. C. Lux-Steiner, *Phys. Rev. Lett.* **2003**, *91*, 266101.

7. T. J. Smith, K. J. Stevenson, *Rev. Sci. Instrum. in preparation*.

8. D. A. Fischer, B. M. DeKoven, *November 1996 NSLS Newsletter* **1996**.

9. D. A. Krapchetov, H. Ma, A. K. Y. Jen, D. A. Fischer, Y.-L. Loo, *Langmuir* **2005**, *21*, 5887.

10. D. Ross, R. Aroca, *J. Chem. Phys.* **2002**, *117*, 8095.

11. J. Yue, A. J. Epstein, *Macromolecules* **1991**, *24*, 4441.

12. L. Burgi, T. J. Richards, R. H. Friend, H. Sirringhaus, *Journal of Applied Physics* **2003**, *94*, 6129.

Chapter 3: Direct patterning of water-dispersible, conductive polyaniline for organic thin-film transistors

Several patterning techniques have been developed to incorporate conductive polyaniline (PANI) as functional electrodes in organic electronic devices, such as organic thin-film transistors (TFTs).[1-5] To pattern PANI that has a limited solubility, such as PANI doped with hydrochloric and sulfuric acids, several techniques that typically exploit area-selective polymerization of aniline onto specific regions of a previously-patterned molecular template have been developed.[1-5] As mentioned in Chapter 1, molecular templates frequently consist of functionalized thiols on gold or hydrophobic alkyltrichlorosilanes on hydrophilic SiO_x. These molecules are either selectively deposited by microcontact printing[6] or created by first uniformly coating a molecular layer which is then selectively photo-patterned. Most of these techniques[1, 2, 4] rely on the use of gold substrates to electropolymerize aniline. The final conductive PANI features must thus be transferred onto insulating substrates to prevent laterally shorting between individual features. Moreover, polymerization of aniline during patterning significantly limits the ability to control the details of the reaction conditions, so the quality of the resulting PANI cannot be independently optimized. Decoupling aniline polymerization from patterning is thus desirable so the two processes can be tuned independently. Recently, solution-processable, conductive PANI, such as PANI doped with camphor sulfonic acid (CSA) in m-cresol, was directly patterned.[7, 8] These techniques, however, rely on additional chemistries or thermal transfer that may complicate patterning and can be potentially expensive. As a result, a need still exists for methods to direct pattern conductive PANI.

We have developed direct patterning techniques that selectively deposit water-dispersible, conductive PANI on molecular templates.[9] Our ability to directly pattern water-dispersible, conductive PANI is based on the selective adsorption of the polymer in the hydrophilic regions of a molecular template, attributable to the hydrophilic nature of water-dispersible PANI that is template-synthesized with poly(2-acrylamido-2-methyl-1-propane-sulfonic acid) (PANI-PAAMPSA). The resulting PANI-PAAMPSA features are electrically conductive, so they can be readily used as functional components in electronic devices. More importantly, because the patterning scheme involves PANI-PAAMPSA that is polymerized separately, we now have the opportunity to independently examine how the molecular characteristics of PAAAMPSA influences the electrical conductivity (subject of JEY thesis). For example, we recently demonstrated that the conductivity of PANI-PAAMPSA can be improved from 0.1 to 1S/cm by decreasing the molecular weight of PAAMPSA.[10] Our patterning techniques also allows the directly patterning of PANI-PAAMPSA on insulating substrates.[9] As we shall describe in detail, this particular feature of our patterning techniques greatly simplifies device fabrication.

Figure 3.1a illustrates one of the techniques, which we refer to as "stamp-and-spin-cast."[9] Stamp-and-spin-cast begins with the creation of hydroxyl groups on Si/SiO_x substrates through UV/ozone irradiation for 20 minutes. To create a hydrophobic molecular template that repels PANI-PAAMPSA, alkyltrichlorosilanes are microcontact printed[11, 12] onto the hydrophilic SiO_x surface. Specifically, cross-linked polydimethylsiloxane (PDMS)[6] stamps are created by casting and curing the PDMS prepolymer against a master created by conventional optical photolithography.[6] The stamp is inked with 5-10mM of octadecyltrichlorosilane (OTS) in hexanes and then brought into the contact with the substrate for 3-5 minutes. In the regions of stamp-substrate contact, hydrophobic pattern is formed on the substrate. The non-contacted regions on the substrate remain largely hydrophilic. A 5-10wt% PANI-PAAMPSA aqueous dispersion was then be directly spun-cast onto the molecular template. Since PANI-PAAMPSA selectively adsorbs in the hydrophilic regions, a conductive pattern was created immediately after spin-casting. Figures 3.2a and b contain micrographs of an OTS-stamped Si wafer with native silicon oxide (SiO_x) before and after PANI-PAAMPSA deposition, respectively. Specifically, the bright regions in Figure 3.2a represent the regions where OTS is deposited and the dark regions indicate the SiO_x surface that still remains hydrophilic. Figure 3.2b shows that only the dark regions are covered with PANI-PAAMPSA after spin-casting.

During stamping, lateral diffusion of OTS molecules into the non-stamped regions can occur, and this phenomenon often creates undesirable hydrophobic OTS islands within the hydrophilic regions.[12] Although these OTS islands cannot be seen under the optical microscope, the islands prevent PANI-PAAMPSA from adsorbing completely onto the hydrophilic regions during patterning, as shown in Figure 3.3a. These islands, however, can be readily removed by immersing the molecular template in a dilute acid solution (1:10v/v HCl:H_2O) for 3 minutes. This short immersion in HCl does not significantly affect the hydrophobicity of the OTS-stamped regions.[9] The OTS-stamped hydrophobic regions consist of multilayers, as shown in Figure 3.3b. Such multilayer adsorption can result in an increase in the surface roughness that can significantly affect the growth of the organic semiconductor (e.g., pentacene) that is deposited on top during thin-film transistor fabrication.

To create a smoother hydrophobic pattern that still repels PANI-PAAMPSA, hydrophobic molecules, such as OTS, fluorinated alkyltrichlrosilanes, or hexamethyldisilazane (HMDS) can be uniformly vapor-deposited onto hydrophilic Si/SiO_2 substrates. HMDS can also be spin-coated from a concentrated HMDS solution. We then UV/Ozone irradiate the treated substrate through a shadow mask to create the hydrophilic patterns onto which PANI-PAAMPSA will adsorb (Figure 3.1b). In contrast to stamp-and-spin-cast, this technique is subtractive in operation because hydrophobic molecules are first uniformly deposited and then selectively removed to create the same hydrophobic/hydrophilic specificity.

The size of PANI-PAAMPSA features produced by the subtractive patterning scheme (Figure 3.1b) is limited by the resolution of the shadow mask ($\geq$ 100 μm). Finer conductive PANI-PAAMPSA features, as small as 5 μm (Figure 3.4a), can be routinely obtained by stamp-and-spin-cast. The thicknesses of these patterns depend on the lateral feature size, the solution concentration, and the spin speed. For example, the thicknesses of films spun from a 5wt% PANI-PAAMPSA aqueous dispersion range from 200nm to 500nm as the spin-speed is increased from 500 to 5000rpm.

To measure the conductivity of PANI-PAAMPSA, we patterned PANI-PAAMPSA wires using stamp-and-spin-cast. The inset of Figure 3.4b shows an optical micrograph of one such wire. We measured the resistance (*R*) along the length of this wire by which we were able to calculate the conductivity (σ) based on the wire dimensions:

$$\sigma = \frac{L}{RA} \qquad (3.1)$$

where A is the cross-sectional area and L is the length of the PANI-PAAMPSA wire, respectively. PANI-PAAMPSA wires patterned by stamp-and-spin-cast typically exhibit an average electrical conductivity of 0.2S/cm. PANI-PAAMPSA conductivities can also be quantified by four-point probe measurements. Specifically, we deposited four equally-spaced gold strips through a shadow mask directly onto the PANI-PAAMPSA film through a shadow mask. PANI-PAAMPSA film resistance was obtained by dividing the applied current by the voltage drop between the two inner gold strips. Contact resistances between PANI-PAAMPSA and the gold strip, as well as those between the probe tip and the gold strip, could therefore be eliminated. The conductivity was then obtained by normalizing the film resistance by the cross-sectional area defined by the gold strip and the distance between two inner gold strips, as shown in Equation (3.1). We obtained quantitatively comparable values from both the wire conductivity measurements and the four-point probe measurements.

While spin-casting onto circular hydrophilic patterns allows us to create PANI-PAAMPSA features with uniform thicknesses (Figure 3.2b), spin-casting PANI-PAAMPSA onto non-circular molecular templates often result in thickness variations, such as, those shown in Figure 3.5a. This phenomenon stems from non-uniform evaporation rates at the center and at the edges of the substrate during PANI-PAAMPSA spin-casting. To circumvent this non-uniform thickness, we used drop-casting or blade-casting rather than spin-casting to create non-circular PANI-PAAMPSA patterns. Drop-casting begins with covering the entire molecular template with PANI-PAAMPSA aqueous solution using a pipette. Excess solution is then drawn back into the pipette leaving behind PANI-PAAMPSA in the hydrophilic regions only. Blade-casting involves depositing a small amount of PANI-PAAMPSA dispersion on a molecular template and then dragging a credit card with its edges covered with Teflon tape across the substrate. After solvent evaporation, the final solid PANI-PAAMPSA features from both casting techniques exhibit thicknesses that are more uniform than those from spin-casting, as shown in Figures 3.5b and c. For example, a thickness variation, i.e., standard deviation, within a drop-cast feature is ±170nm whereas that within a spun-cast feature in is ±690nm.

To assess the functionality of PANI-PAAMPSA as a conductor in organic thin-film transistors (TFTs), we fabricated pentacene TFTs with PANI-PAAMPSA electrodes. Our ability to directly pattern conductive PAN-PAAMPSA features on a Si/SiO_2 platform facilitates the fabrication of bottom-contact devices (Figure 1.2a). We begin by patterning PANI-PAAMPSA electrodes onto 300nm of SiO_2 thermally-grown on a highly-doped Si substrate (<0.004Ωcm) by using either stamp-and-spin-cast (Figure 3.1a) or the subtractive patterning scheme illustrated in Figure 3.1b. To complete the TFTs, 20-50nm of pentacene is then thermally evaporated onto the channel region through a shadow mask. After stamp-and-spin-cast, pentacene is deposited onto the OTS-stamped SiO_2 surface (Figure 3.1a). If the subtractive scheme is used, pentacene is deposited onto HMDS-treated SiO_2 surface which was created either by vapor deposition in a prime chamber or directly spun cast from a solution (Figure 3.1b).

Figure 3.6a shows representative current-voltage (I-V) characteristics of a bottom-contact pentacene TFT with PANI-PAAMPSA electrodes defined by stamp-and-spin-cast. Of 30 such TFTs tested, the average linear and saturation mobilities were 0.024±0.011 and 0.016±0.008cm^2/V-sec, respectively, and the on/off current ratios were of the order 10^4. These mobilities, however, are significantly lower than those typical of bottom-contact pentacene TFTs, (≅0.1cm^2/V-s).[13] Such reduction in mobility is speculated to stem from the roughness of the stamped OTS multilayers. It has been reported that subtle differences in the dielectric surface roughness can dramatically alter the electrical properties of the organic semiconductor.[14-20] To verify this hypothesis, we measured the surface roughnesses of both the OTS-stamped surface and the HMDS-treated surface using atomic force microscopy (AFM). Figures 3.7a shows the surface topography of the OTS-stamped surface. The root mean square (r.m.s) roughness calculated from a 1×1μm window was found to be 1.4nm on the OTS-stamped surface. In Figure 3.7b, AFM shows that the vapor-deposited HMDS surface is much smoother with a r.m.s roughness of 0.2nm. To examine how these surface roughnesses affect pentacene thin-film morphologies, we imaged pentacene that had been deposited on both the OTS-stamped surface and on the HMDS-treated surface using scanning electron microscopy (SEM). Figure 3.8a shows the SEM image of pentacene on OTS-stamped surface. The average grain size is 200nm. In contrast, much larger dendritic pentacene grains (>1μm) are observed on the HMDS-treated surface, as shown in Figure 3.8b. We attribute this disparity in pentacene grain size to different nucleation densities on the OTS-stamped surface and on the HMDS-treated surface.[21, 22] Consistent with classical nucleation theory,[23] the higher surface energy associated with the rougher surfaces reduces the barrier to nucleation. Since the OTS-stamped surface is significantly rougher than the HMDS-treated surface, it is not surprising that we observe many more grains that are smaller in size on the OTS-stamped surface. Since charge transport is known to be limited by the presence of grain boundaries,[24, 25] it is not surprising that the TFTs built on the OTS-stamped surface exhibit significantly lower mobilities compared to those of the TFTs on HMDS-treated surface.

Figure 3.6b shows representative I-V characteristics of a TFT built on vapor-deposited HMDS vapor-treated Si/SiO_2 substrates. The pentacene layer in this device has large grains and reduced grain boundaries, as shown in Figure 3.8b. The output currents of this TFT as well as others on HMDS-treated surfaces are an order of magnitude higher than those from the TFTs fabricated on OTS-stamped surfaces having the same device geometry and dimensions. The mobilities of TFTs fabricated with PANI-PAAMPSA electrodes defined by the subtractive technique on HMDS-treated surfaces (μ_{lin}=0.19±0.05 and μ_{sat} 0.19±0.06cm^2/V-s) are now comparable with those of typical pentacene TFTs with gold electrodes.

Our results demonstrate the effectiveness of simple, inexpensive techniques for patterning conducting PANI-PAAMPSA. Due to selective wetting and adsorption of PANI-PAAMPSA, conductive PANI-PAAMPSA features can be created in the hydrophilic regions of the molecular template immediately after casting from an aqueous dispersion. The ability to directly pattern PANI-PAAMPSA decouples the details of polymerization from that of processing so both can be optimized independently. Unlike previously demonstrated techniques that rely on conductive substrates, our techniques allow the direct patterning of conductive PANI-PAAMPSA features on insulating substrates. As demonstrated, this feature allows us to directly fabricate pentacene TFTs with PANI-PAAMPSA electrodes on the molecular templates. We found pentacene TFT performance to be limited by the dielectric surface roughness rather than PANI-PAAMPSA contacts, so the roughness of the molecular template would have to be taken into account when choosing the appropriate technique for patterning PANI-PAAMPSA.

FIGURES

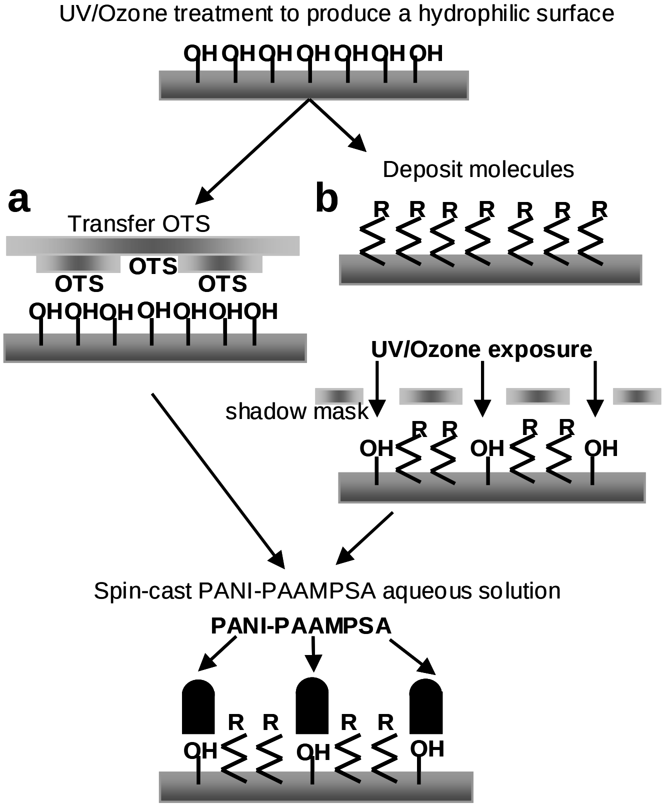

Figure 3.1. Scheme of direct patterning for water-dispersible polyaniline. A hydrophobic OTS pattern is created by either (a) stamping of OTS layer on a hydrophilic substrate via microcontact printing or (b) UV/ozone irradiation of a substrate that had been uniformly treated with a hydrophobic molecular layer (OTS, fluorinated alkyltrichlorosilanes, or HMDS) through a shadow mask. Spin-casting PANI-PAAMPSA aqueous solution onto the molecular template created by (a) or (b), creates conductive PANI-PAAMPSA features in the hydrophilic regions.

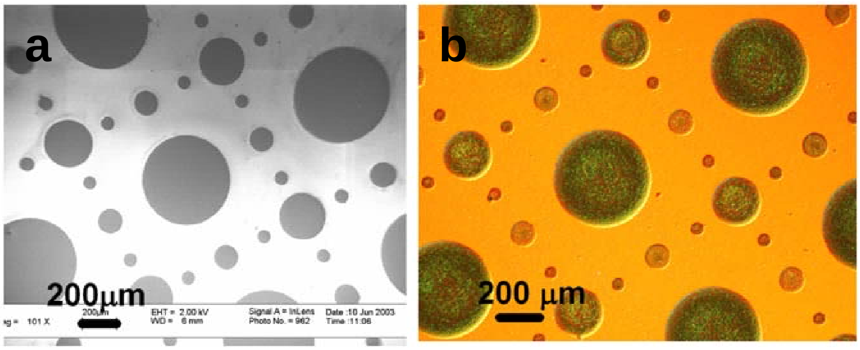

Figure 3.2. (a) Scanning electron micrograph of an OTS-stamped Si/SiO_x substrate. The bright regions indicate OTS-transferred regions (hydrophobic) and the dark regions represent native SiO_x (hydrophilic). (b) Optical micrograph reveals that PANI-PAAMPSA selectively adsorbs in the hydrophilic regions.

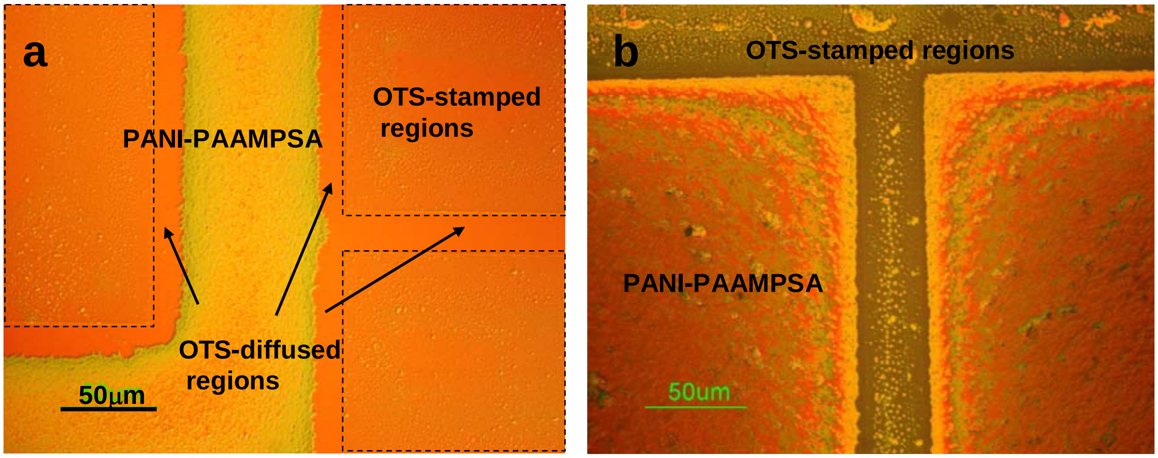

Figure 3.3. (a) During stamping, lateral diffusion of OTS molecules into the non-stamped regions creates undesirable OTS islands. OTS islands prevent PANI-PAAMPSA from adsorbing in the regions indicated by the arrows. PANI-PAAMPSA features are also reduced in size due to the presence of OTS islands near the edges of the OTS-stamped regions. OTS-stamped regions are highlighted by dashed lines for clarity. (b) During stamping, OTS forms multilayers in the regions of contact.

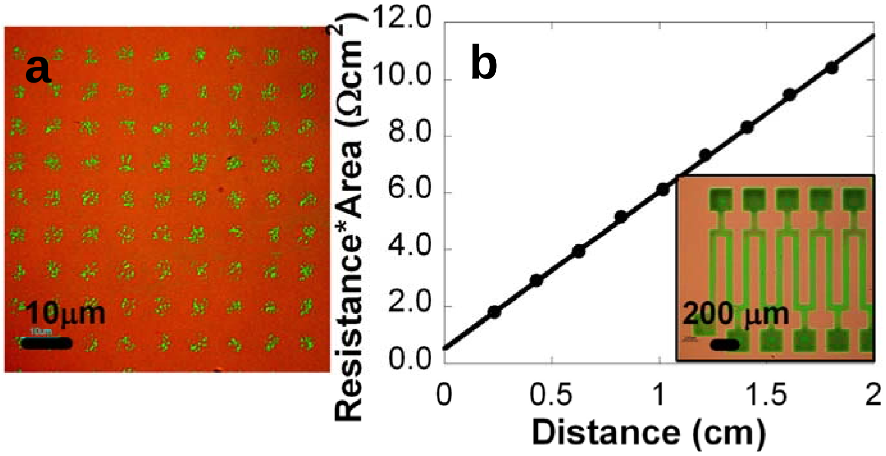

Figure 3.4. (a) Conductive PANI-PAAMPSA features as small as 5μm can be created using stamp-and-spin-cast. (b) The resistance of a PANI-PAAMPSA wire as a function of the wire length. The conductivity of PANI-PAAMPSA wire is extracted from the inverse of the slope. This specific PANI-PAAMPSA wire exhibits a conductivity of 0.2S/cm.

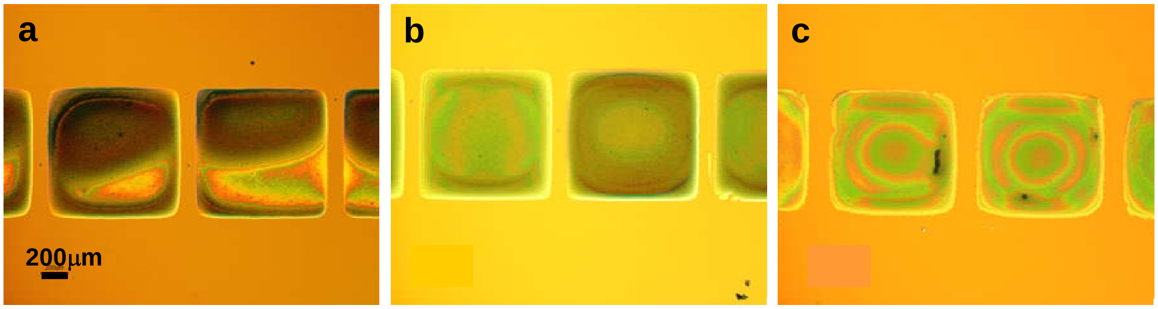

Figure 3.5. PANI-PAAMPSA features created by (a) spin-casting often exhibit thickness variations as indicated by color variation in the optical micrograph. Such variations are minimized in PANI-PAAMPSA features created by (b) drop-casting, and (c) blade-casting.

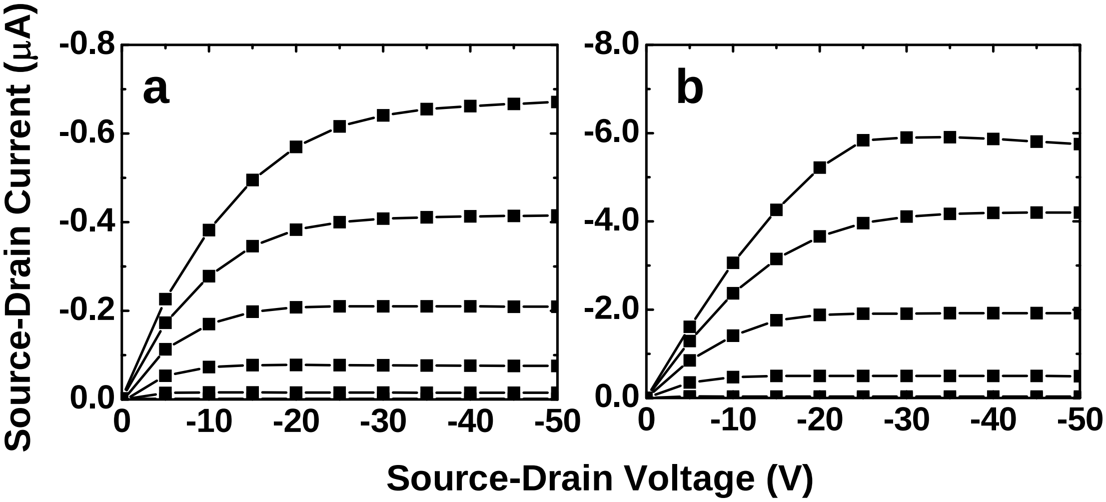

Figure 3.6. I-V characteristics of bottom-contact pentacene TFTs with PANI-PAAMPSA electrodes: PANI-PAAMPSA electrodes are patterned (a) by stamp-and-spin-cast (*W/L* = 950/170μm) and (b) using the subtractive scheme outlined in Fig. 3.1b where the SiO_2 dielectric surface was first vapor-treated with HMDS (*W/L* = 930/150μm). We increased the gate voltage from 0 to -50V in increments of -10V.

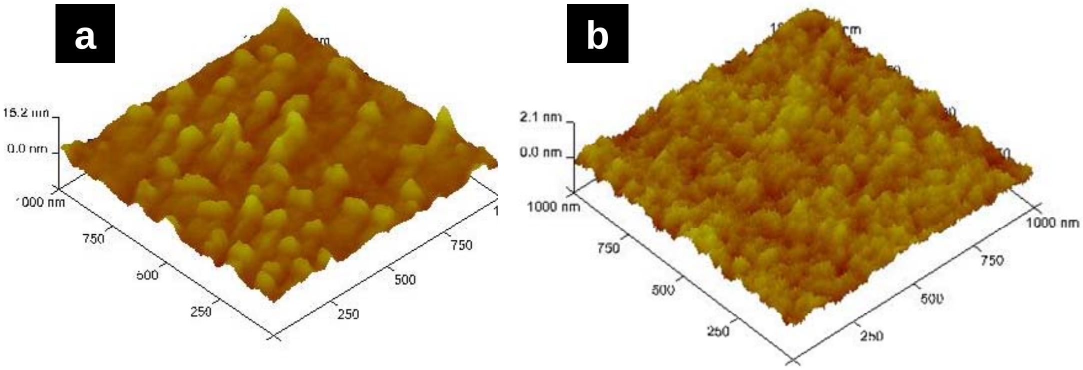

Figure 3.7. AFM reveals the topography of (a) OTS-stamped surface and (b) HMDS-treated surface. The root mean square roughness is found to be 1.4 and 0.2nm on OTS-stamped surface and HMDS-treated surface, respectively.

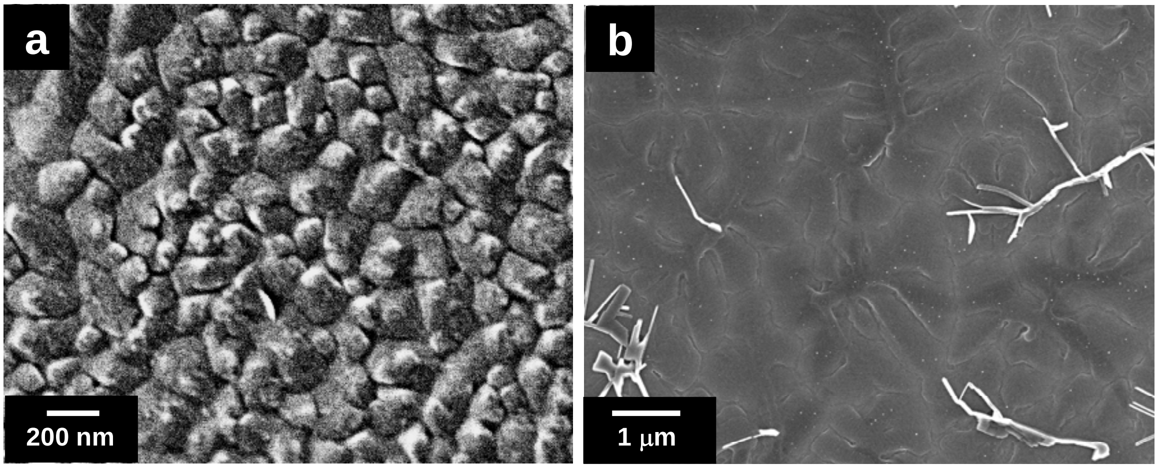

Figure 3.8. SEM reveals the morphologies of 50nm thick pentacene deposited on (a) OTS-stamped surface and (b) vapor-deposited HMDS surface. The average size of pentacene grains is less than 200nm on the OTS-stamped surface. In contrast, pentacene grains are greater than 1μm when deposited on HMDS-treated surface.

REFERENCES

1. D. M. Collard, C. N. Sayre, *Synthetic Metals* **1997**, *84*, 329.
2. C. N. Sayre, D. M. Collard, *Journal of Materials Chemistry* **1997**, *7*, 909.
3. Z. Huang, P.-C. Wang, A. G. MacDiarmid, Y. Xia, G. Whitesides, *Langmuir* **1997**, *13*, 6480.
4. L. F. Rozsnyai, M. S. Wrighton, *Chemistry of Materials* **1996**, *8*, 309.
5. Z. F. Li, E. Ruckenstein, *Macromolecules* **2002**, *35*, 9506.
6. Y. Xia, G. M. Whitesides, *Angewandte Chemie, International Edition* **1998**, *37*, 550.
7. C. J. Drury, C. M. J. Mutsaers, C. M. Hart, M. Matters, D. M. de Leeuw, *Applied Physics Letters* **1998**, *73*, 108.
8. G. B. Blanchet, Y.-L. Loo, J. A. Rogers, F. Gao, C. R. Fincher, *Applied Physics Letters* **2003**, *82*, 463.
9. K. S. Lee, G. B. Blanchet, F. Gao, Y.-L. Loo, *Applied Physics Letters* **2005**, *86*, 074102.
10. J. E. Yoo, J. L. Cross, T. L. Bucholz, K. S. Lee, M. P. Espe, Y.-L. Loo, *Journal of Materials Chemistry* **2007**, *17*, 1268.
11. Y. Xia, M. Mrksich, E. Kim, G. M. Whitesides, *Journal of the American Chemical Society* **1995**, *117*, 9576.
12. N. L. Jeon, K. Finnie, K. Branshaw, R. G. Nuzzo, *Langmuir* **1997**, *13*, 3382.
13. M. Halik, H. Klauk, U. Zschieschang, G. Schmid, W. Radlik, W. Weber, *Advanced Materials* **2002**, *14*, 1717.
14. Y.-Y. Lin, D. J. Gundlach, S. F. Nelson, T. N. Jackson, *IEEE Transactions on Electron Devices* **1997**, *44*, 1325.
15. A. Salleo, M. L. Chabinyc, M. S. Yang, R. A. Street, *Applied Physics Letters* **2002**, *81*, 4383.

16. D. Knipp, R. A. Street, A. Volkel, J. Ho, *Journal of Applied Physics* **2003**, *93*, 347.

17. S. Kobayashi, T. Nishikawa, T. Takenobu, S. Mori, T. Shimoda, T. Mitani, H. Shimotani, N. Yoshimoto, S. Ogawa, Y. Iwasa, *Nature Materials* **2004**, *3*, 317.

18. H. Sirringhaus, P. J. Brown, R. H. Friend, M. M. Nielsen, K. Bechgaard, B. M. W. Langeveld-Voss, A. J. H. Spiering, R. A. J. Janssen, E. W. Meijer, P. Herwig, D. M. De Leeuw, *Nature (London)* **1999**, *401*, 685.

19. M. Shtein, J. Mapel, J. B. Benziger, S. R. Forrest, *Applied Physics Letters* **2002**, *81*, 268.

20. G. B. Blanchet, C. R. Fincher, M. Lefenfeld, J. A. Rogers, *Applied Physics Letters* **2004**, *84*, 296.

21. C. D. Dimitrakopoulos, P. R. L. Malenfant, *Advanced Materials* **2002**, *14*, 99.

22. A. L. Briseno, S. C. B. Mannsfeld, M. M. Ling, S. H. Liu, R. J. Tseng, C. Reese, M. E. Roberts, Y. Yang, F. Wudl, Z. N. Bao, *Nature* **2006**, *444*, 913.

23. J. A. Venables, G. D. T. Spiller, M. Hanbucken, *Reports on Progress in Physics* **1984**, *47*, 399.

24. T. W. Kelley, C. D. Frisbie, *Journal of Physical Chemistry B* **2001**, *105*, 4538.

25. R. A. Street, D. Knipp, A. R. Volkel, *Applied Physics Letters* **2002**, *80*, 1658.

Chapter 4: Characterizing pentacene/polyaniline interfaces in thin-film transistors

While organic semiconductors play an important role as the active charge transporting layers in organic thin film transistors (TFTs), the device performance is not solely governed by the inherent electrical properties of the organic semiconductors. Rather, the performance of organic TFTs can be significantly limited by the organic semiconductor/electrode interface through which charge injection and extraction occur. Such charge transfer can be greatly affected by morphology and grain size of the organic semiconductor thin film at the interfaces. The structure of the organic semiconductor at the interfaces can be significantly influenced by the underlying topography on which the organic semiconductor, which is dictated by the device architectures, i.e., top- vs. bottom-contact devices, as shown in Figure 1.3.[1] For example, in the top-contact device geometry shown in Figure 1.3a, the organic semiconductor layer is deposited on a single gate dielectric surface. This procedure results in a continuous, uniform organic semiconductor layer. In contrast, the bottom-contact device geometry employs a reverse sequence, where the source and drain electrodes are first defined on the gate dielectric surface, and the organic semiconductor is subsequently deposited. As a consequence, the organic semiconductor layer is deposited on two different surfaces: the gate dielectric surface (the channel region) and the electrode surface. Due to topographical differences and the difference in the degree of interaction the organic semiconductor has with the specific surface, the growth of the organic semiconductor can vary significantly in the channel and on the electrodes. For example, Kymissis and coworkers[1] showed that microcrystalline pentacene grains form preferentially on silicon dioxide, while grain growth is greatly suppressed on gold electrodes in bottom-contact TFTs. These TFTs exhibit non-linear current-voltage (I-V) characteristics with "hooking" behavior at small source-drain voltages, attributed to a non-negligible contact resistance at the channel/gold electrode interfaces. Such contact resistance is speculated to stem from the different growth habits of pentacene in the channel and on the gold electrodes. Kymissis and coworkers also improved the mobilities of bottom-contact pentacene TFTs by a factor of three relative to reference bottom-contact TFTs by treating the gold electrode surface with alkylthiols prior to pentacene deposition.[1] Alkylthiols are thought to suppress the interactions between pentacene and gold surface. With alkylthiol treatment, pentacene grains near the gold electrode appear to be as large as those in the middle of channel region, and the organic semiconductor layer appear to be continuous across the channel/electrode interface. This in turn leads to reduced defects that can trap charges at the charge injection and extraction interface, thereby enhancing charge transfer from the gold electrodes to the pentacene layer.

Recent reports[2-4] have suggested that the use of conducting polymer electrodes can also improve device performance in bottom-contact organic TFTs. Such an improvement in device performance is attributable to reduced contact resistances between organic semiconductors and conducting polymers.[2-4] These reports, however, do not provide any detailed structural characterization that elucidates the origin of reduced contact resistance at the channel/electrode interfaces.

In this chapter, we provide a detailed structural characterization of pentacene thin films at the channel/polyaniline (PANI-PAAMPSA) interface in bottom-contact TFTs.

We show a direct correlation between the morphology of the organic semiconductor layer and the device characteristics at small source-drain voltages. By quantifying the surface potentials across the channels of devices under operation, we have identified resistances by which the output currents are limited in each TFT. Suppression of such resistance components limiting the output currents has led to improvement in device characteristics.

PENTACENE THIN-FILM TRANSISTORS

As seen in the previous chapter, PANI-PAAMPSA[5, 6] effectively functions as source and drain electrodes for pentacene TFTs.[5] We also fabricated reference bottom-contact pentacene TFTs with gold source and drain electrodes. For comparison, these TFTs were built under identical conditions. The device geometry and dimensions, such as channel length and width, as well as dielectric treatment are the same for both reference TFTs with gold electrodes, and TFTs with PANI-PAAMPSA electrodes. We found that the TFTs with PANI-PAAMPSA electrodes performed as effectively as those with gold electrodes in the saturated source-drain voltage region. Specifically, bottom-contact pentacene TFTs with gold electrodes and those with PANI-PAAMPSA electrodes exhibited statistically similar saturation mobilities of 0.14±0.05 and 0.19±0.06cm^2/Vs, respectively, when these devices are built on HMDS-treated SiO_2 surfaces.[5] Examining the low source-drain voltage operation (linear) regime, however, revealed significant differences in the I-V characteristics between the TFTs with gold electrodes and those with PANI-PAAMPSA electrodes.

Figures 4.1a and b contain I-V characteristics of bottom-contact pentacene TFTs with gold and PANI-PAAMPSA electrodes in the linear regime, respectively. In the reference TFT, the gold electrodes were fabricated using photolithography and lift-off. The PANI-PAAMPSA electrodes for the TFT were fabricated by the subtractive patterning technique outlined in Figure 3.1b.[7] To ensure that the details of gate dielectric treatment are identical for both TFTs, we created the molecular template for PANI-PAAMPSA patterning by photolithography and lift-off. Specifically, we started by irradiating the substrate with UV/Ozone for 20min. A concentrated hexamethyl disilazane (HMDS 99.9%, Aldrich) was then spin-coated on the substrate at 3000rpm for 60s. This was followed by the deposition of a thin layer of photoresist (AZ® 5214-E photoresist, Clariant Corporation). The photoresist was exposed to a UV flood source (365nm) through a photomask. After exposure, the substrates were immersed in a developer (AZ® 400K developer, Clariant Corporation). We found that the developer not only strips off the exposed AZ photoresist, it also readily strips off the underlying HMDS. The exposed and developed regions thus became hydrophilic. To remove the photoresist in the unexposed regions, we rinsed the substrate with acetone. Since acetone does not remove adsorbed HMDS, these regions remained hydrophobic. Following HMDS pattern definition on the substrate, a 5wt% PANI-PAAMPSA aqueous solution was then spun-cast on the molecular template. Since PANI-PAAMPSA selectively adsorbs in the hydrophilic regions,[5] conductive PANI-PAAMPSA features in the pre-defined geometry of source and drain electrodes were created immediately after spin-coating.

Both these TFTs have the same channel dimensions with L=120 and W=1000μm. In Figure 4.1, we observe that the TFT with gold electrodes exhibit lower output currents at a given input voltage, compared to the TFT with PANI-PAAMPSA electrodes.

Additionally, the I-V characteristics of the TFT with gold electrodes appear to be non-linear. Such “hooking” behavior is not surprising and is commonly reported for bottom-contact organic TFTs with gold electrodes.[1, 8] This phenomenon is believed to stem from large contact resistance at the pentacene/gold electrode interface.[1] On the contrary, this behavior is not observed in the I-V characteristics of the bottom-contact pentacene TFT with PANI-PAAMPSA electrodes, as shown in Figure 4.1b. Likewise, the absence of non-linear I-V characteristics can be attributed to a reduced contact resistance at the pentacene/PANI-PAAMPSA interface.

We carried out scanning electron microscopy (SEM) experiments to examine the pentacene thin-film morphologies at the channel/gold and at the channel/PANI-PAAMPSA interfaces in the TFTs whose I-V characteristics are shown in Figures 4.1a and b, respectively. Figure 4.2a reveals the morphology of pentacene that is deposited at the channel/gold interface in the TFT with gold electrodes. In the channel region, the pentacene grain size ranges from 0.5 to 1μm.[7, 9] The morphology of pentacene on gold, on the other hand, is quite different. On gold, pentacene appears to form small, round grains on the order of 100nm in diameter.[1, 7, 10] Figure 4.2b reveals slightly larger pentacene grains (200-500nm) on PANI-PAAMPSA in the TFT with PANI-PAAMPSA electrodes. The pentacene grains on PANI-PAAMPSA appear to conform to the topography of the PANI-PAAMPSA surface. The morphology of pentacene in the channel region of this TFT appears to be similar to that is the channel regions to the TFT with gold electrode. The difference in pentacene growth habit is most pronounced at the gold/channel interface. Specifically, we observe disconnected grains across the channel/gold interface (Figure 4.2a). This discontinuity necessarily induces structural disorder, which is speculated to be responsible for the large contact resistance reported in bottom-contact organic TFTs with gold electrodes.[1, 10] Such discontinuity within the pentacene thin film, however, is not observed at the channel/PANI-PAAMPSA interface where individual grains appear to traverse the interface. We correlate the reduced contact resistance to the continuity of grains across the pentacene/PANI-PAAMPSA interface (Figure 4.2b).

Interestingly, the ensemble-average molecular orientation of pentacene is also different when pentacene is deposited on PANI-PAAMPSA, compared to when pentacene is deposited on gold. To quantify the ensemble-average orientation of pentacene, we carried out near-edge x-ray adsorption fine structure spectroscopy (NEXAFS) experiments[11] at the carbon edge on pentacene thin films deposited on the different substrates. These NEXAFS experiments were performed in collaboration with Dr. Kimberly Dickey, a former graduate student in our group. We examined thin films of thermally-evaporated pentacene on HMDS-treated Si surface with native oxide (analogous to the channel region), on gold, and on PANI-PAAMPSA. Figure 4.3a shows the pre- and post-edge normalized carbon-edge NEXAFS spectra of pentacene deposited on HMDS-treated Si at different angles of incidence (defined as the angle from the substrate normal). We identify the two sharp peaks at 284 and 285eV as $C1s \rightarrow \pi^*$ transitions of the fused rings of pentacene.[12] The two broader peaks, which are observed at 294 and 301eV, are associated with $C1s \rightarrow \sigma^*$ transitions of pentacene.[12, 13] As the incident angle is increased from 20° (glancing), to 50° and 75° (nearly perpendicular to the substrate), the π^* intensities of the rings increase; this is accompanied by a decrease in the σ^* intensities. Figure 4.3d contains the integrated π^* intensity of the peak at

284eV as a function of incident angle for pentacene on HMDS-treated Si. The positive slope in Figure 4.3d indicates that the rings of pentacene are preferentially oriented upright with respect to the silicon substrate.[12] This preferential orientation is desirable, particularly in the channel region, as it promotes lateral π-π overlap of pentacene molecules, which can enhance charge transport across the channel.[12] In contrast, when pentacene is deposited on gold, the molecular orientation is dramatically different. This is first seen in the pre- and post-edge normalized NEXAFS spectra in Figure 4.3b, where the π* intensities decreases, and the σ* intensities increases with increasing incident angle. The integrated π* intensity is presented in Figure 4.3e. Contrary to the corresponding picture of pentacene on HMDS-treated Si, the negative slope indicates that the rings of pentacene are preferentially oriented parallel to the substrate.[14] When pentacene is deposited on PANI-PAAMPSA, however, the integrated π* intensity increase with increasing incident angles (Figure 4.3c and f), i.e., pentacene appears to adopt the same preferential upright preferential orientation when deposited on PANI-PAAMPSA as when it is deposited on HMDS-treated Si.

Our NEXAFS results indicate that the molecular orientation of pentacene must change dramatically – from rings perpendicular to the substrate to rings parallel – across the channel-electrode interface in devices with gold electrodes. In contrast, pentacene is organized in the same orientation across the channel-electrode interface in TFTs with PANI-PAAMPSA electrodes. It has been speculated that the details of molecular orientation of the organic semiconductor can drastically affect charge injection and lateral charge transport within the thin film.[12, 15] That pentacene maintains the same molecular orientation across the charge transfer interface in the TFT with PANI-PAAMPSA electrodes should enhance device characteristics. At the pentacene-gold interface, however, the abrupt change in the ring orientation is likely to hamper charge transfer between pentacene and gold in these devices.

To directly map the surface potential of our TFTs during operation, we conducted scanning surface potential microscopy (SSPM)[16] experiments on our TFTs in collaboration with Timothy J. Smith in Professor Keith Stevenson's group in the Department of Chemistry and Biochemistry.[7] Using SSPM, we are able to separate the potential drops associated with the contact resistances at pentacene/electrode interfaces from those associated with the channel resistance of pentacene. Any potential drops attributable to the bulk resistance of electrodes can be further decoupled from the total potential drop. We then calculate the individual resistances by normalizing the respective potential drops by the output currents that are measured concurrently during the SSPM experiments.

The bottom-contact pentacene TFTs whose device characterization are shown in Figure 4.1 were examined by SSPM. During SSPM, both the topography and the surface potential distribution across the channels were measured in an interleaved fashion while devices were in operation. Due to size limitation of the scan window (≈100μm), we scanned each of the channel-electrode interfaces separately to span the entire channel region for TFTs having channel lengths greater than 100μm. To capture the surface potential in the linear regime, we applied a constant source-drain voltage of -5V, and systematically increased the gate voltage in increments of -10V, ranging from -10 to -50V. We first acquired the topography profiles of the channel regions of these TFTs (Figures 4.4a and b), then probed the surface potentials across the channel, as shown in

Figures 4.4c and d. For purpose of clarity, we highlighted the channel region (L=120μm) for each TFT in Figure 4.4. The edges of the highlighted regions are thus the interfaces of interest. The topography profile in Figure 4.4a shows gold source and drain electrodes with sharp edges resulting from photolithography and liftoff. Figure 4.4b, however, shows taller PANI-PAAMPSA source and drain electrodes (≈500nm, as opposed to 150nm) with diffused edges due to the nature of the subtractive patterning process used to deposit PANI-PAAMPSA.[5] In Figure 4.4c, a series of surface potential profiles reveals how the -5V bias applied between the source and drain electrodes is distributed across the channel region as the gate voltage is increased. At a gate voltage of -50V, for example, we observe relatively flat potentials from the gold source contact on the right side, then a sharp drop at the pentacene-gold source interface. A gradual surface potential drop occurs across the channel followed by another sharp drop at the pentacene-gold drain interface. There is negligible potential drop at the gold drain electrode. The sharp potential drops at the pentacene-gold source interface and at the pentacene-gold drain interface are labeled as ΔV_s and ΔV_d, respectively; the gradual potential drop in the channel is label as ΔV_{ch} in Figure 4.4c.

Figure 4.4d reveals the surface potential profiles acquired in a bottom-contact pentacene TFT with PANI-PAAMPSA source and drain electrodes. In this TFT, the dominant potential drop occurs across the channel region without any significant potential drops at either of the pentacene/PANI-PAAMPSA interfaces. This phenomenon indicates that the output currents are mainly limited by pentacene in the channel, and not by the pentacene/PANI-PAAMPSA interface. The potential drops in the channel, at the channel/PANI-PAAMPSA source electrode, and at the channel/PANI-

PAAMPSA drain electrode are also labeled as ΔV_{ch}, ΔV_s and ΔV_d, respectively in Figure 4.4d.

To quantify the individual resistances that comprise the total resistance of each TFT, we used a simple model of five resistors in series, as shown in Figure 4.5a. The total resistance consists of the bulk resistance of the drain electrode (R_1), the contact resistance at the pentacene-drain interface (R_2), the channel resistance (R_3), the contact resistance at the pentacene-source interface (R_4), and the bulk resistance of the source electrode (R_5). The individual resistances were quantified by normalizing each of the potential drops by the source-drain current measured concurrently during SSPM. Our experimental setup allows us to directly measure R_2, R_3, and R_4, which are highlighted in Figure 4.5a. The sum of R_1 and R_5 are measured with a potential drop along the source and drain electrodes. This potential drop is obtained by subtracting a potential within the two channel/electrode interfaces from the total potential (-5V). The channel resistance (R_3) and the sum of the contact resistance (R_2+R_4) are plotted as a function of the gate voltage for the TFTs with gold and PANI-PAAMPSA electrodes in Figures 4.5b and c, respectively. We observe that both the channel resistance and the sum of the contact resistances decrease with increasing gate bias. In the TFT with gold electrodes, the sum of the contact resistance ($R_2+R_4 \cong 580$kΩcm at a gate voltage of -50V) is more than half that of the channel resistance ($R_3 \cong 910$kΩcm at the same gate voltage) as the gate voltage is increased. This device is therefore contact-limited, and this phenomenon is entirely consistent with the electrical characterization shown in Figure 4.1a. This observation is also consistent with previous reports for bottom-contact organic TFTs with metal electrodes.[2, 4, 8, 17, 18] On the other hand, the contact resistance of the pentacene TFT with

PANI-PAAMPSA electrodes appears to be significantly lower than the channel resistance at all gate voltages. At gate bias of -50V, for example, the sum total of the contact resistance at the pentacene/PANI-PAAMPSA interfaces (26kΩcm) is nearly an order of magnitude lower than the channel resistance (290kΩcm).[7] The reduced contact resistance indicates that the current output from the TFT with PANI-PAAMPSA electrodes is not limited at the pentacene/PANI-PAAMPSA interfaces. The reduced contact resistance in this device can be correlated with the molecular structures of pentacene at the channel/PANI-PAAMPSA interface. Specifically, pentacene grains are well-connected at this interface. These pentacene rings are preferentially oriented perpendicular to the channel and on PANI-PAAMPSA surface. The perpendicular orientation is preferred for efficient lateral charge transfer through pentacene molecules.[15, 19] The preservation of such orientation across the channel and PANI-PAAMPSA can significantly reduce defects that can trap charges during device operation.

As just mentioned, there can exist potential drops along source and drain electrodes, each of which span 7mm from the channel/electrodes interfaces. Since goid is not resistive, the -5V bias applied between the ends of the gold source and drain electrodes is only dropped across the scan window, i.e., these is insignificant potential drop along the electrodes (R_1 and $R_5 \cong 0$). On the other hand, PANI-PAAMPSA is significantly more resistive compared to gold (0.2S/cm as opposed to ~10^6S/cm),[5] so a -5V bias that is applied across the TFT with PANI-PAAMPSA electrodes is dropped both along the electrodes outside the scan window. This resistance, R_1+R_5, can be calculated by normalizing the potential drop outside the scan window by the current output measured during the SSPM experiments. To complete our results, we have also plotted this value in Figure 4.5c. This resistance is largely gate bias independent (≈180kΩcm) as it originates from the bulk resistance of PANI-PAAMPSA. For comparison, Table 4.1 summarizes the contact resistance (R_2+R_4), the channel resistance (R_3), and the bulk resistance of electrode (R_1+R_5) of pentacene TFTs with gold electrodes and PANI-PAAMPSA electrodes at a gate voltage of -50V. While the TFT with PANI-PAAMPSA electrodes is not contact limited, its performance appears to be limited by the bulk resistance of the PANI-PAAMPSA electrodes. This result implicates the importance of improving the conductivity of PANI-PAAMPSA; our efforts in this area are detailed in Chapter 5.

Table 4.1 - Summary of contact resistance (R_2+R_4), channel resistance (R_3), and bulk resistance (R_1+R_5) of pentacene TFTs with gold electrodes and PANI-PAAMPSA electrodes at a gate voltage of -50V.

At V_g=-50V	R_2+R_4 (kΩcm)	R_3 (kΩcm)	R_1+R_5 (kΩcm)
gold	580	910[a]	negligible
PANI-PAAMPSA	26	290[a]	180

[a] While the linear mobility of the two devices extracted from the I-V characteristics are comparable, the channel resistance in the device with gold electrodes appear significantly higher than that in the device with PANI-PAAMPSA electrodes. We believe this is because the SSPM measurements were carried out approximately one week after the TFTs were made and tested electrically. The SSPM output characteristics reveal a 58% reduction in linear mobility for the TFT with gold electrodes and insignificant reduction in the device with PANI-PAAMPSA electrodes.

Our characterization indicates that it is crucial to understand the molecular structures of organic semiconductor at the channel/electrode interfaces because they can be directly correlated with the charge transfer properties at these interfaces. Such understanding will provide us with the ability to choose an "appropriate" combination of materials or processing conditions to control the structure of organic semiconductor thin films thereby can optimize device performance.

ASYMMETRIC PENTACENE THIN-FILM TRANSISTORS WITH ONE GOLD AND ONE PANI-PAAMPSA-COATED GOLD ELECTRODE

Our characterization of bottom-contact pentacene TFTs indicates that the use of PANI-PAAMPSA significantly reduces contact resistance at the channel-electrode interfaces. A non-negligible potential drop, however, is observed along the PANI-PAAMPSA electrodes, attributed to the bulk resistance of PANI-PAAMPSA. In a single device, the impact of potential drops along PANI-PAAMPSA electrodes on device performance is minimal. These potential drops will, however, result in significant reduction in current output when multiple devices are connected with PANI-PAAMPSA wires. To minimize the bulk resistance of PANI-PAAMPSA, we employed gold electrode beneath PANI-PAAMPSA. The use of PANI-PAAMPSA-coated gold electrodes eliminates the bulk resistance associated with these wires while still maintaining low contact resistance at the channel/electrode interface. To create these electrodes, PANI-PAAMPSA is spun-cast onto gold electrodes from an aqueous dispersion. Since clean gold surfaces are hydrophilic, PANI-PAAMPSA effectively coats the gold surface, and not the gate dielectric surface that is pre-coated with hydrophobic molecules.

To effectively compare I-V characteristics and contact resistances between gold and PANI-PAAMPSA-coated gold electrodes in bottom-contact pentacene TFTs, we fabricated asymmetric devices in which one electrode is made of gold and one electrode of PANI-PAAMPSA-coated gold. We begin by defining two gold electrodes on Si/SiO_2 substrates using photolithography and lift-off. To create asymmetric devices, we covered one electrode with Teflon tape. PANI-PAAMPSA aqueous dispersion is spun on the other gold electrode that is exposed. Pentacene is thermally evaporated in the channel region through a shadow mask. The resulting device thus consists of one gold electrode and one PANI-PAAMPSA-coated gold electrode contacting the same pentacene layer, as shown in Figure 4.6a. In Figure 4.6b, an SEM micrograph reveals the underlying gold electrode. Figure 4.6c confirms that PANI-PAAMPSA completely covers the edge of the gold electrode. Charge transfer to pentacene during device operation therefore occurs through PANI-PAAMPSA, and not directly from gold. Figure 4.7 contains representative I-V characteristics of an asymmetric pentacene TFT in the linear regime. When we operate the TFT with PANI-PAAMPSA-coated gold as the source electrode and gold as the drain electrode, we observe I-V characteristics that are represented by the green curves in Figure 4.7. When the electrical connections are switched around, i.e., with gold acting as the source electrode and PANI-PAAMPSA-coated gold as the drain electrode, the output currents decrease, especially at high gate voltages, as depicted by the yellow curves in Figure 4.7.

We also carried out SSPM during the operation of an asymmetric pentacene TFT whose I-V characteristics are shown in Figure 4.7. Figure 4.8a shows the optical micrograph of the channel region of an asymmetric TFT with one gold electrode and one

PANI-PAAMPSA-coated gold electrode prior to pentacene deposition. Figure 4.8b reveals the topography of pentacene in the channel region of the asymmetric device. Figure 4.8c shows how a -5V bias is distributed across the channel when the asymmetric device operates with PANI-PAAMPSA-coated gold as the source electrode and gold as the drain electrode. The gate bias is increased from 0 to -50V in steps of -5V. The potential distribution at each gate bias is offset for clarity. Unlike the surface potential profiles of the pentacene TFT with PANI-PAAMPSA source and drain electrodes (Figure 4.4d), the entire -5V bias is dropped with the scan window in this TFT. This observation indicates that the underlying gold electrode effectively minimizes any additional potential drops associated with the bulk resistance of PANI-PAAMPSA. Consistent with previous observations, we observe negligible potential drops at the pentacene/PANI-PAAMPSA-coated gold source interface, but a large potential drops at the pentacene/gold drain interface. When we switch the electrical connections on the TFT, a sharp potential drop is observed only at the pentacene/gold source interface but not the pentacene/PANI-PAAMPSA-coated gold drain interface. The individual resistance in the TFT was quantified per previous discussion, and plotted in Figure 4.9. The bulk resistance (R_1+R_5) in Figure 4.5a can now be eliminated with the use of PANI-PAAMPSA-coated gold electrode. We therefore used three resistors in series to model the resistance distribution in our asymmetric TFTs, as shown in Figure 4.9a. The resistances extracted from the surface potential profile in Figures 4.8c and d shows that the channel resistance (R_3) remains constant whether PANI-PAAMPSA-coated gold is used as the source or the drain electrode. At most gate biases, the contact resistance (R_4) at the pentacene/gold interface is more than five-fold higher than the contact resistance (R_2) at the pentacene/PANI-PAAMPSA-coated gold interface. This observation indicates that the output currents from the asymmetric TFT are mainly limited by the channel/gold interface. Specifically, Table 4.2 summarizes the source contact resistance, the drain contact resistance, and the channel resistance extracted from the asymmetric pentacene TFTs at a gate voltage of -50V. Both gold and PANI-PAAMPSA-coated gold electrodes exhibit higher contact resistances when they are used as the source electrode compared those when they are used as the drain electrode. This observation indicates that charge injection from the electrode to pentacene is more difficult than charge extraction from pentacene to the electrode.[20, 21]

The use of an underlying gold layer allows us to effectively minimize the effect of high bulk resistance of PANI-PAAMPSA during device operation. We are thus able to effectively quantify the contact resistances that are decoupled from the bulk resistance of PANI-PAAMPASA. The asymmetric device geometry provided an efficient tool to comparatively study the contact resistances of two different electrodes. Specifically, we identified more than five-fold higher contact resistance at the pentacene/gold interface compared to that at pentacene/PANI-PAAMPSA-coated gold. The charge injection is shown to be more difficult than the charge extraction at both the pentacene/gold and the pentacene/PANI-PAAMPSA-coated gold electrodes.

Table 4.2 - Summary of contact resistance at the pentacene/PANI-PAAMPSA-coated gold interface (R_2), contact resistance at the pentacene/gold interface (R_4), and channel resistance (R_3) in an asymmetric pentacene TFT when operated in two different electrical connections at a gate voltage of -50V.

At V_g=-50V	R_2 (kΩcm)	R_4 (kΩcm)	R_3 (kΩcm)
Gold source, PANI-PAAMPSA drain	3.6	96	320
PANI-PAAMPSA source, gold drain	7.4	38	340

FIGURES

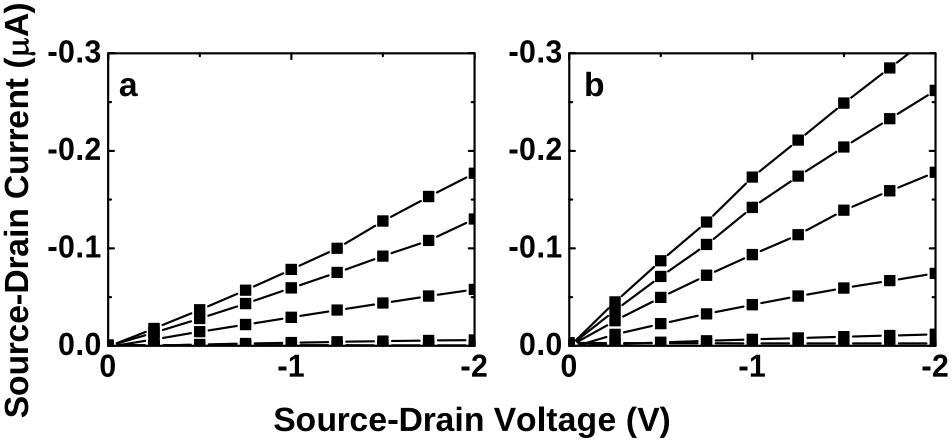

Figure 4.1. Linear-regime I-V characteristics of two pentacene TFTs with the same channel dimensions (L=120μm and W=1000μm), with (a) gold source and drain electrodes (μ_{lin}=0.03cm^2/V-s) and (b) PANI-PAAMPSA electrodes (μ_{lin}=0.05cm^2/V-s). We increased the gate voltage from 0V to -50V in increments of -10V.

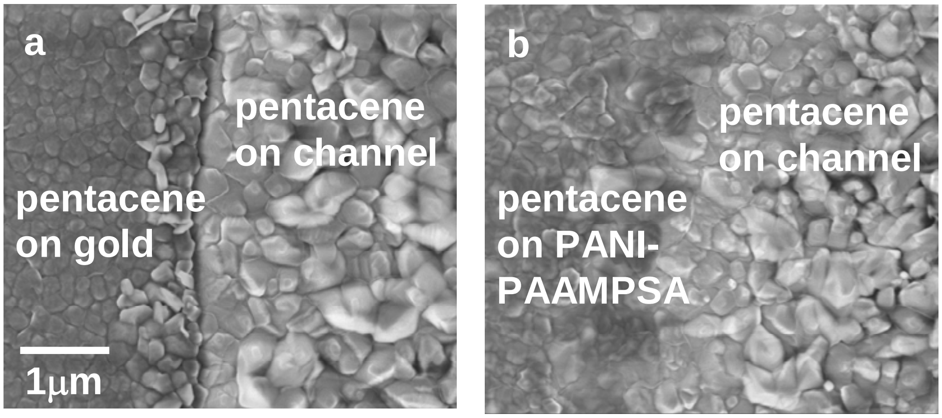

Figure 4.2. SEM micrographs of pentacene at (a) the SiO2-gold interface and (b) the SiO2-PANI-PAAMPSA interface.

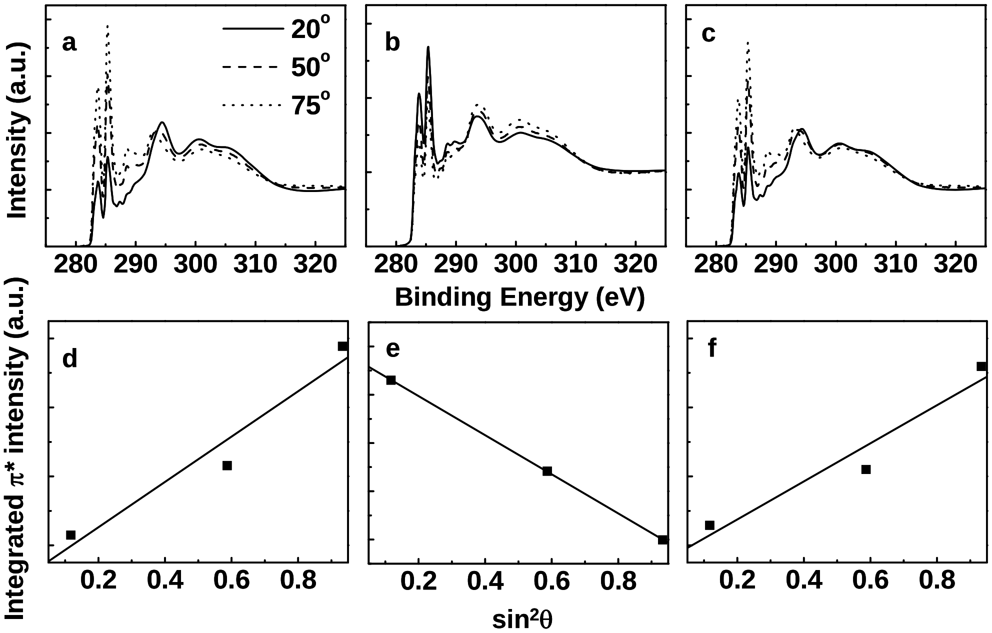

Figure 4.3. Pre- and post-edge normalized angle-dependent carbon-edge NEXAFS spectra of pentacene on (a) HMDS-treated Si, (b) on gold, and (c) on PANI-PAAMPSA. The respective integrated intensity of the peak associated with C1s→π* transition at 284eV is plotted as a function of x-ray incident angle in (d) through (f).

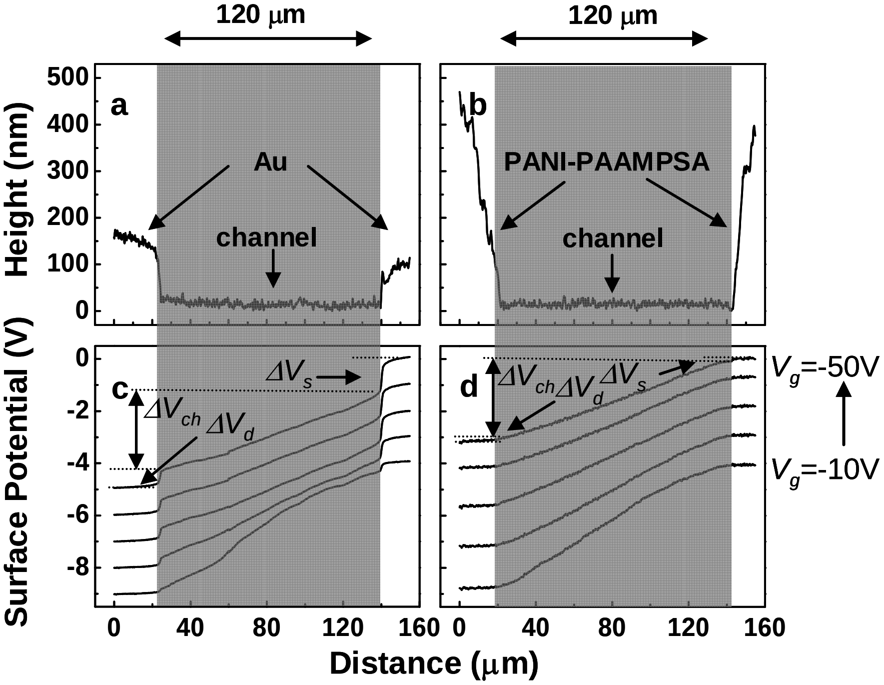

Figure 4.4. Surface topography (a, b) and surface potential (c,d) profiles of the two TFTs whose I-V characteristics are shown in Figure 1. The profiles on the left are acquired on the TFT with gold electrodes whereas the profiles on the right are acquired during the operation of the TFT with PANI-PAAMPSA electrodes. The TFTs are operated at V_{sd}=-5V while V_g is increased in increments of -10V. The surface potential profiles have been offset along the y-axis for clarity.

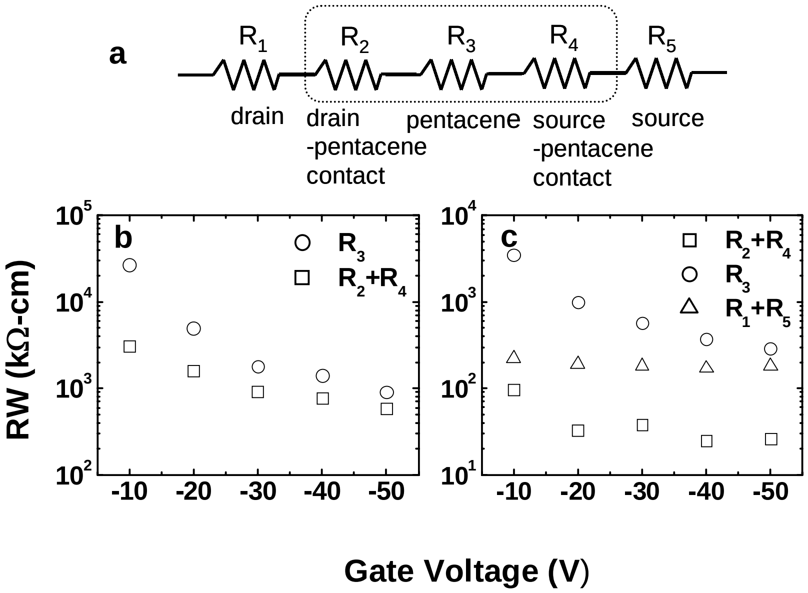

Figure 4.5. The organic TFTs are modeled as five resistors wired in series, as shown in (a). Dashed line defines the scan window. The contact resistance in the TFT with gold electrodes (*L*=120μm and *W*=1000μm) becomes comparable with the channel resistance at high gate voltages, as shown in (b). Although the contact resistance in the TFT with PANI-PAAMPSA electrodes is small compared to the channel resistance, the bulk resistance of PANI-PAAMPSA electrodes is significant and appears to dominate device performance at high gate voltages, as shown in (c).

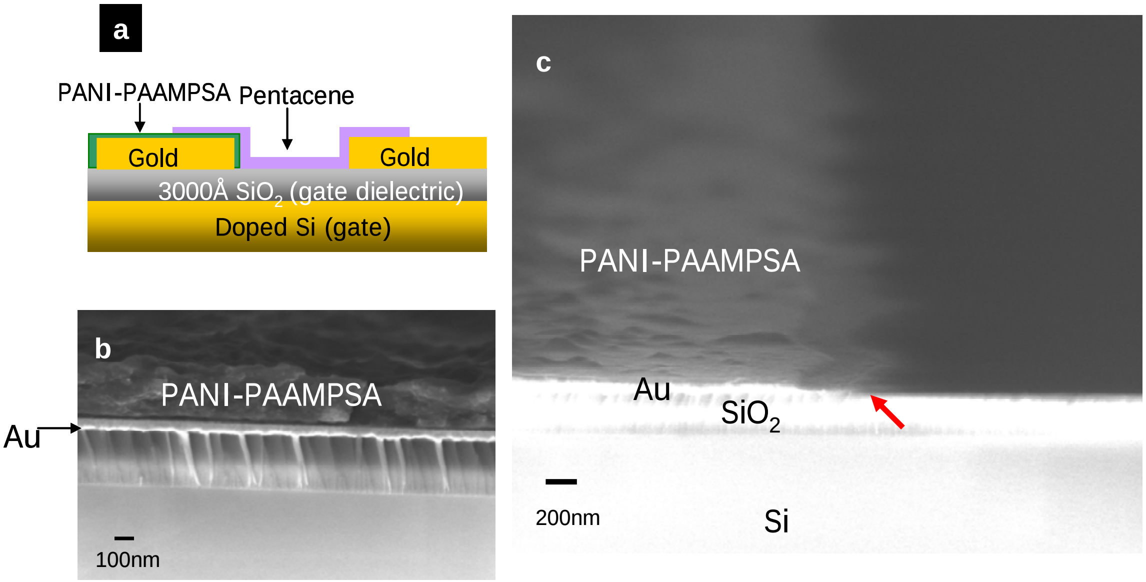

Figure 4.6. (a) Schematic of a pentacene TFT with one gold electrode and PANI-PAAMPSA-coated gold electrode, (b) cross-sectional SEM image of PANI-PAAMPSA-coated gold electrode, (c) PANI-PAAMPSA completely covers the edge of the underlying gold electrode as indicated by the red arrow in this SEM image.

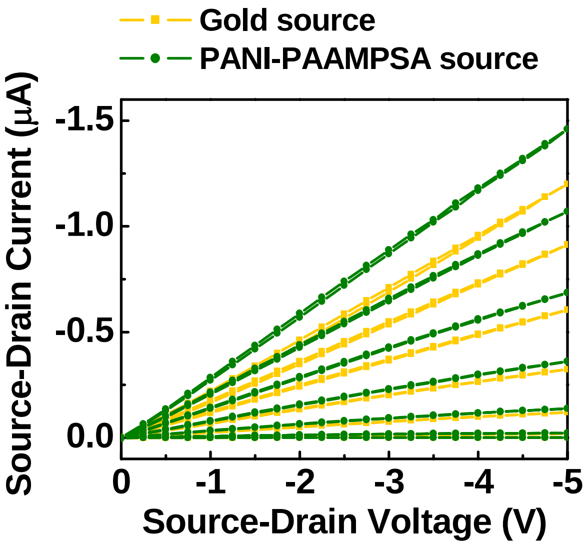

Figure 4.7. Representative linear regime I-V characteristics of an asymmetric pentacene TFT (*L*≅200μm and *W*≅1000μm) with PANI-PAAMPSA as the source electrode and gold as the drain electrode (green curves); and vice versa (yellow curves).

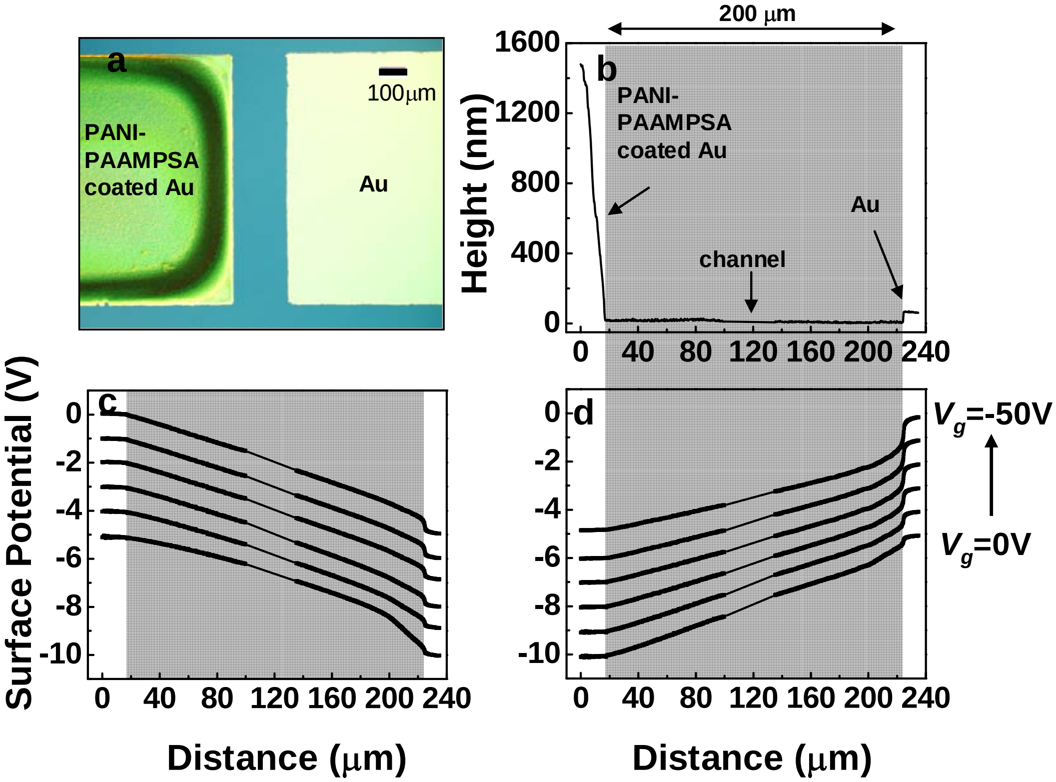

Figure 4.8. (a) Optical micrograph of the channel region of an asymmetric device with one gold electrode and one PANI-PAAMPSA-coated gold electrode prior to pentacene deposition. (b) Topography of the asymmetric pentacene TFT as probed by SSPM. (c) Surface potential profiles reveal sharp potential drops at the channel/gold interface when the device operates with PANI-PAAMPSA-coated gold electrode as the source and gold electrode as the drain. (d) Such potential drops are still at the channel-gold interface when the electrical connections are flipped, i.e., gold electrode as the source and PANI-PAAMPSA-coated gold electrode as the drain. The TFT was operated at V_{sd} = -5V while Vg is increased in increments of -10V. The channel regions (L≅200μm) are highlighted for clarity.

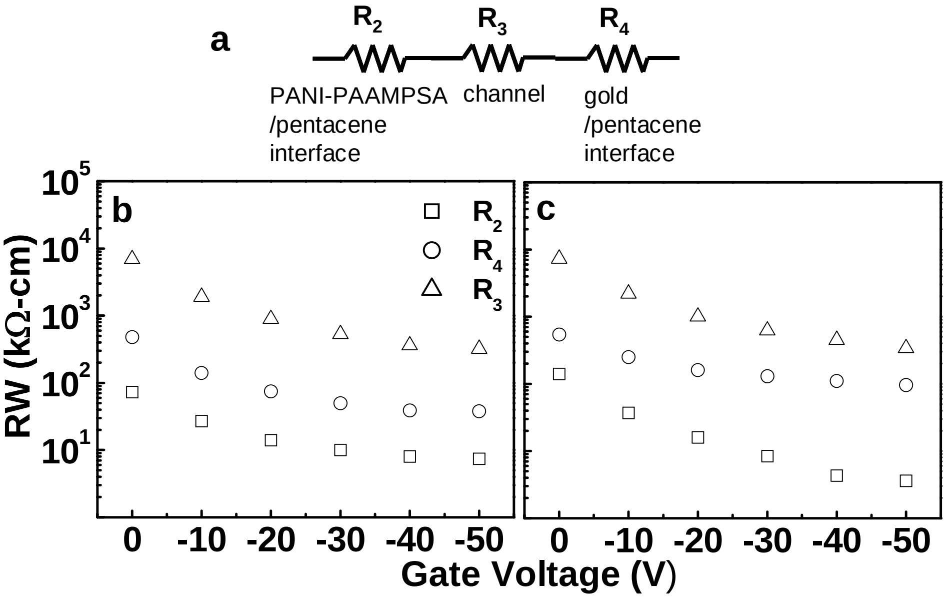

Figure 4.9. (a) Three resistors-in-series is used to model the asymmetric pentacene TFT with one gold electrode and one PANI-PAAMPSA-coated gold electrode. The individual resistance is plotted as a function of gate bias (b) when the TFT is operating with PANI-PAAMPSA-coated gold as the source electrode and gold as the drain electrode; (c) with gold as the source electrode and PANI-PAAMPSA-coated gold as the drain electrode. For both configurations, the contact resistance at the channel/gold interface is more than five-fold higher than that at the channel/PANI-PAAMPSA interface at most gate biases.

REFERENCES

1. I. Kymissis, C. D. Dimitrakopoulos, S. Purushothaman, *IEEE Transactions on Electron Devices* **2001**, *48*, 1060.

2. M. Lefenfeld, G. Blanchet, J. A. Rogers, *Advanced Materials* **2003**, *15*, 1188.

3. H. Sirringhaus, T. Kawase, R. H. Friend, T. Shimoda, M. Inbasekaran, W. Wu, E. P. Woo, *Science* **2000**, *290*, 2123.

4. G. B. Blanchet, C. R. Fincher, M. Lefenfeld, J. A. Rogers, *Applied Physics Letters* **2004**, *84*, 296.

5. K. S. Lee, G. B. Blanchet, F. Gao, Y.-L. Loo, *Applied Physics Letters* **2005**, *86*, 074102.

6. J. E. Yoo, J. L. Cross, T. L. Bucholz, K. S. Lee, M. P. Espe, Y.-L. Loo, *Journal of Materials Chemistry* **2007**, *17*, 1268.

7. K. S. Lee, T. J. Smith, K. C. Dickey, J. E. Yoo, K. J. Stevenson, Y.-L. Loo, *Advanced Functional Materials* **2006**, *16*, 2409.

8. P. V. Necliudov, M. S. Shur, D. J. Gundlach, T. N. Jackson, *Solid-State Electronics* **2002**, *47*, 259.

9. F. J. Meyer zu Heringdorf, M. C. Reuter, R. M. Tromp, *Applied Physics A: Materials Science & Processing* **2004**, *78*, 787.

10. C. D. Dimitrakopoulos, P. R. L. Malenfant, *Advanced Materials* **2002**, *14*, 99.

11. J. Stohr, *NEXAFS Spectroscopy*, Springer, Berlin **1992**.

12. D. M. DeLongchamp, E. K. Lin, D. A. Fischer, *Proceedings of SPIE-The International Society for Optical Engineering* **2005**, *5940*, 54.

13. D. A. Krapchetov, H. Ma, A. K. Y. Jen, D. A. Fischer, Y.-L. Loo, *Langmuir* **2005**, *21*, 5887.

14. W. S. Hu, Y. T. Tao, Y. J. Hsu, D. H. Wei, Y. S. Wu, *Langmuir* **2005**, *21*, 2260.

15. H. Sirringhaus, P. J. Brown, R. H. Friend, M. M. Nielsen, K. Bechgaard, B. M. W. Langeveld-Voss, A. J. H. Spiering, R. A. J. Janssen, E. W. Meijer, P. Herwig, D. M. De Leeuw, *Nature (London)* **1999**, *401*, 685.

16. M. Nonnenmacher, M. P. O'Boyle, H. K. Wickramasinghe, *Applied Physics Letters* **1991**, *58*, 2921.

17. R. A. Street, A. Salleo, *Applied Physics Letters* **2002**, *81*, 2887.

18. H. Klauk, G. Schmid, W. Radlik, W. Weber, L. Zhou, C. D. Sheraw, J. A. Nichols, T. N. Jackson, *Solid-State Electronics* **2002**, *47*, 297.

19. D. M. DeLongchamp, S. Sambasivan, D. A. Fischer, E. K. Lin, P. Chang, A. R. Murphy, J. M. J. Frechet, V. Subramanian, *Advanced Materials* **2005**, *17*, 2340.

20. L. Burgi, H. Sirringhaus, R. H. Friend, *Applied Physics Letters* **2002**, *80*, 2913.

21. K. P. Puntambekar, P. V. Pesavento, C. D. Frisbie, *Applied Physics Letters* **2003**, *83*, 5539.

Chapter 5: Improving the electrical conductivity of polyaniline

Our characterization of pentacene thin-film transistors (TFTs) with polyaniline (PANI-PAAMPSA) electrodes in the previous chapter reveals reduced contact resistance at the pentacene/PANI-PAAMPSA interface during device operation. We observe, however, non-negligible bulk resistance associated with PANI-PAAMPSA electrodes that limit current outputs from the device. While the use of an underlying gold layer can effectively suppress the bulk resistance of PANI-PAAMPSA (Chapter 4), this is only a means for us to decouple the bulk resistance so we can effectively quantify the contact resistance of PANI-PAAMPSA. The use of underlying gold electrodes would not be practical from an application standpoint. Our ultimate goal is thus to improve the conductivity of PANI-PAAMPSA so the material is no longer bulk resistance limited when incorporated in organic devices. As described in Chapter 1, the conductivity of PANI that is doped with small-molecule acids, such as camphor sulfonic acid (CSA), has shown to increase when exposed to or immersed in an "appropriate" solvent.[1, 2] For example, PANI-CSA films cast from chloroform exhibits a conductivity of 0.2S/cm. If this PANI-CSA film is immersed in or exposed to m-cresol (or other phenols), its conductivity can be as high as 300S/cm.[1, 2] This phenomenon is called "secondary doping" where the conductivity improvement originates from a change in the PANI-CSA chain conformation.[1, 2] Specifically, PANI-CSA adopts a "compact coil" chain conformation when dissolved in a poor solvent, such as chloroform. When PANI-CSA is dissolved in a good solvent, like m-cresol, the chain conformation of PANI-CSA can be rearranged from the "compact coil" to the "extend chain" conformation. The extended chain conformation increases charge delocalization along the PANI backbone, thereby enabling more efficient charge transport.

In the literature, there has not been any example of secondary doping of PANI doped with polymer acids. Our experience also indicates that treating PANI-PAAMPSA with m-cresol does not improve its conductivity. While secondary doping with a fluorinated alcohol also increases the conductivity of PANI-CSA,[3-5] fluorinated alcohols do not alter the conductivity of PANI-PAAMPSA.[6] This indicates that secondary doping of PANI is specific with respect to its dopant and implicates further complications with secondary doping of PANI that is doped with polymer acids.

We recently improved the conductivity of PANI-PAAMPSA by more than two orders of magnitude by treating it with dichloroacetic acid (DCA). DCA has been reported to be a good solvent for PANI-CSA[4] and PANI doped with 2-acrylamido-2-methyl-1-propane sulfonic acid (AMPSA[7-9]; the monomer of PAAMPSA). The role of DCA in such processes, however, has not been described. In this chapter, we present the first detailed structural characterization of untreated and DCA-treated PANI-PAAMPSA to elucidate the origin of conductivity improvement by DCA treatment.

To assess the effect of the improved conductivity, we incorporated DCA-treated PANI-PAAMPSA electrodes into organic TFTs that utilize vapor- as well as solution-processable organic semiconductors. Our results indicate that the performance of organic TFTs, such as mobilities and on/off current ratios, can be improved by more than an order of magnitude when the bulk resistance of PANI-PAAMPSA electrodes is reduced through DCA treatment.

DCA TREATMENT

We prepared PANI-PAAMPSA films on Si/SiO$_2$ substrates from a 5wt% aqueous dispersion. The PANI-PAAMPSA films were baked at 90°C for 3 minutes to remove residual water, and were subsequently immersed in pre-heated DCA (Acros Organics, 99+%) at 80°C for 10 minutes. After immersing in DCA, the substrates were baked at 90-100°C for 10-15 minutes to remove residual DCA. The electrical conductivities of DCA-treated PANI-PAAMPSA films were then measured using the four-point probe technique previously described in Chapter 3. We also measured the conductivities of PANI-PAAMPSA films prior to DCA treatment for reference. Figures 5.1a and b show representative current-voltage (I-V) characteristics of untreated and DCA-treated PANI-PAAMPSA films, respectively. The currents are on the order of 10μA when a voltage of 10V is applied on the PANI-PAAMPSA thin film. After DCA treatment, the current levels increase by more than two orders of magnitude (Figure 5.1b), given the same applied voltage (Figure 5.1a). Normalizing the slopes by the lengths and the cross-sectional areas of the films reveals an average conductivity of 72.9±44.6S/cm for DCA-treated PANI-PAAMPSA films and an average conductivity of 0.16±0.11S/cm for the untreated films.

We characterized the morphologies of PANI-PAAMPSA films before and after DCA treatment using scanning electron microscopy (SEM), as shown in Figure 5.2a and b, respectively. Figure 5.2a reveals a rough globular morphology in the PANI-PAAMPSA film. We observed a drastically different morphology after DCA treatment. Figure 5.2b is featureless except for the deep scratch we created so we could focus on the surface during imaging. Consistent with SEM images, atomic force microscopy (AFM) reveal the rough surface of PANI-PAAMPSA, with aggregates ranging 100 to 200nm in size. The root mean square (r.m.s) roughness of PANI-PAAMPSA is 29.5nm in the 5×5μm window shown in Figure 5.2c. In contrast, the r.m.s roughness of the treated PANI-PAAMPSA film is 7.85nm, as shown in Figure 5.2d.

To reveal the details of the electronic structures of the two films, we carried out ultraviolet-visible-near-infra-red spectroscopy (UV-Vis-NIR) experiments on PANI-PAAMPSA and DCA-treated PANI-PAAMPSA. Figure 5.3a (i) shows the UV-Vis-NIR spectrum of untreated PANI-PAAMPSA. It has two distinct absorption bands. The broad absorption ranging from 300 to 450nm is associated with a transition from the π band to the π^* band.[10] The other narrow absorption at around 760nm is attributed to a transition from the π band to a narrow polaron band.[10] This optical spectrum is consistent with previously-reported spectra of PANI having low conductivities (0.01-0.1S/cm), and is interpreted as PANI having a compact coil conformation.[1, 2, 10] Figure 5.3a (ii) reveals the UV-Vis-NIR spectrum of DCA-treated PANI-PAAMPSA, which is drastically different from that of untreated PANI-PAAMPSA. Specifically, the narrow absorption at 760nm disappears, and a broad absorption appears between 1000 and 2000nm. This broad absorption is often referred to as the "free charge carrier tail,"[1, 2, 10] and corresponds to the transition from a broad polaron band to the π^* band stemming from an extended chain conformation.[10] The presence of this board absorption in the near-IR region suggests that the chain conformation of PANI-PAAMPSA has changed from a compact coil conformation to an extended chain conformation upon DCA exposure. As mentioned earlier, such extended chain conformation improves charge transport.[1, 2, 10] As a consequence, DCA-treated PANI-PAAMPSA exhibits conductivities on the order of 100S/cm.

To elucidate the nature of charge transport in untreated and DCA-treated PANI-PAAMPSA, we conducted variable temperature conductivity measurements on the two samples. These conductivity measurements were conducted in collaboration with Suyong Jung in Professor Zhen Yao's group in the Physics Department. The PANI-PAAMPSA thin films were placed in a cryostat and their conductivities measured as a function of temperature from 81 to 298K.

Figure 5.3b (i) shows the temperature-dependent conductivity of untreated PANI-PAAMPSA. We carried out two-point probe measurements on untreated PANI-PAAMPSA because its conductivity at low temperatures was too low to be analyzed by the four-point probe setup. Since the bulk resistance of PANI-PAAMPSA is so high, we assumed that the contact resistance between the probes and the sample is negligible and calculated its conductivity based on the dimensions of the setup given the output currents. Below 130K, the bulk resistance of PANI-PAAMPSA exceeds the instrumental limitation so we were not able acquire data beyond this point. The conductivity of PANI-PAAMPSA decreased from 10^{-2}S/cm at room temperature to 10^{-6}S/cm at 130K. This phenomenon indicates that PANI-PAAMPSA becomes more like a semiconductor than a metal (conductivity should increase with decreasing temperature due to reduced electron scattering at low temperatures). The conductivity data can be described by an Arrhenius fit, suggesting that charge transport in PANI-PAAMPSA is enabled by a thermally activated hopping process.[11-14] Figure 5.3b (ii) reveals the conductivity of DCA-treated PANI-PAAMPSA. These measurements were made with a four-point probe. Similar to that of PANI-PAAMPSA film, the conductivity decreases as the temperature is decreased, suggesting that charge transport is also enabled by a thermally-activated hopping process in DCA-treated PANI-PAAMPSA.[11-14] We were able to fit the conductivity-temperature curves with the quasi one-dimensional variable hopping model[11-14] shown in Equation 5.1.

$$\sigma(T) = \sigma_o \exp\left[-\left(\frac{T_o}{T}\right)^{1/2}\right] \qquad (5.1)$$

where σ is the conductivity; σ_o is a constant; T is the temperature; T_o is the slope of the conductivity-temperature curve shown in Figure 5.3, which can be thought of as an activation energy for charge hopping.[11-14] Fitting the data to Equation 5.1 reveals T_o = 1690K for DCA-treated PANI-PAAMPSA and T_o = 19980K for PANI-PAAMPSA. That T_o is an order of magnitude smaller for DCA-treated PANI-PAAMPSA compared to untreated PANI-PAAMPSA indicates that charge hopping is much more effective in DCA-treated PANI-PAAMPSA compared that in untreated PANI-PAAMPSA.

As a first step towards to elucidating the origin of conductivity improvement by DCA treatment, we conducted comparative experiments by treating PANI-PAAMPSA with other solvents, such as trichloroacetic acid (TCA) and dimethyl sulfoxide (DMSO). TCA is interesting because it has a similar chemical structure to DCA, except that it contains one more chlorine atom. TCA thus has a slightly low acidity (pK_a=0.77) compared to that of DCA (pK_a=1.25).[15] DMSO was chosen because its sulfonyl groups are not acidic (pK_a=35) so the use of DMSO can possibly provide information about how the acidity of solvents affects conductivity improvement.[15] Table 5.1 summarizes the conductivities of PANI-PAAMPSA films treated with DCA, TCA, and DMSO. While similar conductivity improvement was observed in DCA-treated and TCA-treated PANI-PAAMPSA, little improvement was observed in DMSO-treated PANI-PAAMPSA. These results suggest that the acidity of the solvent plays an important role in improving the conductivity of PANI-PAAMPSA.

Table 5.1 - Summary of conductivities of PANI-PAAMPSA treated with various solvents and the acidities of the solvents.

	Conductivity (S/cm)	**Solvent acidity (pK_a)**
Untreated PANI-PAAMPSA	0.16±0.10	
DCA-treated PANI-PAAMPSA	72±43	1.3
TCA-treated PANI-PAAMPSA	64±34	0.77
DMSO-treated PANI-PAAMPSA	0.20±0.01	35

To identify whether the DCA treatment induces any chemical changes in PANI-PAAMPSA, we conducted transmission Fourier-Transform Infrared spectroscopy (FTIR) on PANI-PAAMPSA as well as on DCA-treated PANI-PAAMPSA. We spun-cast PANI-PAAMPSA on test Si wafers (1-10Ωcm, transparent to IR) before treating with the solvents. PAAMPSA powder dispersed in KBr was also examined as a reference. Figure 5.4 contains the powder FTIR spectrum of PAAMPSA in KBr (a). The other spectra are FT-IR spectra of spun-cast films including PANI-PAAMPSA (b), DCA-treated PANI-PAAMPSA (c), TCA-treated PANI-PAAMPSA (d), and DMSO-treated PANI-PAAMPSA (e). Figure 5.4a shows the spectrum of PAAMPSA with a broad peak at $3328cm^{-1}$ (labeled 1 in Figure 5.4). This broad peak at $3328cm^{-1}$ is attributed to N-H stretching of the amide groups.[16] Figure 5.4b reveals the spectrum of PANI-PAAMPSA in which peak (1) is suppressed. Rather, we observe a broad peak located at 3238 cm^{-1} (labeled 2 in Figure 5.4). Previous reports have indicated that this broad peak at 3238cm^{-1} is associated with hydrogen-bonded N-H stretching of the PANI backbone.[17-20] The peaks labeled as (3) through (7) from 1572 to 1144cm^{-1} are associated with C-C and C-N stretching of the PANI backbone.[17-20] The identification of these peaks is difficult because they overlap extensively with peaks associated with PAAMPSA, such as S-O stretching at 1220cm^{-1} and C-N stretching at 1550cm^{-1} (see Figure 5.4a).[21, 22] While the spectrum of DCA-treated PANI-PAAMPSA (Figure 5.4c) exhibits peaks (3-7), peak (2) is significantly suppressed. A similar spectrum is observed for TCA-treated PANI-PAAMPSA, as shown in Figure 5.4d. These observations indicate that exposure to DCA and TCA induces similar chemical changes in PANI-PAAMPSA. Figure 5.4e shows the spectrum of DMSO-treated PANI-PAAMPSA. This spectrum is similar to that of PANI-PAAMPSA. This observation indicates that exposure to DMSO does not induce any significant structural changes, and is consistent with the negligible conductivity improvement we observe after DMSO treatment (Table 5.1). The presence of peak (2) in the spectra of PANI-PAAMPSA and DMSO-treated PANI-PAAMPSA suggests significant hydrogen bonding in these two samples.[17-20] DCA or TCA treatment appears to suppress such hydrogen bonding as peak (2) is suppressed in those spectra.

To further examine the chemical changes in PANI-PAAMPSA after DCA treatment, we conducted X-ray photoemission spectroscopy (XPS) experiments on untreated and DCA-treated PANI-PAAMPSA films. XPS spectra were collected at a take-off angle of 75° to increase the depth sensitivity of the films. Figures 5.5a and b contain the XPS nitrogen spectra of untreated and DCA-treated PANI-PAAMPSA, respectively. The nitrogen spectra were deconvoluted into three Gaussian peaks centered at 399.2eV (NH, nitrogen in amines), 400.4eV (N^{1+}, protonated nitrogen), and 401.3eV (N^{2+}, protonated nitrogen). A full width half maximum intensity (FWHM) of 1.4eV is maintained for all three peaks.[20, 23, 24] Figures 5.5c and d show the XPS sulfur spectra of PANI-PAAMPSA and DCA-treated PANI-PAAMPSA, respectively. The sulfur spectra were deconvoluted into two doublets. Each doublet was fitted with two sinlgets, i.e., $S2p_{3/2}$ and $S2p_{1/2}$. One doublet was fitted with two singlets, $S2p_{3/2}$ and $S2p_{1/2}$ that are centered at 167.5 and 168.7eV, respectively (ionized PAAMPSA, $SO_3^-N^+$) and the other doublet with $S2p_{3/2}$ and $S2p_{1/2}$ that are centered at 168.3 and 169.5eV, respectively (neutral PAAMPSA, SO_3H).[12, 25, 26] All four singlet peaks maintain a FWHM of 1.0eV. We detected no measurable amounts of chlorine in DCA-treated PANI-PAAMPSA, suggesting that DCA was completely removed on heating at 80°C

Table 5.2 - Summary of the relative concentration of nitrogen and sulfur atoms in different environments to total sulfurs.

	NH/S (399.2eV)	**N^{1+}/S (400.4eV)**	**N^{2+}/S (401.3eV)**	**SO_3H/S (168.3eV)**	**$SO_3^-N^+$/S (167.5eV)**
PANI-PAAMPSA	**1.08**	**0.10**	**0.73**	**0.21**	**0.79**
DCA-treated PANI-PAAMPSA	**1.25**	**0.30**	**0.23**	**0.35**	**0.65**

To quantify the changes in the concentration of nitrogen and sulfur atoms in neutral and ionic environments, we first assumed that the concentration of total sulfur atoms in the system (only PAAMPSA contains sulfur) remains constant before and after DCA treatment since PAAMPSA is not volatile. We further assumed that the nitrogen in PAAMPSA is neutral.[24] The peak associated with these neutral nitrogen atoms is difficult to decoupled from any neutral nitrogens in PANI because they overlap.[24] We integrated intensities of neutral amine nitrogens of PANI-PAAMPSA, (NH, 399.2eV), that of protonated nitrogens (N^{1+}, 400.4eV and N^{2+}, 401.3eV) in PANI, that of the neutral sulfurs in PAAMPSA (SO_3H, $S2p_{3/2}$ at 168.3eV), and that of sulfurs in ionized sulfonic acid ($SO_3^-N^+$, $S2p_{3/2}$ at 167.5eV) in PAAMPSA. These integrated intensities are normalized by the total concentration of sulfur atoms (S) and are summarized in Table 5.2.

According to a previous report[23], we identify N^{1+} that is associated with delocalized polarons and bipolarons that enable charge transport through PANI-PAAMPSA.[23] N^{2+} is identified as the positively charged amines that are more tightly bound to the ionized sulfonic groups in PAAMPSA compared to N^{1+}.[23] Before treating PANI-PAAMPSA with DCA, we found NH/S, N^{1+}/S, and N^{2+}/S to be 1.08 and 0.10, and 0.73, respectively. These observations indicate that a large portion of protonated nitrogens is strongly associated with negatively charged sulfonic acids groups in PAAMPSA. Consistent with these observations, we observe a large portion of sulfonic acid that is ionized, 0.79 of $SO_3^-N^+$/S as opposed to 0.21 of SO_3H/S. A low portion of N^{1+}/S that is relevant to charge transport is in agreement with a low electrical conductivity of PANI-PAAMPSA prior to DCA treatment.

After DCA treatment, NH/S and N_1^+/S, (401.3eV) increased from 1.08 to 1.25 and 0.10 to 0.30, respectively. N_2^+/S decreased from 0.73 to 0.23. Simultaneously, the relative concentration of ionized sulfonic acid, $SO_3^-N^+$/S is also decreased from 0.79 to 0.65. These observations suggest that the strong ionic associations between PANI and PAAMPSA, i.e., N_2^+/S and $SO_3^-N^+$/S are reduced with DCA treatment. As such, DCA "moderates" the ionic interactions between PANI and PAAMPSA, thereby allowing structural rearrangement of PANI-PAAMPSA. Specifically, PANI-PAAMPSA adopts an "extended chain" structure (as opposed to a "compact coil") after DCA treatment. Such DCA-treated PANI-PAAMPSA having the "extended chain" structure exhibits higher conductivities.

In addition to conductivity improvement, exposure to DCA induces macroscopic changes in morphology of PANI-PAAMPSA films, as shown in Figure 5.2.[27] An earlier study by Sun and Yang speculated that the morphology of polymer acid template-synthesized PANI can be determined by the degree of interaction between protonated aniliniums and polymer acid anions during synthesis.[27] For example, when aniline is polymerized in the presence of poly(styrene sulfonic acid), which has a high degree of ionization, protonated aniliniums are tightly bound to the polymer anions due to strong ionic interactions. After polymerization, tight aniline-polymer interactions maintain, so the resulting PANI-poly(styrene sulfonic acid) adopts a globular morphology that reflects the random coil conformation of poly(styrene sulfonic acid).[27] In contrast, Sun and Yang observed an extended fibrous morphology of PANI when it is synthesized with poly(acrylic acid) where aniliniums are weakly bound to poly(acrylic acid) anions due to the relatively low degree of ionization of -COOH groups, relative to that of $-SO_3H$

groups.[27] We thus speculate that the rough globular morphology of PANI-PAAMPSA stems from the strong ionic interactions between PANI and PAAMPSA (Figure 5.2a and c). Exposure to DCA moderates the ionic interactions between PANI and PAAMPSA, the rough globular morphology of PANI-PAAMPSA thus becomes featureless after DCA treatment (Figure 5.2b and d).

We have shown that the conductivity of PANI-PAAMPSA is improved by more than two orders of magnitude by a simple DCA treatment post processing. The conductivity improvement is accompanied by drastic changes in the molecular structures of PANI-PAAMPSA after DCA treatment. Investigating the interactions between PANI and PAAMPSA shed light on understand the origin of the structural changes. Specifically, we identify the presence of strong ionic interactions between PANI and PAAMPSA to lead to a compact coil conformation of PANI-PAAMPSA. DCA, having a sufficiently low acidity, effectively interrupts the ionic interactions between PANI and PAAMPSA. Due to moderated ionic interactions, PANI-PAAMPSA can rearrange its conformation from the “compact coil” to the “extended chain”. In the extended chain conformation, delocalized polarons and bipolarons that enable more efficient charge transport are increased, thereby improving the conductivity of PANI-PAAMPSA.

ORGANIC THIN-FILM TRANSISTORS WITH DCA-TREATED PANI-PAAMPSA ELECTRODES

To investigate how the enhanced conductivity of DCA-treated PANI-PAAMPSA affects the performance of organic TFTs, we fabricated bottom-contact pentacene and dihexylthiophene anthracene (DHT-ANT) TFTs with DCA-treated PANI-PAAMPSA electrodes. DHT-ANT is an alternative to pentacene because of its high mobility and long-term air-stability.[28] Its chemical structure was shown in Figure 2.1b. This molecule is provided by Dr. Hong Meng at DuPont Research and Development, Wilmington, DE. Meng and coworkers recently demonstrated top-contact DHT-ANT TFTs with gold electrodes that exhibit mobilities ranging from 0.1-0.5cm^2/V-s and air stability over 15 months.[28]

We first defined a series of PANI-PAAMPSA electrodes on Si/SiO$_2$ substrates (SiO$_2$ thickness ≅90nm). Specifically, the molecular template was created by the subtractive patterning scheme outlined in Figure 3.1b on vapor-deposited HMDS substrates. A series of PANI-PAAMPSA electrodes were then created by drop-casting from its aqueous dispersion. Representative electrodes were shown in Figure 3.5b. These electrodes define a channel length (L) of ≅100μm and a channel width (W) of ≅1000μm. These electrodes were subsequently treated in DCA to improve the polymer electrode conductivity per earlier discussion. To complete the TFTs, either pentacene or DHT-ANT was thermally evaporated on the electrodes. Each TFT was isolated by mechanically scratching the organic semiconductor film in the surroundings of each electrode pair. We also fabricated reference bottom-contact TFTs with untreated PANI-PAAMPSA electrodes having the same device dimensions in the same batch.

To operate these devices, we applied a source-drain voltage between 0 and -20V. The gate voltage was increased from 5 to -20V in steps of -5V. Figure 5.6 contains representative I-V characteristics of a pentacene TFT with untreated PANI-PAAMPSA. The I-V characteristics in Figure 5.6a exhibits clean output current modulation as the gate voltage is increased from 5 to -10V. The output current modulation, however, appears to be stagnant in the saturation regime at gate voltages greater than -15V. To a lesser degree, we witnessed this phenomenon in the output characteristics of the pentacene TFT with PANI-PAAMPSA electrodes in Figure 3.4b. This effect is more obvious in the transfer characteristics shown in Figure 5.6b. In the transfer characteristics, the square root of source-drain current at a source-drain voltage of -20V is plotted as a function of gate voltage (saturation regime). At gate voltages greater than -10V, the square root of source-drain current starts to roll off and is no longer consistent with that estimated from Equation 2.2 in which the square root of source-drain current increases linearly as a function of the gate voltage. As a result, we estimate the mobility (0.17cm^2/V-s) using only two points at -5 and -10V. The roll of in the transfer characteristics is attributed to the high bulk resistance of PANI-PAAMPSA electrodes. As shown in Chapter 4, a non-negligible potential drop can be comparable to the channel resistance as the gate voltage is increased. The source-drain voltage and the gate voltage are thus singinficanly reduced. As a result, the output current is no longer modulated by Equation 2.2 and it is stagnant regardless of increasing the gate voltage.

In contrast, such phenomenon is absent in pentacene TFTs with DCA-treated PANI-PAAMPSA electrodes. Figure 5.6c reveals representative I-V characteristics of one such device exhibiting effective current modulation beyond gate voltages of -10V. Figure 5.6d shows the transfer characteristics of the same device. In the transfer characteristics, the square root of source-drain current effectively increases at the gate voltages greater than -10V, a sign that the output currents are not limited by the bulk resistance of DCA-treated PANI-PAAMPSA electrodes. We were thus able to extrapolate a slope using data points spanning the entire range of gate voltages after the device turns on. This slope yields a mobility of 0.19cm^2/V-s.

Figure 5.7a shows representative I-V characteristics of a DHT-ANT TFTs with untreated PANI-PAAMPSA electrode. This TFT exhibits significantly suppressed output currents and suffers from serious current hysteresis. The transfer characteristics also exhibit low source-drain currents with a roll-off at gate voltages higher than -5V, as shown in Figure 5.7b. Figure 5.7c reveals drastically the enhanced I-V characteristics of a DHT-ANT TFT with DCA-treated PANI-PAAMPSA electrodes. The output currents increase by more than an order of magnitude, relative to those of devices with PANI-PAAMPSA electrodes. Figure 5.7d shows that the transfer characteristics of the same device, in which the source-drain current is effectively modulated as a function of the gate voltage without any roll-off. The details of device performance of pentacene and DHT-ANT TFTs with non-treated as well as DCA-treated PANI-PAAMPSA electrodes are summarized in Table 5.3.

Table 5.3 - Summary of device characteristics of bottom-contact pentacene and DHT-ANT TFTs with untreated PANI-PAAMPSA electrodes and DCA-treated PANI-PAAMPSA electrodes having the same channel dimensions ($L \cong 100\mu\text{m}$ and $W \cong 1000\mu\text{m}$).

Channel/Electrodes	**Mobility (cm^2/Vs)**	**On/off Current Ratio**	**Threshold voltage (V)**
Pentacene/untreated PANI-PAAMPSA	0.16±0.02	10^4	-0.2±0.4
Pentacene/DCA-treated PANI-PAAMPSA	0.16±0.04	10^5	0.6±1.4
DHT-ANT/untreated PANI-PAAMPSA	0.007±0.003	10^3	3.5±2.6
DHT-ANT/DCA-treated PANI-PAAMPSA	0.07±0.02	10^5	2.7±1.8

While the average mobilities appear to be statistically identical between pentacene TFTs with PANI-PAAMPSA and those with DCA-treated PANI-PAAMPSA electrodes, we observe that the on/off current ratio increased by one order of magnitude due to an increase in the on-currents at higher gate voltages from the TFTs with DCA-treated PANI-PAAMSPA. Similar values of threshold voltage indicate that DCA does not affect the surface polarity of the dielectric surface significantly.[29] A ten-fold increase in the average mobility is observed with DHT-ANT TFTs with DCA-treated PANI-PAAMPSA electrodes, relative to that of TFTs with untreated electrodes. The on/off current ratio increased from 10^3 to 10^5. Again, the threshold voltage remained the same after DCA treatment. While the mobility of pentacene devices appears to be similar whether using PANI-PAAMPSA electrodes or DCA-treated PANI-PAAMPSA electrodes in pentacene devices, we observe an order of magnitude increase in the mobility of DHT-ANT devices using DCA-treated PANI-PAAMPSA electrodes. We speculate this disparity stems from a difference in energy barriers between the pentacene/PANI-PAAMPSA and the DHT-ANT/PANI-PAAMPSA interfaces.

To complement device characterization, we conducted AFM experiments to further examine the topography of pentacene and DHT-ANT in the channel regions of both TFTs. Figures 5.8a and b reveal the morphologies of the organic semiconductor in the channel regions of pentacene TFTs with untreated PANI-PAAMPSA and of those with DCA-treated PANI-PAAMPSA electrodes, respectively. The pentacene morphologies appear to be largely similar in the channels regardless of PANI-PAAMPSA electrode treatment. Similarly, Figures 5.8c and d reveal similar DHT-ANT morphologies in the channel regions of TFTs with untreated and with DCA-treated PANI-PAAMPSA electrodes, respectively. These observations indicate that treating PANI-PAAMPSA with DCA after the channel has been defined does not significantly affect the surface properties of HMDS-treated SiO_2 on which pentacene or DHT-ANT is subsequently deposited.

We also took SEM images of pentacene and DHT-ANT TFTs at the channel/electrodes interfaces. Figure 5.9a shows the morphology of pentacene at the channel/PANI-PAAMPSA interface. In Figure 5.9a, we observe small pentacene grains that conform to the surface of PANI-PAAMPSA. Figure 5.9b shows pentacene at the interface between the channel and DCA-treated PANI-PAAMPSA. A much smoother pentacene morphology is observed on DCA-treated PANI-PAAMPSA. Since pentacene tends to adhere to the surface of PANI-PAAMPSA, the smoother DCA-treated PANI-PAAMPSA likely results in smooth pentacene. As expected, pentacene in the channel regions of both TFTs appears the same. Figure 5.9c reveals the morphology of DHT-ANT at the channel/PANI-PAAMPSA interface. Similar to pentacene on PANI-PAAMPSA, DHT-ANT adopts the high surface roughness of PANI-PAAMPSA. In contrast, Figure 5.9d reveals a smoother DHT-ANT morphology on DCA-treated PANI-PAAMPSA. The DHT-ANT grains in this TFT appear to be similar to those in the channel region.

ELECTRONIC BAND STRUCTURES OF PENTACENE/PANI-PAAMPSA VS. DHT-ANT/PANI-PAAMPSA INTERFACES

The performance of bottom-contact DHT-ANT TFTs can be enhanced by improving the bulk conductivity of PANI-PAAMPSA electrodes through DCA treatment. Unlike pentacene TFTs, DHT-ANT TFTs exhibit poor performance (μ_{sat}=0.007cm^2/V-s, as opposed to 0.16cm^2/V-s) when using untreated PANI-PAAMPSA electrodes. We did not find any distinct structural defects between pentacene/PANI-PAAMPSA and DHT-ANT/PANI-PAAMPSA interfaces (Figures 5.9a and c). Rather, DHT-ANT appears to conform to the surface morphology of PANI-PAAMPSA. As mentioned previously, we speculate that the disparity in device performance is likely to originate from an energy barrier difference[30, 31] for charge injection at these two interfaces.

To examine the details of the electronic band structures of both pentacene/PANI-PAAMPSA and DHT-ANT/PANI-PAAMPSA interfaces, we carried out UPS experiments with the help of Dr. Chris Zangmeister at the National Institute of Standards and Technologies (NIST), in Gaithersburg, MD. With the UPS spectra collected, we obtained the work functions, the highest occupied molecular orbital (HOMO) levels, and the interfacial dipoles at the interfaces of interest, as previously described in Chapter 2.

The HOMO level can be interpreted as the energy barrier for charge injection through the electrode/semiconductor interface since it is defined as the energy difference between the ionization energy of the organic semiconductor and the work function of the electrode.[32] A large HOMO level thus suggests that charge transfer is difficult from the electrode to the organic semiconductor.[30, 31] Figure 5.10a illustrates the vacuum level alignment of the organic semiconductor and the electrode when the interfacial dipole is absent between the two materials. In such a case, the HOMO level (Φ_h) is simply estimated as the difference between the work function (Φ) of electrode surface and the ionization energy (IE): $\Phi_h = IE - \Phi$, as shown in Figure 5.10a. If an interfacial dipole (Δ) exists between the organic semiconductor and the electrode, the HOMO level becomes higher, i.e., $\Phi_h = IE - \Phi + \Delta$, as shown in Figure 5.10b. The presence of an interfacial dipole thus leads to a higher injection barrier between the organic semiconductor and the electrode. Figures 5.10c and d shows the electronic band structure of pentacene/PANI-PAAMPSA interface and that of DHT-ANT/PANI-PAAMPSA interface, respectively. The measured HOMO level of pentacene is 0.99eV. At the interface with PANI-PAAMPSA, pentacene exhibits an interfacial dipole of 0.54eV (Figure 5.11c). DHT-ANT exhibits a higher HOMO, i.e., 1.41eV, at the interface with PANI-PAAMPSA, as shown in Figure 5.10d. The larger HOMO level in DHT-ANT is attributed to a larger interfacial dipole at the DHT-ANT/PANI-PAAMPSA interface, i.e., 1.05eV as opposed 0.54eV at the pentacene/PANI-PAAMPSA interface. These observations indicate charge injection is much more difficult from PANI-PAAMPSA to DHT-ANT compared to that from PANI-PAAMPSA to pentacene. Such a large barrier hampers effective operation of DHT-ANT devices with PANI-PAAMPSA electrodes; their characteristics are never as high as those in similar devices with gold electrodes whether untreated or DCA-treated PANI-PAAMPSA electrodes are used. The presence of a large energy barrier can also be translated as a large contact resistance existing the channel/electrode interface.[31] Unlike pentacene devices, DHT-ANT devices with untreated PANI-PAAMPSA electrodes suffer from both the high bulk electrode resistance and large contact resistances. Highly conductive DCA-treated PANI-PAAMPSA is thus necessary to overcome contact resistances and effectively operate DHT-ANT devices.

There are several possible factors that can influence the formation and the magnitude of interfacial dipoles at organic semiconductor/electrode interfaces.[33] Such factors include charge transfer from the electrode to the organic semiconductor or vice-versa, rearrangement of electron cloud at the surface, chemical interactions at the interface, and orientation of polar molecules.[33] The origin of a large interfacial dipole at the DHT-ANT/PANI-PAAMPSA interface, however, is not well understood at this time and there thus needs future efforts to further examine such interface.

SOLUTION-PROCESSABLE ORGANIC SEMICONDUCTORS

We also incorporated DCA-treated PANI-PAAMPSA electrodes into TFTs that utilize solution-processable pentacene and anthradithiophene derivatives as active layers. Figures 5.11a and b show the chemical structures of triisopropylsilyl pentacene (TIPS-pentacene) and difluoro-triethylsilylethynyl anthradithiophene (FTES-ADT), respectively. These molecules are provided by Prof. John Anthony, in the Department of Chemistry at the University of Kentucky.[34] These molecules are particularly interesting because they can be easily processed from common organic solvents, such as toluene and chloroform.[34-37] The solution processability of these molecules stems from the bulky substituents on the center of the fused benzene rings. These substituents also promote inter-molecular π-stacking through which the molecules can form highly crystalline films.[38] Recently, Lee and coworkers demonstrated the growth of one-dimensional crystals of TIPS-pentacene by drop casting on tilted substrates.[39]

We recently found that one-dimensional ribbon-like FTES-ADT crystals can also be created through drop-casting on tilted substrates. More importantly, these one-dimensional crystals of FTES-ADT (and TIPS-pentacene) can form directly on Si/SiO_2 substrates with DCA-treated PANI-PAAMPSA electrodes. Figure 5.11c shows the scheme of drop-casting TIPS-pentacene or FTES-ADT solutions on tilted substrates. We began by preparing a series of PANI-PAAMPSA electrodes as well as DCA-treated PANI-PAAMPSA electrodes on Si/SiO_2 substrates. These electrodes define a channel dimension of $L \cong 100\mu m$ and $W \cong 1000\mu m$. To crystallize TIPS-pentacene or FTES-ADT, we drop-cast these molecules from 2wt% solution in toluene directly on tilted substrates that are pre-patterned with a series of DCA-treated PANI-PAAMPSA electrodes, as illustrated in Figure 5.11c. The solution droplet is pinned at an upper contact line while the rest of the drop flows along the substrate forming ribbon-like crystals oriented parallel to the flow direction as the solvent evaporates. Figures 5.12a and b reveal representative crystals of TIPS-pentacene and FTES-ADT in the channel regions and on DCA-treated PANI-PAAMPSA electrodes, respectively. These crystals have widths ranging from 50 to 300μm and lengths greater than 1mm. Most of these crystals thus span the entire channel length ($\cong$100μm).

Figure 5.13a shows representative I-V characteristics of a TIPS-pentacene TFT with untreated PANI-PAAMPSA electrodes. We apply source-drain voltages from 0 to -20V and systematically increase the gate voltages from 0 to -20V with steps of -5V. These TFTs yield low currents, on the order of $10^{-2}\mu A$, with serious current hysteresis, as shown in Figure 5.13a. Figure 5.13b shows representative I-V characteristics of a TIPS pentacene TFT with DCA-treated PANI-PAAMPSA electrodes. The TFT is operated by applying the source-drain voltages from 0 to -10V and the gate voltage from 0 to -10V in steps of -2V. Despite the reduced applied voltages, this device is yielding an order of magnitude higher output currents compared to the device with untreated PANI-PAAMPSA electrodes. Consequently, these TFTs exhibit mobilities and on/off ratios as high as 0.12 cm^2/V-s and 10^5, respectively. The device characteristics of TIPS-pentacene TFTs with untreated and DCA-treated PANI-PAAMPSA electrodes are summarized in Table 5.4.

Figure 5.13c shows representative I-V characteristics of an FTES-ADT TFT with untreated PANI-PAAMPSA electrodes. We again increased operating voltages with source-drain voltages from 0 to -20V and the gate voltages from 0 to -20V with steps of -5V. This device yield output currents on the order of 10^{-1}μA. Figure 5.13d shows representative I-V characteristics of an FTES-ADT TFT with DCA-treated PANI-PAAMPSA electrodes. Similar to TIPS-pentacene devices, this FTES-ADT TFT yields a current that is five-fold higher current than that from the TFT with untreated PANI-PAAMPSA electrodes at reduced operating voltages, as shown in Figure 5.13d. As a result, the mobilities of these devices is an approximately order of magnitude higher than those devices with untreated PANI-PAAMPSA electrodes, as summarized in Table 5.4.

Unlike DHT-ANT devices, however, we observe current crowding that persists in the small source-drain voltage regime at gate voltages greater than -8V in both TIPS-pentacene and FTES-ADT devices even when using DCA-treated PANI-PAAMPSA electrodes. This phenomenon suggests that charge injection may be much more difficult from PANI-PAAMPSA to TIPS-pentacene or FTES-ADT, compared to that to DHT-ANT. Payne and coworkers also observe similar current crowding in bottom-contact

TIPS-pentacene TFT with gold electrodes. They speculate that this phenomenon is attributed to an increase in the ionization energy (and thus HOMO level) of TIPS-pentacene compared to pentacene.[40] Specifically, the addition of triakylsilyl substituents increases the ionization of energies of functionalized acenes by >0.3eV compared to their parents acenes.[40] These higher ionization energies combined with the possibility of the formation of interface dipoles suggest large energy barriers between these molecules and PANI-PAAMPSA. It will thus be worthwhile to further identify the large energy barriers and elucidate their origins at interfaces between PANI-PAAMPSA and these molecules as future work.

Table 5.4 - Summary of device characteristics of bottom-contact TIPS-pentacene and FTES-ADT TFTs comparing untreated PANI-PAAMPSA electrodes with DCA-treated PANI-PAAMPSA electrodes having the same channel dimensions ($L \cong 100\mu m$ and $W \cong 1000\mu m$).

Channel/Electrodes	**Mobility (cm^2/Vs)**	**On/off Current Ratio**	**Threshold voltage (V)**
TIPS-pentacene/untreated PANI-PAAMPSA	0.002±0.001	10^3	0.5±0.3
TIPS-pentacene/DCA-treated PANI-PAAMPSA	0.07±0.04	10^5	0.2±0.4
FTES-ADT/untreated PANI-PAAMPSA	0.008±0.006	10^4	5.0±5.2
FTES-ADT/DCA-treated PANI-PAAMPSA	0.06±0.02	10^4	4.8±3.3

We have shown that the conductivity improvement of PANI-PAAMPSA is much more crucial when incorporated in TFTs that utilize functional acenes. Unlike pentacene, bottom-contact functional acene TFTs exhibit poor device characteristics when using untreated PANI-PAAMPSA electrodes. The poor device characteristics can be attributed to increased injection barrier between PANI-PAAMPSA and the functionalized acene. For example, we have identified a larger energy barrier between DHT-ANT and PANI-PAAMPSA compared to that between pentacene and PANI-PAAMPSA. The presence of a large energy barrier indicates the existence of a large contact resistance at the channel/electrode interface. To overcome a large contact resistance, highly conductive DCA-treated PANI-PAAMPSA has to be incorporated. Our results indicate that the use of DCA-treated PANI-PAAMPSA electrodes can improve the performance of organic thin-film transistors, such as mobilities and on/off current ratios, by more than an order of magnitude.

FIGURES

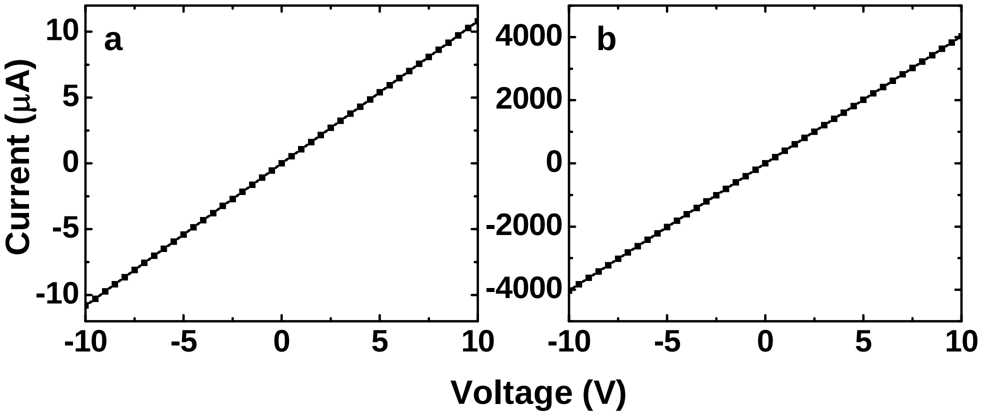

Figure 5.1. I-V characteristics of (a) PANI-PAAMPSA and (b) DCA-treated PANI-PAAMPSA.

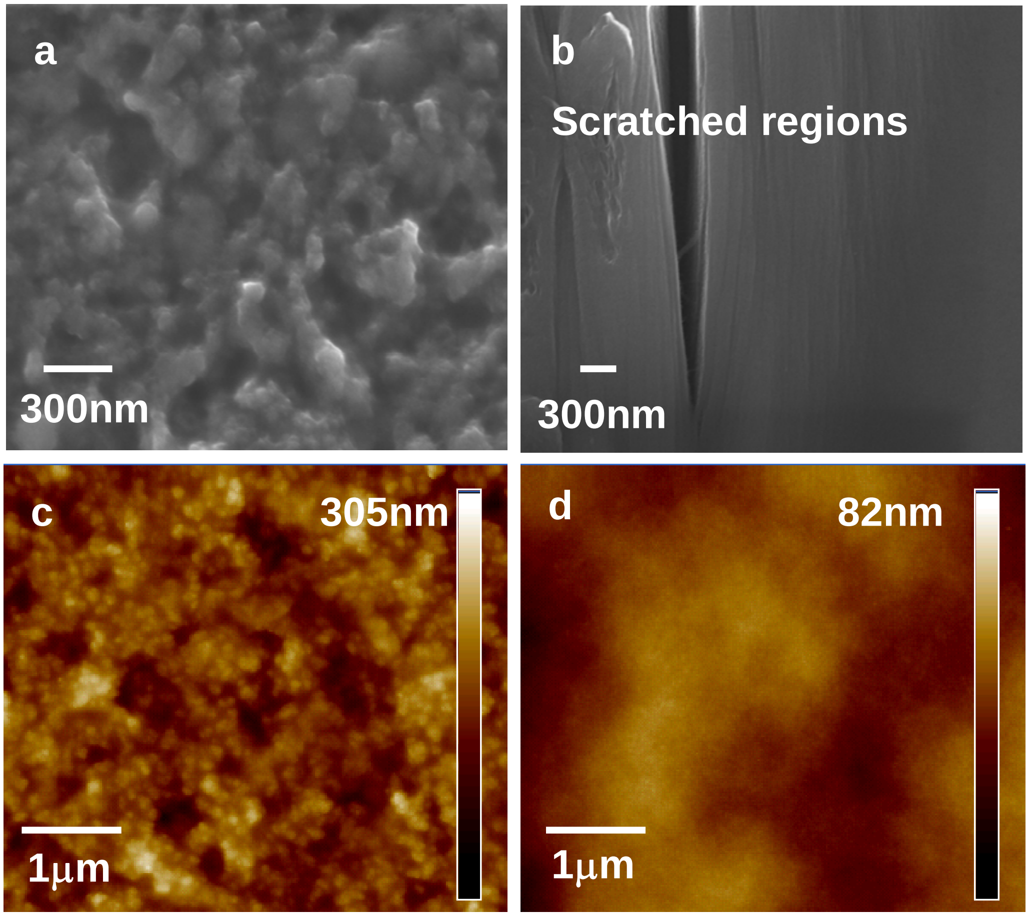

Figure 5.2. SEM images of (a) PANI-PAAMPSA and (b) DCA-treated PANI-PAAMPSA. AFM images of (c) PANI-PAAMPSA and (d) DCA-treated PANI-PAAMPSA.

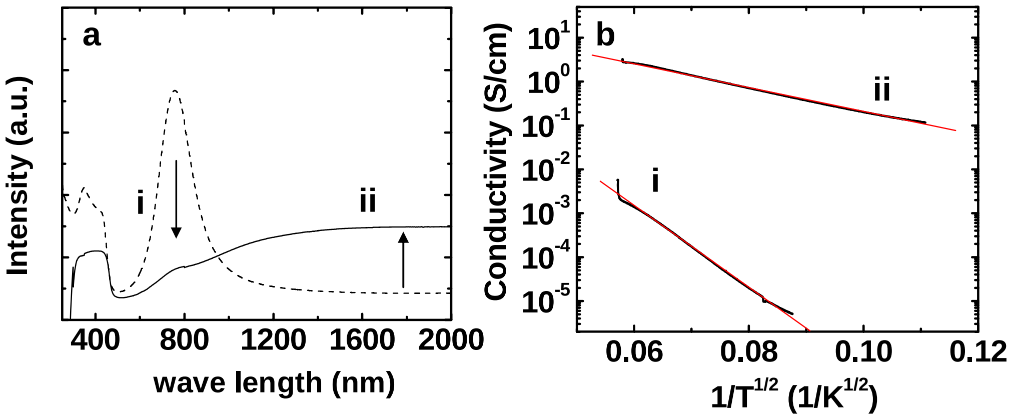

Figure 5.3. (a) UV-Vis-NIR spectra of (i) PANI-PAAMPSA and (ii) DCA-treated PANI-PAAMPSA films. (b) Temperature-dependent conductivities of (i) PANI-PAAMPSA and (ii) DCA-treated PANI-PAAMPSA films collected by the two-point probe and four-point probe measurement, respectively. We carried out two-point probe measurements on untreated PANI-PAAMPSA because its conductivity at low temperatures was too low to be analyzed by the four-point probe setup. Since the bulk resistance of PANI-PAAMPSA is so high, we assumed that the contact resistance between the probes and the sample is negligible and calculated its conductivity based on the dimensions of the setup given the output currents.

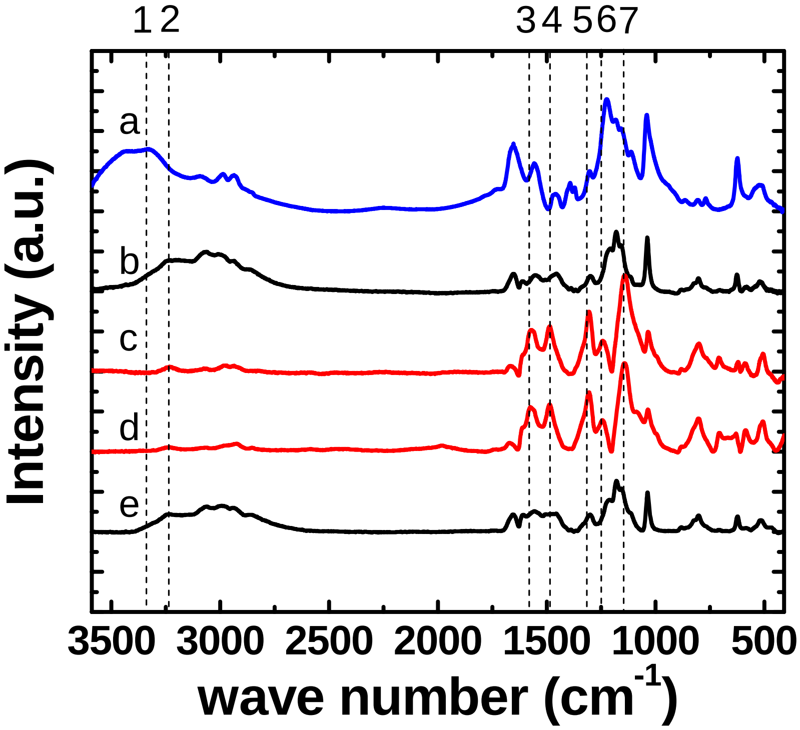

Figure 5.4. FT-IR spectra of (a) PAAMPSA (blue), (b) PANI-PAAMPSA (black), (c) DCA-treated PANI-PAAMPSA (red), (d) TCA-treated PANI-PAAMPSA (red), and (e) DMSO-treated PANI-PAAMPSA (black). The broad peak at 3328cm^{-1} (1) is attributed to N-H stretching of the amide groups.[16] The broad peak at 3238cm^{-1} (2) is associated with hydrogen-bonded N-H stretching of the PANI backbone.[17-20] The peaks labeled as (3) through (7) from 1572 to 1144cm^{-1} are associated with C-C and C-N stretching of the PANI backbone.[17-20] Identification of peaks (3-7) is difficult in (b) and (e) due to the overlap with the peaks associated with PAAMPSA, such as the S-O stretching at 1220cm^{-1} and C-N stretching at 1550cm^{-1}.[21, 22]

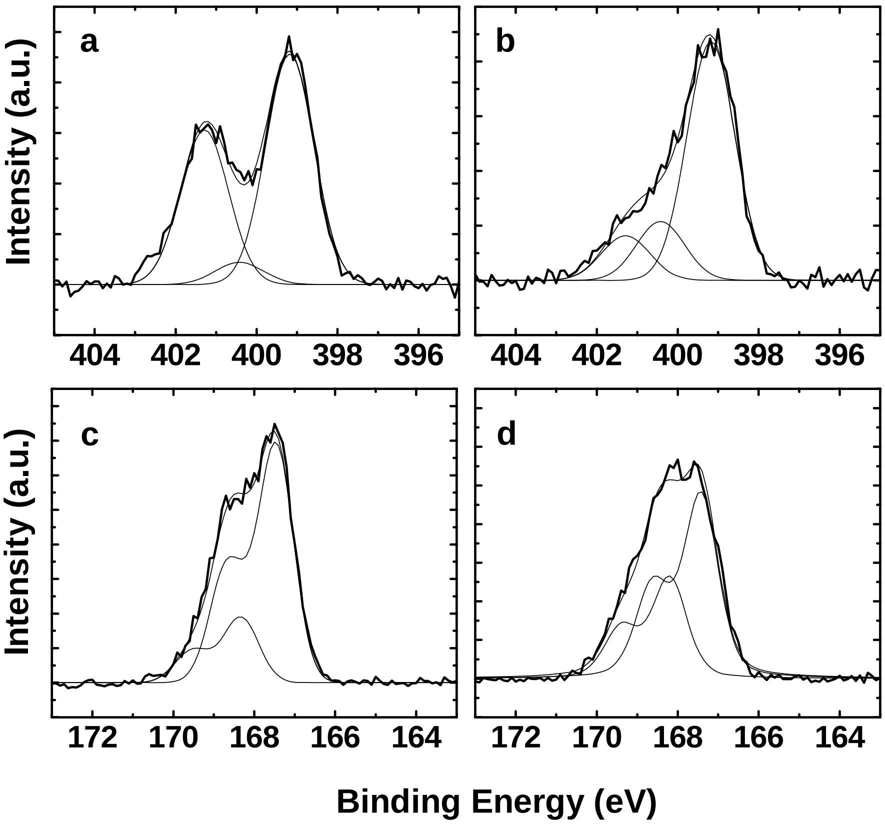

Figure 5.5. XPS nitrogen spectra of (a) untreated and (b) DCA-treated PANI-PAAMPSA, respectively. The nitrogen spectra were deconvoluted into three Gaussian peaks centered at 399.2eV (NH, nitrogen in amines), 400.4eV (N1+, protonated nitrogen), and 401.3eV (N2+, protonated nitrogen). A full width half maximum intensity (FWHM) of 1.4eV is maintained for all three peaks.20, 23, 24 XPS sulfur spectra of (c) untreated PANI-PAAMPSA and (d) DCA-treated PANI-PAAMPSA, respectively. The sulfur spectra were deconvoluted into two doublets. Each doublet was fitted with two sinlgets, i.e., S2p3/2 and S2p1/2. One doublet was fitted with two singlets, S2p3/2 and S2p1/2 centered at 167.5 and 168.7eV, respectively (ionized PAAMPSA, SO3-N+) and the other doublet with S2p3/2 and S2p1/2 at 168.3 and 169.5eV, respectively (neutral PAAMPSA, SO3H).12, 25, 26 All four singlet peaks maintain a FWHM of 1.0eV.

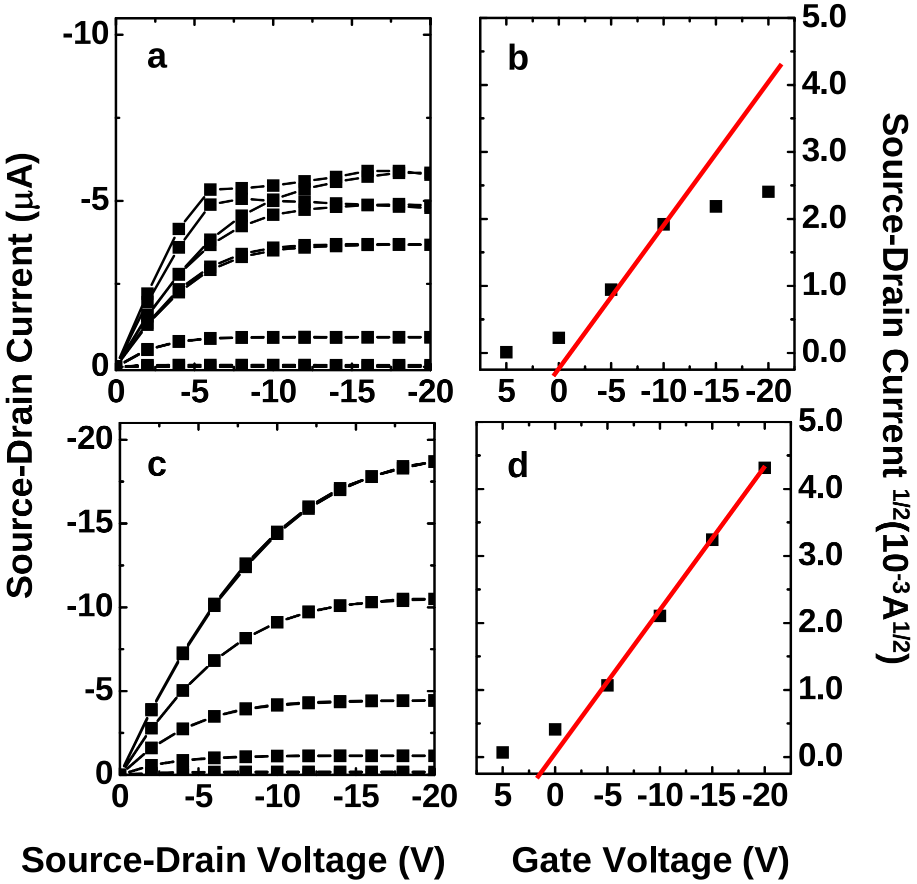

Figure 5.6. (a) Representative I-V characteristics of a bottom-contact pentacene TFT with untreated PANI-PAAMPSA and (b) its corresponding transfer characteristics. The mobility (μ_{sat}) extracted (red line) is 0.17cm^2/V-s. (c) Representative I-V characteristics of a bottom-contact pentacene TFT with DCA-treated PANI-PAAMPSA electrodes and (d) its corresponding transfer characteristics. The μ_{sat} extracted (red line) is 0.19cm^2/V-s. The channel dimensions of both devices are $L \cong 100\mu m$ and $W \cong 1000\mu m$.

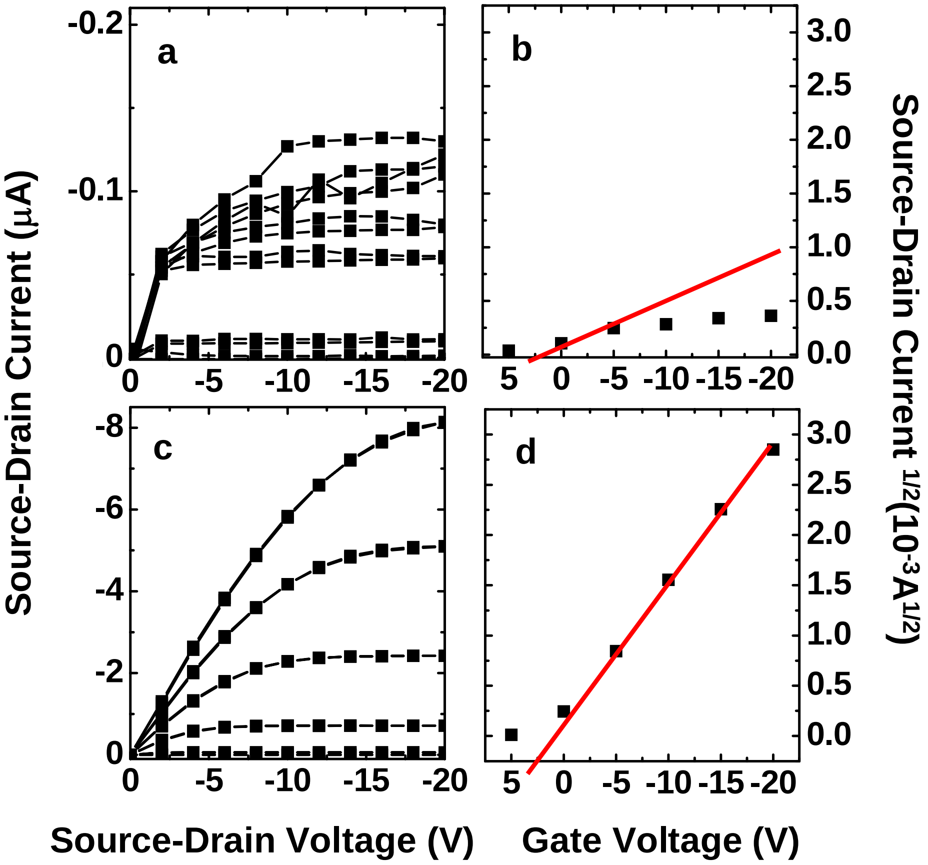

Figure 5.7. (a) Representative I-V characteristics of a bottom-contact DHT-ANT TFT with untreated PANI-PAAMPSA and (b) its corresponding transfer characteristics. The μsat from extracted the slope (red line) is 0.004cm2/V-s. (c) Representative I-V characteristics of a bottom-contact DHT-ANT TFT with DCA-treated PANI-PAAMPSA electrodes and (d) its corresponding transfer characteristics. The μsat extracted from the slope (red line) is 0.09cm2/V-s. The channel dimensions of both devices are *L* ≅ 100μm and *W* ≅ 1000μm.

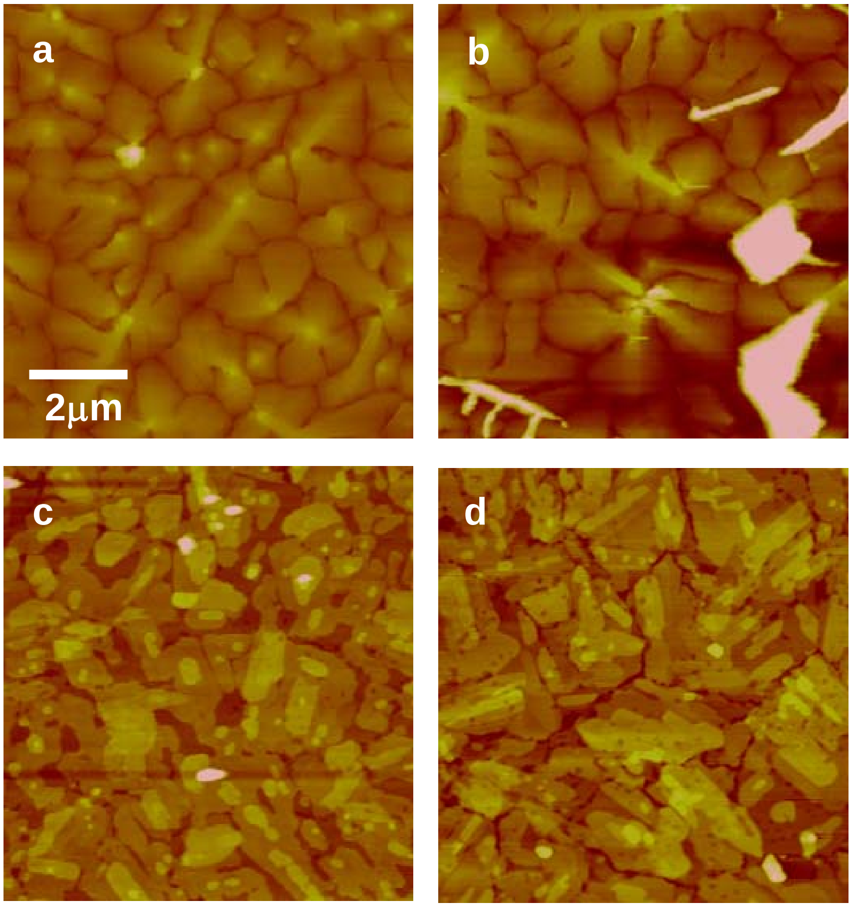

Figure 5.8. AFM images of pentacene (a) in the channel region of a TFT with untreated PANI-PAAMPSA electrodes and (b) in the channel region of a TFT with DCA-treated PANI-PAAMPSA electrodes. AFM images of DHT-ANT (c) in the channel region of a TFT with untreated PANI-PAAMPSA electrodes and (d) in the channel region of a TFT with DCA-treated PANI-PAAMPSA electrodes.

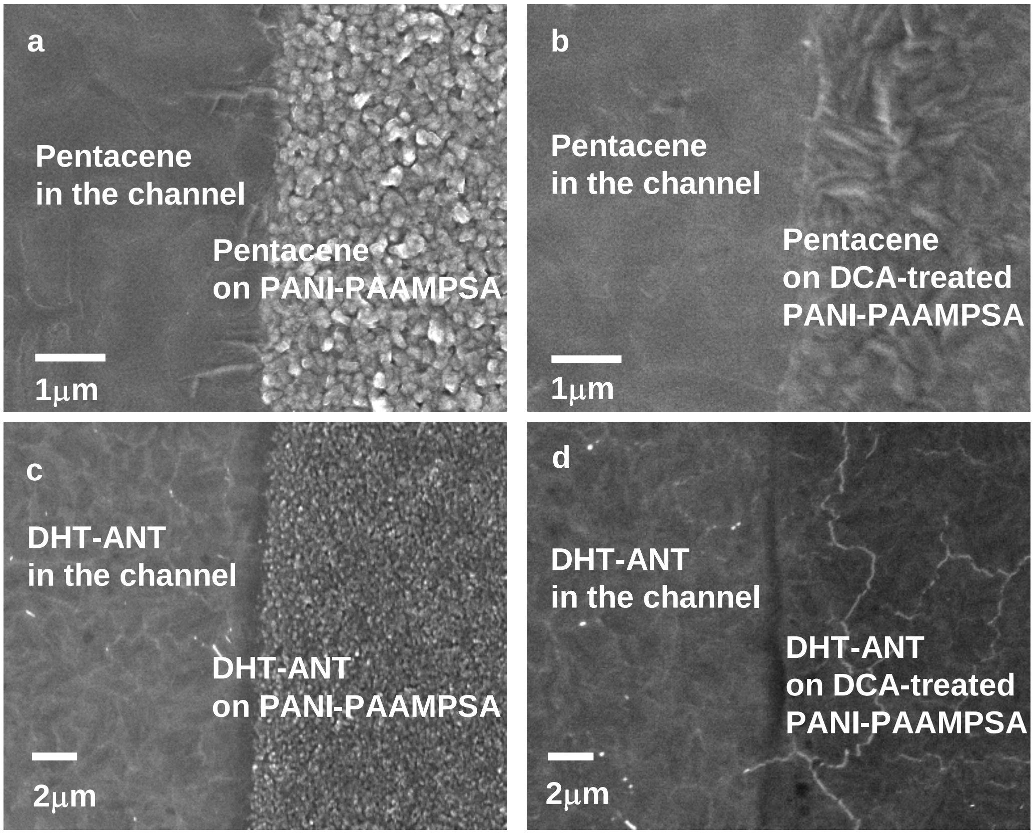

Figure 5.9. SEM images of pentacene (a) at the channel/untreated PANI-PAAMPSA interface and (b) at the channel/DCA-treated PANI-PAAMPSA interface. SEM images of DHT-ANT (c) at the channel/untreated PANI-PAAMPSA interface and (d) at the channel/DCA-treated PANI-PAAMPSA interface.

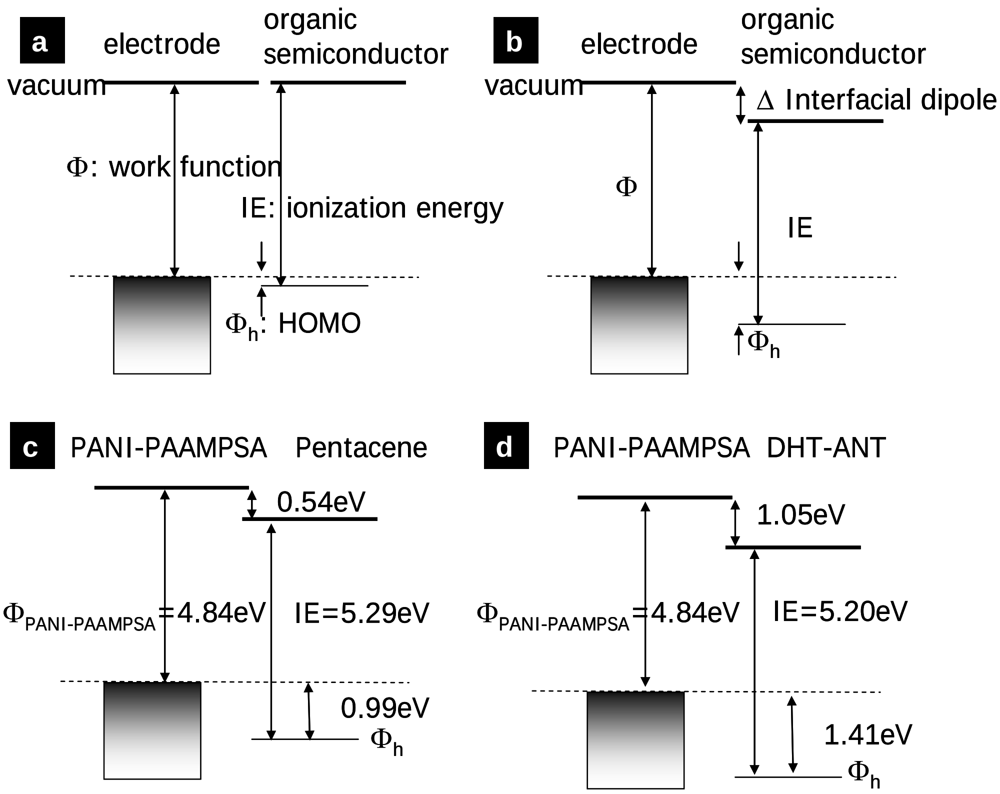

Figure 5.10. (a) The vacuum level alignment of the organic semiconductor and the electrode when the interfacial dipole is absent between the two materials. In such a case, the HOMO level (Φ_h) is simply estimated as the difference between the work function (Φ) of electrode surface and the ionization energy (IE): $\Phi_h = IE - \Phi$. (b) If an interfacial dipole (Δ) exists between the organic semiconductor and the electrode, the HOMO level becomes higher, i.e., $\Phi_h = IE - \Phi + \Delta$. The details of the electronic band structure of (a) pentacene/PANI-PAAMPSA interface and (b) DHT-ANT/PANI-PAAMPSA interface. While pentacene and DHT-ANT have similar ionization energies (5.29 and 5.20eV), a large interfacial dipole leads to a large energy barrier at the DHT-ANT/PANI-PAAMPSA interface compared to that at the pentacene/PANI-PAAMPSA interface.

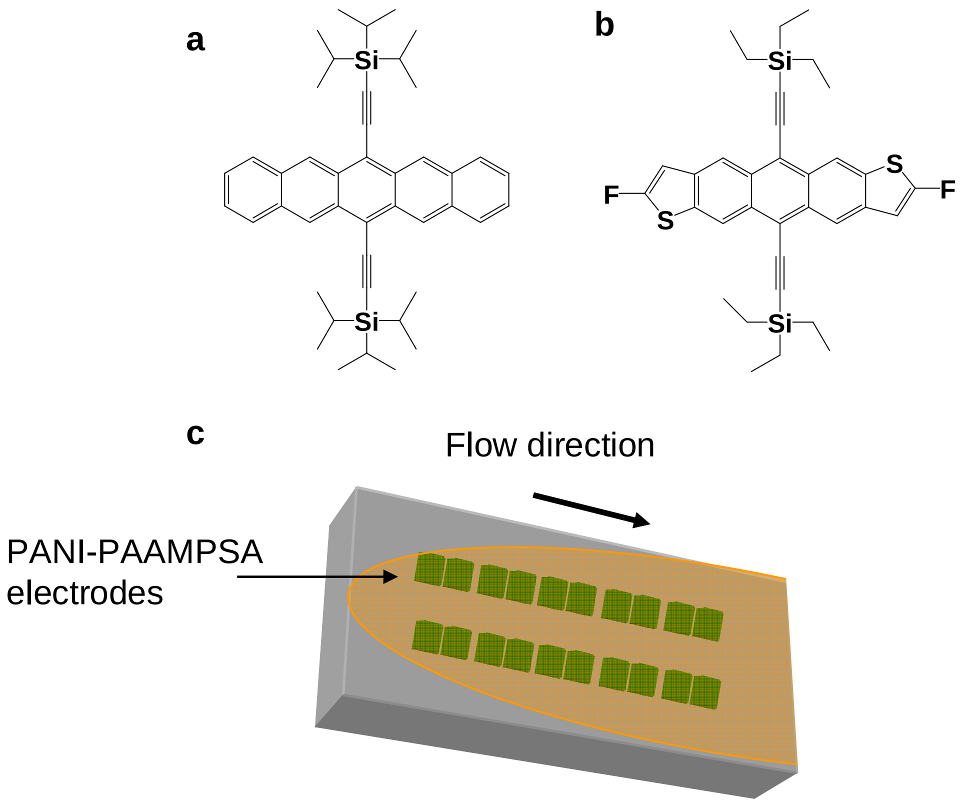

Figure 5.11. The chemical structures of and (a) TIPS-pentacene (b) FTES-ADT. (c) Scheme of flow-induced crystallization on Si/SiO_2 substrates on which a series of PANI-PAAMPSA electrodes have been patterned.

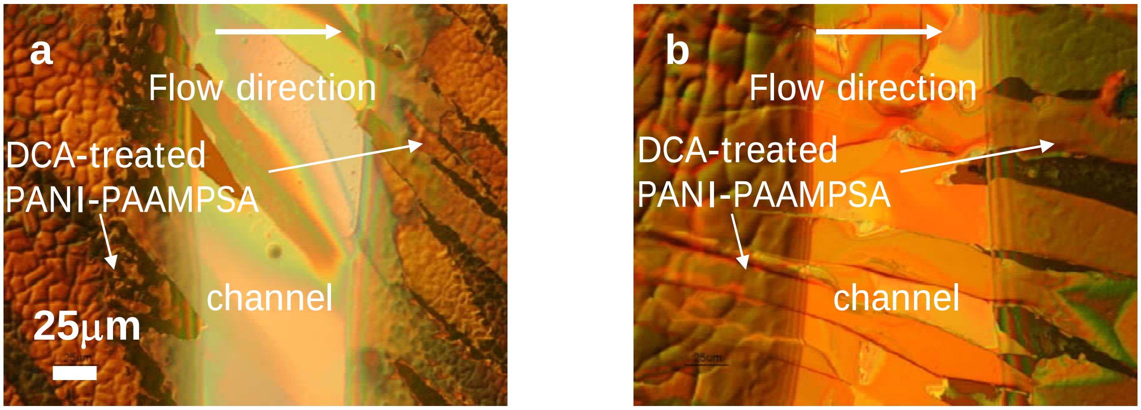

Figure 5.12. Optical micrograph of (a) TIPS-pentacene and (b) FTES-ADT crystals in the channel regions and on DCA-treated PANI-PAAMPSA electrodes. For both cases, a droplet of the organic semiconductor solution flows from left to right during the process, as indicated with the arrows.

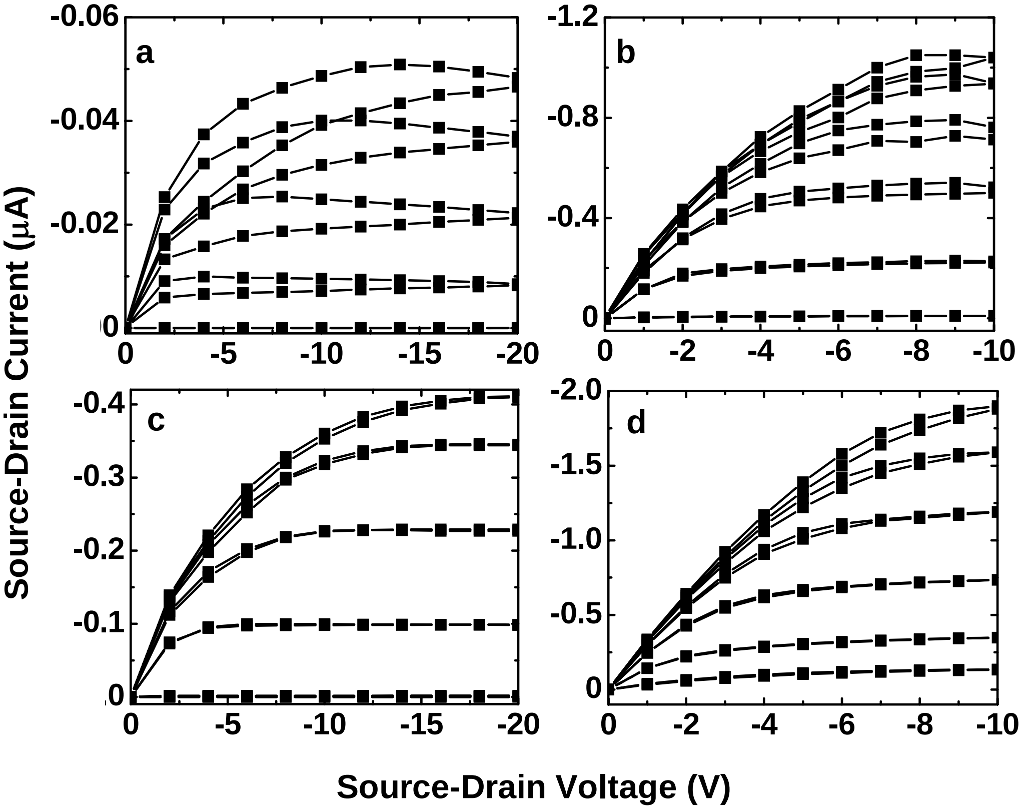

Figure 5.13. Representative I-V characteristics of a bottom-contact TIPS-pentacene TFT (a) with untreated PANI-PAAMPSA electrodes and (b) with DCA-treated PANI-PAAMPSA electrodes. Representative I-V characteristics of a bottom-contact FTES-ADT TFT (c) with untreated PANI-PAAMPSA electrodes and (d) with DCA-treated PANI-PAAMPSA electrodes. The channel dimensions of all these devices are $L \cong 100\mu m$ and $W \cong 1000\mu m$.

REFERENCES

1. A. G. MacDiarmid, A. J. Epstein, *Synthetic Metals* **1994**, *65*, 103.

2. A. G. MacDiarmid, A. J. Epstein, *Synthetic Metals* **1995**, *69*, 85.

3. P. Rannou, A. Gawlicka, D. Berner, A. Pron, M. Nechtschein, D. Djurado, *Macromolecules* **1998**, *31*, 3007.

4. Y. Cao, J. Qiu, P. Smith, *Synthetic Metals* **1995**, *69*, 187.

5. A. R. Hopkins, P. G. Rasmussen, R. A. Basheer, B. K. Annis, G. D. Wignall, W. A. Hamilton, *Synthetic Metals* **1998**, *97*, 47.

6. A. V. Caramyshev, E. G. Evtushenko, V. F. Ivanov, A. R. Barcel, M. G. Roig, V. L. Shnyrov, R. B. van Huystee, I. N. Kurochkin, A. K. Vorobiev, I. Y. Sakharov, *Biomacromolecules* **2005**, *6*, 1360.

7. P. N. Adams, P. Devasagayam, S. J. Pomfret, L. Abell, A. P. Monkman, *Journal of Physics-Condensed Matter* **1998**, *10*, 8293.

8. D. L. Yang, P. N. Adams, L. Brown, B. R. Mattes, *Synthetic Metals* **2006**, *156*, 1225.

9. M. F. Hundley, P. N. Adams, B. R. Mattes, *Synthetic Metals* **2002**, *129*, 291.

10. Y. N. Xia, J. M. Wiesinger, A. G. Macdiarmid, A. J. Epstein, *Chemistry of Materials* **1995**, *7*, 443.

11. G. Horowitz, *Advanced Materials (Weinheim, Germany)* **1998**, *10*, 365.

12. J. Y. Kim, J. H. Jung, D. E. Lee, J. Joo, *Synthetic Metals* **2002**, *126*, 311.

13. R. Menon, C. O. Yoon, D. Moses, A. J. Heeger, Y. Cao, *Physical Review B: Condensed Matter and Materials Physics* **1993**, *48*, 17685.

14. L. Zuppiroli, M. N. Bussac, S. Paschen, O. Chauvet, L. Forro, *Physical Review B* **1994**, *50*, 5196.

15. *CRC handbook of chemistry and physics*, CRC Press, Cleveland, OH **2007**.

16. R. J. Fessenden, J. S. Fessenden, *Organic chemistry*, Brooks/Cole, Pacific Grove, CA **1994**.

17. W. Zheng, M. Angelopoulos, A. J. Epstein, A. G. MacDiarmid, *Macromolecules* **1997**, *30*, 2953.

18. K. Potje-Kamloth, B. J. Polk, M. Josowicz, J. Janata, *Chemistry of Materials* **2002**, *14*, 2782.

19. D. W. Hatchett, M. Josowicz, J. Janata, *Journal of Physical Chemistry B* **1999**, *103*, 10992.

20. E. T. Kang, K. G. Neoh, K. L. Tan, *Progress in Polymer Science* **1998**, *23*, 277.

21. H. Erdemi, A. Bozkurt, W. H. Meyer, *Synthetic Metals* **2004**, *143*, 133.

22. J. L. Qiao, T. Hamaya, T. Okada, *Journal of Materials Chemistry* **2005**, *15*, 4414.

23. J. Yue, A. J. Epstein, *Macromolecules* **1991**, *24*, 4441.

24. H. Moon, R. Zeis, E.-J. Borkent, C. Besnard, A. J. Lovinger, T. Siegrist, C. Kloc, Z. Bao, *Journal of American Chemical Society* **2004**, *126*, 15322.

25. G. Greczynski, T. Kugler, W. R. Salaneck, *Thin Solid Films* **1999**, *354*, 129.

26. K. Z. Xing, M. Fahlman, X. W. Chen, O. Inganaes, W. R. Salaneck, *Synthetic Metals* **1997**, *89*, 161.

27. L. Sun, S. C. Yang, *Polymer Preprints* **1992**, *33*, 379.

28. H. Meng, F. Sun, M. B. Goldfinger, G. D. Jaycox, Z. Li, W. J. Marshall, G. S. Blackman, *Journal of the American Chemical Society* **2005**, *127*, 2406.

29. K. P. Pernstich, S. Haas, D. Oberhoff, C. Goldmann, D. J. Gundlach, B. Batlogg, A. N. Rashid, G. Schitter, *Journal of Applied Physics* **2004**, *96*, 6431.

30. N. Koch, A. Kahn, J. Ghijsen, J. J. Pireaux, J. Schwartz, R. L. Johnson, A. Elschner, *Applied Physics Letters* **2003**, *82*, 70.

31. L. Burgi, T. J. Richards, R. H. Friend, H. Sirringhaus, *Journal of Applied Physics* **2003**, *94*, 6129.

32. S. M. Sze, *Physics of Semiconductor Devices*, John Wiley & Sons, Inc., New York **1981**.

33. H. Ishii, K. Sugiyama, E. Ito, K. Seki, *Advanced Materials (Weinheim, Germany)* **1999**, *11*, 605.

34. M. M. Payne, S. R. Parkin, J. E. Anthony, C.-C. Kuo, T. N. Jackson, *Journal of the American Chemical Society* **2005**, *127*, 4986.

35. K. C. Dickey, J. E. Anthony, Y.-L. Loo, *Advanced Materials (Weinheim, Germany)* **2006**, *18*, 1721.

36. K. C. Dickey, S. Subramanian, J. E. Anthony, L.-H. Han, S. Chen, Y.-L. Loo, *Applied Physics Letters* **2007**, *90*, 244103/1.

37. S. K. Park, C.-C. Kuo, J. E. Anthony, T. N. Jackson, *Technical Digest - International Electron Devices Meeting* **2005**, 113.

38. J. E. Anthony, *Chemical Reviews* **2006**, *106*, 5028.

39. W. H. Lee, D. H. Kim, Y. Jang, J. H. Cho, M. Hwang, Y. D. Park, Y. H. Kim, J. I. Han, K. Cho, *Applied Physics Letters* **2007**, *90*, 132106/1.

40. M. M. Payne, S. R. Parkin, J. E. Anthony, *Journal of the American Chemical Society* **2005**, *127*, 8028.

Chapter 6: Direct correlation between morphologies, molecular orientation, and work functions of organic semiconductor thin films

Understanding the molecular structure of PANI-PAAMPSA, is critical for the engineering of its electrical conductivity. In this same vein, understanding the structure-function relationships of organic semiconductors – which comprise the active layers of TFT – is important as well. Several examples have demonstrated how the morphology[1-5] and molecular orientation[5-7] of organic semiconductor thin films can affect charge transport properties when the materials are incorporated in functional TFTs. Additionally, understanding how molecular structures affect electronic band structures of organic semiconductor is critical to improve performance of organic TFTs and organic junctions in which charge transport is controlled by differences in the electronic band structures of the two materials in contact.[8] Such relationships are well understood in inorganic semiconducting materials. For example, Kahn[9] and Palmstrøm[10, 11] research groups have demonstrated that the electronic band structures, e.g., electron affinity and work function, can be correlated with the surface reconstruction of GaAs(100). Palmstrøm groups further show how changes in the electronic band structures can impact the characteristics of Schottky junctions.[11] Established relationships based on such understanding have led to better control and improvement of device performance. While there has been significant efforts to understand the relationship between the molecular structures and the electronic structures of organic semiconductors, these studies have focus on either on characterizing the molecular orientation and packing[12-14] or on elucidating interfacial electronic band structures on various substrates.[15-17] No attempts have been made to correlate the molecular structures with the electronic structures of organic semiconductors.

We recently found that the molecular orientation of organic semiconductor thin films can directly affect their electronic structures. Specifically, we directly correlated the morphology, molecular orientation, and work function of two organic semiconductors. i.e., pentacene and dihexylthiophene anthracene (DHT-ANT),[18] on various substrates. We prepared six different substrates as described in Chapter 2, i.e., hexamethyl disilazane (HMDS)-treated silicon (Si), PANI-PAAMPSA-coated Si, bare gold, HMDS-treated gold, and solvent-cleaned gold. To assess the effect of substrates on the growth behaviors of vacuum-deposited organic semiconductors, 50nm of pentacene and 40nm of DHT-ANT were then thermally evaporated on all these substrates.

To examine the morphology of pentacene and DHT-ANT on the various substrates, we carried out scanning electron microscopy (SEM) experiments. Figures 6.1a through f contain SEM images of pentacene on the substrates listed above. Figure 6.1a reveals two-dimensional pentacene grains on HMDS-treated Si.[5, 19-23] The sizes of these pentacene grains range from 3 to 5μm. On the contrary, smaller pentacene grains (100-200nm) are found on PANI-PAAMPSA-coated Si, as shown in Figure 6.1b. Consistent with our previous observation, pentacene appear to adopt the rough topography of the surface when deposited on PANI-PAAMPSA.[5] Figure 6.1c reveals pentacene grains on solvent-cleaned gold. Pentacene exhibits similar morphology to that shown in Figure 6.1a but the grains are smaller (0.8-1μm). Pentacene, however, adopts a drastically different morphology when deposited on HMDS-treated gold, as shown in Figure 6.1d. These pentacene grains appear to adopt a one-dimensional feather-like morphology. These feather-like pentacene grains are interconnected. Figure 6.1e reveals a similar feather-like morphology of pentacene grains on bare gold.

Figures 6.1f through j contain SEM images of DHT-ANT on the various different substrates. Figure 6.1f reveals the morphology of DHT-ANT on HMDS-treated Si. We observe two-dimensional DHT-ANT grains ranging from 2 to 3μm.[18] Figure 6.1g shows that DHT-ANT conforms to the rough surface morphology when deposited on PANI-PAAMPSA-coated Si. Figure 6.1h shows DHT-ANT on solvent-cleaned gold. Figure 6.1i reveals dramatically different morphology of DHT-ANT grains deposited on HMDS-treated gold. We observe one-dimensional rod-like morphology on HMDS-treated gold. Figure 6.1j reveals two-dimensional grains when DHT-ANT is deposited on bare gold.

To look more closely at how these molecules pack to form these grains on the different substrates, we carried out near-edge X-ray absorption fine structure spectroscopy (NEXAFS)[24, 25] in collaboration with Dmitry Krapchetov, a fellow graduate student in our group. Figures 6.2a and b contain pre- and post-edge normalized angle-dependent carbon-edge NEXAFS spectra of pentacene deposited on HMDS-treated Si and HMDS-treated gold, respectively. The spectra exhibit two sharp absorption at 284 and 285eV associated with the $C1s \rightarrow \pi^*$ transitions of the fused rings of pentacene and two broad features at 294 and 301eV attributed to the $C1s \rightarrow \sigma_1^*$ and $C1s \rightarrow \sigma_2^*$ transitions, respectively.[12, 26]

We examined the angular dependence of the NEXAFS spectra of pentacene on the different substrates.[5, 25] Specifically, we quantified the ensemble-average orientation of pentacene using a dichroic ratio (DR), which measures how the molecules are preferentially orientated on the surface:[27]

$$DR = \frac{I(75^\circ) - I(20^\circ)}{I(75^\circ) + I(20^\circ)} \qquad (6.1)$$

where $I(\theta)$ represents the combined integrated intensities of the π* resonances at 284 and 285eV obtained at an x-ray incidence angle of θ relative to the substrate surface. DR is thus a measure of the level of anisotropy of molecular ring orientation in the organic semiconductor. According to the NEXAFS dipole selection rules,[27, 28] DR > 0 indicates that the fused rings are preferentially oriented perpendicular to the surface, while DR < 0 indicates that the fused rings are preferentially oriented parallel to the surface. Correspondingly, DR ≈ 0 indicates the absence of any preferential orientation. Dichroic ratios derived for each set of NEXAFS spectra are included in Figure 6.2. We note that this analysis does not provide any insight into how the molecular long axis is oriented with respect to the substrate surface, i.e., with NEXAFS, we are not able to distinguish whether pentacene is oriented with its long axis perpendicular or parallel to the substrate.

Figure 6.2a shows the NEXAFS spectra of pentacene deposited on HMDS-treated Si. Its DR is 0.53. This positive value of DR indicates that the fused rings of pentacene are generally oriented perpendicular to the HMDS-treated Si substrate surface. We observe a similar upright orientation in pentacene deposited on PANI-PAAMPSA-coated Si and on solvent-cleaned gold with DR = 0.47 and DR = 0.50, respectively (data not shown). In contrast, Figure 6.2b shows the NEXAFS spectra of pentacene deposited on HMDS-treated gold. The DR from these spectra is -0.26. The negative value of DR suggests that the fused rings are generally oriented parallel to the surface. Similar orientation is observed for pentacene on bare gold with DR = -0.22 (data not shown). Macroscopically, these pentacene films exhibit a feather-like morphology. Our results suggest that when pentacene is preferentially oriented with its fused rings perpendicular to the substrate, the macroscopic grains are two-dimensional as opposed to being feather-like.

Figures 6.2c and d contain representative pre- and post-edge normalized angle-dependent NEXAFS spectra of DHT-ANT deposited on HMDS-treated Si and HMDS-treated gold, respectively. Similar to pentacene, we identify two absorptions at 284 and 285eV associated with the C1s→π* transitions of the fused rings of anthracene and two broad absorptions at 294 and 301eV associated with the C1s→σ* transitions of both the anthracene backbone and the alkyl side chains.[29, 30] To examine the fused ring orientation in DHT-ANT deposited on various substrates, we again quantify the dichroic ratios of the π* intensities using Equation 6.1. From the NEXAFS spectra in Figure 6.2c, DR is 0.48, which indicates that the fused rings of DHT-ANT are oriented perpendicular to HMDS-treated Si. DHT-ANT is oriented in a similar fashion when it is deposited on PANI-PAAMPSA-coated Si (DR = 0.39), solvent-cleaned gold (DR = 0.50), and bare gold (DR = 0.49) (data not shown). In contrast, we extracted DR = -0.50 from the NEXAFS spectra of DHT-ANT deposited on HMDS-treated gold (Figure 3b-ii), indicating that the fused rings of DHT-ANT are generally oriented parallel to this substrate surface. These trends – like those observed with NEXAFS of pentacene – suggest that a ring parallel to substrate orientation manifests itself as one-dimensional feather- or rod-like grains at a larger length scale. Since our DR analysis does not provide any information about how the molecular long axis is oriented with respect to the substrate, Fourier transform infrared (FTIR) spectroscopy is used to provide such complementary information so we get a more complete picture.

For ease of discussion, we shall define three primary orientation that these molecules can adopt on the various substrates. Specifically, these molecules can "lie flat", be oriented "upright", or "edge-on", as illustrated with pentacene in Figure 6.3. Here, pentacene is shown with a coordinate system in which its ***x***-axis is aligned with the long molecular axis of the fused rings, its ***y***-axis along the short molecular axis of the fused rings, and its ***z***-axis is pointing in and out of the fused rings. These axes also correspond to the transitional dipole moment directions of the vibrations of conjugated C-C and C-H bonds of the fused rings. The "lying flat" orientation represents the orientation where the ***x***- and ***y***-axes are parallel to the substrate surface and the ***z***-axis is perpendicular to the surface. The "upright" orientation represents the orientation where ***z***- and ***x***-axes are parallel to the surface and the ***y***-axis is perpendicular to the surface. Finally, the "edge-on" orientation is the orientation in which ***y***- and ***z***-axes are parallel to the surface and the ***x***-axis is perpendicular to the surface.

We carried out FTIR experiments in collaboration with Dmitry Krapchetov in our group. Specifically, we used refection absorption infrared spectroscopy (RAIRS)[31, 32] to determine the orientation of the molecules (i.e., how the molecule's long axis is oriented with respect to HMDS-treated, bare, and solvent-cleaned gold substrates). Because undoped Si is transparent to IR,[33] angle-resolved transmission IR[34] was used to determine the orientation of molecule axis of pentacene and DHT-ANT on HMDS-treated and PANI-PAAMPSA-coated Si substrates.

Figure 6.4 shows the schematic of our RAIRS experiments. We use p-polarized light with a grazing incidence angle that is 80° away from the surface normal to probe the organic semiconductor thin films. The incident p-polarized light consist of components both perpendicular and parallel to the substrate surface. Due to the incidence angle, the magnitude of the parallel component is much smaller than that of the perpendicular component. The parallel component is further nulled at a gold surface due to the interactions with the electromagnetic field of free electrons on the surface,[35] so only the perpendicular component interacts with vibrations of pentacene. On gold, RAIRS is therefore only sensitive to vibrations whose transitional dipole moment components normal to substrate surface. For example, if pentacene adopts the upright orientation on gold, as shown in Figure 6.4, the intensity of the resonance corresponding to the vibrations along the ***y*** axis will be maximized, while those associated with vibrations along either the ***x*** or the ***z*** axis will be suppressed. [31] Thus, comparing the resonance intensities of the sample relative to the resonance intensities in an isotropic pentacene sample allows us to qualitatively determine the orientation of the molecule.

Figure 6.5a contains the RAIRS spectra of pentacene deposited on HMDS-treated gold (i) and on bare gold (ii), and on solvent-cleaned gold (iii). Figure 6.5a-(iv) represents a transmission IR spectrum of pentacene powder dispersed in KBr taken from the literature.[32] On top of Figure 6.5a, we show the chemical structure of pentacene with a coordinate system that is similar to that used in Figure 6.3. These axes also correspond to the transitional dipole moment directions of the vibrations of pentacene. By referring to the literature,[32] we have been able to identify peaks associated the vibrations of pentacene along each of the transitional dipole moment directions. In Figure 6.5a, we point out the major peaks attributed to the vibrations in the three transitional dipole moment directions with dashed lines. Specifically, we identify the two most intense peaks at 730 and 905 cm^{-1} attributed to the vibrations of pentacene along the ***z*** axis; peaks at 1445 and 1499 cm^{-1} associated with the vibrations of pentacene in the ***y*** axis; peaks at 1299 and 1344 cm^{-1} associated with the vibrations of pentacene in the ***x*** axis.

Figures 6.5a-i and ii present RAIRS spectra of pentacene deposited on HMDS-treated and on bare gold, respectively. In both of these spectra, the peaks associated with vibrations of pentacene along the ***z*** and the ***x*** axes dominate the signal compared to the reference spectrum of pentacene powder. Since RAIRS is selective to the transitional dipole moments of vibration that are normal to the surface only, this observation indicates that the ***z*** and the ***x*** axes of pentacene are oriented along the substrate normal. These results suggest that pentacene adopts the "lying flat" orientation in which the long molecular axis of pentacene is parallel to the surface and the short axis is slightly tilted away from the surface when deposited on both HMDS-treated gold and bare gold. This orientation necessitates that the fused rings be parallel to the substrate surface; this orientation is consistent with that we had previously extracted from our NEXAFS experiments.

Figure 6.5a-iii presents the RAIRS spectrum of pentacene deposited on solvent-cleaned gold. This spectrum is drastically different from those of pentacene on HMDS-treated and bare gold.[32] In contrast to Figure 6.5a-i and ii, the peaks associated with transitional dipole moments in the ***y*** direction (1445, 1499, and 1537cm^{-1}) dominate this spectrum. The intensities of these peaks are higher than those in the reference spectrum of pentacene powder (iv).[32] Considering that RAIRS is selective to the transitional dipole moments normal to the substrate surface, the dominance of these peaks indicates that pentacene is oriented "upright" on solvent-cleaned gold. The growth of pentacene appears to be significantly different on solvent-cleaned gold compared to on HMDS-treated and bare gold. Later in this chapter, we will discuss how the solvent cleaning process affects the surface chemistry of gold, which in turn influences the growth of pentacene.

Figure 6.5b contains RAIRS spectra of DHT-ANT deposited on (i) HMDS-treated gold, (ii) bare gold, and (iii) solvent-cleaned gold. Figure 6.5b-(iv) represents a transmission IR spectrum of DHT-ANT powder in KBr. On top of Figure 5.6b, the chemical structure of DHT-ANT with its corresponding transitional dipole moment coordinate system. The orientation of the molecular axis of DHT-ANT is determined based on the anthracene ring plane. We assigned only the major peaks associated with vibrations of the ring plane of anthracene along the ***z*** (799 and 900cm^{-1}) and the ***x*** (1624cm^{-1}) axes.[36] We cannot conclusively assign the group of peaks in 1420-1500 cm^{-1} because the vibrations of the ring plane of anthracene[36] as well as vibrations due to the thiophene rings,[37] and the alkyl side groups[37] all exhibit resonances in this region. Figure 6.5b-i contains the RAIRS spectrum of DHT-ANT deposited on HMDS-treated gold. The peak associated with the vibration in the ***z***-axis is very intense while that associated with the vibration along the ***x***-axis is weak compared to the corresponding peak intensities in the isotropic DHT-ANT spectrum (iv). This comparison suggests that DHT-ANT adopts the "lying flat" orientation with its ***z***-axis perpendicular to the substrate surface when deposit on HMDS-treated gold. This "lying flat" orientation is in the agreement with a negative DR of NEXAFS (Figure 6.2d), and is correlated with the rod-like morphology we observed for DHT-ANT deposited on HMDS-treated gold (Figure 6.1i).

Figures 6.5b-ii and-iii show RAIRS spectra of DHT-ANT deposited on both solvent-cleaned gold and bare gold, respectively. We observe that the peak associated with the vibration of the anthracene fused rings along the ***x*** axis (1624cm^{-1}) is more intense than the peaks associated with vibrations along the ***z*** axis (799 and 900cm^{-1}). When compared with the spectrum of the isotropic DHT-ANT reference (iv), the peak intensity of the vibration in the ***x***-axis is higher than that in the isotropic spectrum. This observation suggests that DHT-ANT adopts the "edge-on" orientation (see Figure 6.5c) when deposited on solvent-cleaned gold and bare gold. While this "edge-on" orientation is not conclusively determined with NEXAFS, it is now readily determined with FTIR.

We employed angle-resolved transmission IR with p-polarized light to investigate the molecular axis orientation of pentacene and DHT-ANT on both HMDS-treated and PANI-PAAMPSA-coated Si. Figure 6.6 illustrates the transmission IR experiment setup with p-polarized light. Specifically, we probed our sample at two different angles, i.e., normal incidence (0° from the surface normal) and near-grazing incidence (68° from the surface normal). When the incident light is normal to the substrate, p-polarized light can selectively probe the vibrations of molecules that are parallel to the surface.[34, 38] If, on the other hand, a near-grazing IR incidence (68°) is used, p-polarized light is selective for vibrations that are perpendicular to the surface.[34, 38] By identifying peaks whose intensities change as a function of the IR incident angle, we can determine how the molecular axis of the organic semiconductors is oriented. For example, if pentacene is oriented upright on the substrate surface, as shown in Figure 6.6, the vibrations of pentacene along the long molecule axis (***y*** axis) will be suppressed when probed with IR at the normal incidence. This vibration, however, will dominate when a near-grazing IR incidence is used.

Figure 6.7a contains transmission IR spectra of pentacene deposited on (i) HMDS-treated Si and (ii) PANI-PAAMPSA-coated Si acquired at normal (0°) and near-grazing (68°) IR incidence. We labeled the vibrations of pentacene along their corresponding transitional dipole moment directions for clarity. In the spectra of pentacene deposited on both HMDS-treated Si and PANI-PAAMPSA-coated Si, the peaks associated with the vibrations along the ***y***-axis are relatively weak at normal IR incidence and become stronger at near-grazing incidence compared to the corresponding peak in the isotropic spectrum of pentacene powder. These observations indicate that pentacene adopts the "upright" orientation (Figure 6.3b) in which its long molecule axis is oriented perpendicular to both HMDS-treated Si and PANI-PAAMPSA-coated Si surface.

Figure 6.7b contains transmission IR spectra of DHT-ANT deposited on (i) HMDS-treated Si and (ii) PANI-PAAMPSA-coated Si acquired at normal (0°) and near-grazing (68°) IR incidence. In the spectra of DHT-ANT deposited on both HMDS-treated Si and PANI-PAAMPSA-coated Si surfaces, the peaks associated with vibrations along the ***x***-axis are weak at normal IR incidence, but become stronger at near-grazing IR incidence compared to the corresponding peak intensities of the isotropic spectrum of DHT-ANT powder. These observations suggest that DHT-ANT adopt the "edge-on" orientation (Figure 6.3c) where the short molecular axis is perpendicular to the surface.

Detailed FT-IR experiments carried out in reflection mode for samples on gold and in transmission mode for samples on Si have allowed us to determine how the molecules are oriented on these different substrates. This information is corroborated by results from our NEXAFS experiments. There also appear to be a correlation between the molecular orientation and the morphology of the organic semiconductors at a larger length scale, as samples with fused rings parallel to substrates exhibit one-dimensional type grains whereas samples with fused rings perpendicular to substrates exhibit two-dimensional grains. These results implicate that growth habits of the organic semiconductors are highly sensitive to substrate surface.

It has been suggested that the molecular orientation of organic semiconductors is mainly governed by the subtle competition between the intermolecular interactions and molecule-substrate interactions.[12, 13, 39] For example, the "lying flat" orientation has been reported for pentacene on Au(111)[13, 40, 41] and bare gold[12]. Such orientation is speculated to stem from strong interactions between the π clouds of pentacene and the d-orbitals of gold.[12, 13, 39] If such interactions are suppressed and the intermolecular interactions of pentacene increased, the way pentacene is oriented on the surface should change accordingly. Indeed, it has been shown that pentacene can be oriented with its rings perpendicular to the surface when deposited on thiol-treated gold substrates. In this case, the thiols are believed to suppress the interactions between pentacene and gold.[12, 13] This result suggests the possibility of controlling the orientation of pentacene through manipulation of surface chemistry.

To examine the surface chemistry of our gold substrates, we conducted x-ray photoelectron spectroscopy (XPS) on (i) solvent-cleaned gold, (ii) HMDS-treated gold, (iii) HMDS-treated gold followed by solvent-cleaning, i.e., NMP cleaning, and on (iv) bare gold. We baseline subtracted each spectrum using a Shirley background and then smoothed the spectrum using the boxcar routine with seven points. Figure 6.8a contains XPS Si2p spectra of the samples listed above. While we may expect to observe silicon peaks associated with HMDS on HMDS-treated gold and HMDS-treated gold substrate that had been cleaned with NMP, we observe a peak centered at 101.5eV only in HMDS-treated gold (Figure 6.8a-ii), but not in HMDS-treated gold followed by solvent cleaning (Figure 6.8a-iii). That HMDS can be removed upon solvent cleaning suggests that it is only physisorbed onto gold during its deposition, and can be readily displaced by NMP during cleaning. Figure 6.8b-i shows the XPS N1s spectrum of solvent-cleaned gold; it exhibits two peaks centered at 398.3 and 399.9eV. These peaks are attributed to the nitrogen in NMP. We also observe similar peaks in the N1s spectrum of HMDS-treated gold followed by solvent-cleaning, as shown in Figure 6.8a-iii. These observations suggest that NMP molecules adsorb on gold upon solvent cleaning. Its interaction with gold is likely also stronger than HMDS since it is able to displace HMDS that was originally physisorbed on the surface. Given the relatively weak interactions between HMDS and gold, we speculate that pentacene, like NMP, is able to displace HMDS when deposited on HMDS-treated gold surfaces. In doing so, the π clouds of pentacene can interact directly with the underlying gold, leading to a preferential orientation where the rings are parallel to the gold substrate. Unlike HMDS, NMP molecules appear to be more strongly adsorb on gold. Pentacene is thus unable to displace NMP on the solvent-cleaned surface. Consequently, pentacene adopts the “upright” orientation on NMP-adsorbed gold whether this surface is created directly by solvent cleaning or by displacing HMDS.

While the “lying flat” orientation is observed in pentacene on both HMDS-treated and bare gold, this orientation is only observed in DHT-ANT when it is deposited on HMDS-treated gold, but not in DHT-ANT that is deposited on bare gold. This disparity is speculated to stem from differences in the chemical structures of DHT-ANT and pentacene. DHT-ANT has a smaller number of fused benzene rings (three as opposed to five in pentacene); the interactions between DHT-ANT and bare gold are thus likely to be weaker than those between pentacene and bare gold. Also, our bare gold substrates are stored in air before organic semiconductor deposition. They may thus contain contaminants, most likely hydrocarbons that are physisorbed on the surface prior to deposition. The “lying flat” orientation of pentacene on bare gold suggests that pentacene is able displace the contaminants on gold, thereby maximizing molecule-substrate interactions. Given the weaker interactions between DHT-ANT and gold, DHT-ANT may not be capable of displacing the contaminants entirely. DHT-ANT thus adopts the “edge-on” orientation on bare gold substrates as well as the other substrates (except HMDS-treated gold). Exactly what causes DHT-ANT to adopt the “edge-on” orientation on bare gold, as opposed to the “upright” orientation is not clear. We speculate this may stem from the presence of alkyl side groups, which also have a tendency to crystallize.[18]

Thus far, we have correlated the morphologies of two organic semiconductors on a larger length scale with their molecular orientation. We have shown that the controlling the orientation of the organic semiconductors is possible through the modification and manipulation of the surface chemistry. In the next paragraphs, we shall show how the details of structure – both in terms of grains and molecular orientation – are correlated with the materials' electronic properties.

We carried out ultraviolet photoemission spectroscopy (UPS)[15, 42] experiments to quantify the work functions of pentacene and DHT-ANT on the different substrates. UPS experiments were conducted with the help with Dr. Chris Zangmeister at the National Institutes of Standards and Technologies (NIST). Considering the thicknesses of these films, i.e., 50 and 40nm for pentacene and DHT-ANT, respectively, UPS probes only the surfaces of these films, so our measurements reflect the properties of the films themselves and not of the interface. Figure 6.9a contains the UPS spectra of pentacene on the different substrates. As described in Chapter 2, the work functions of the organic semiconductor thin films are calculated by subtracting the vacuum cut-offs from the total source photon energy of the source (21.22eV). For example, the vacuum cut-off of pentacene on HMDS-treated Si is 17.06eV (labeled with a solid line in Figure 6.9a-i). The work function of pentacene on HMDS-treated Si is thus calculated as 21.22eV-17.06eV=4.16eV. Similarly, we extracted the work functions of pentacene deposited on the other substrates. All of the work functions of pentacene are listed in Table 6.1. The work functions of pentacene ranges from 4.16 to 4.35eV on (i) HMDS-treated Si, (ii) PANI-PAAMPSA-coated Si, and (iii) solvent-cleaned gold. As shown in Table 6.1, these pentacene films exhibit the "upright" orientation with positive DR from NEXAFS. In contrast, the work functions of pentacene are 4.78 and 4.77eV on (iv) HMDS-treated gold and on (v) bare gold (Figure 6.9a-iv and v). The vacuum cut-offs for (iv) are labeled with a dashed line in Figure 6.9a and is shifted to the left compared to that for (i)-(iii). These work functions are higher by ~0.5eV than those of pentacene thin films on the other substrates (i, ii, and iii). These pentacene films exhibit the “lying flat” orientation, as shown in Table 6.1. It appears that the “lying flat” orientation is not only directly correlated with the feather-like morphology, but also with a higher work function. These correlations imply that controlling of the electronic properties is also possible by altering the molecular orientation of the organic semiconductor.

Figure 6.9b contains the UPS spectra of DHT-ANT thin films on the different substrates. Similar to the case of pentacene, we have extracted the work functions of DHT-ANT from these spectra and have summarized them in Table 6.1. The work functions of DHT-ANT films range from 3.32 to 3.79eV on (i) HMDS-treated Si, (ii) PANI-PAAMPSA-coated Si, (iii) solvent-cleaned gold, and (v) bare gold. The work function of DHT-ANT is 4.28eV on (iv) HMDS-treated gold, which is at least 0.5eV higher compared to the work functions of DHT-ANT on the other substrates. Again, DHT-ANT film having the “lying flat” orientation exhibits a higher work function compared to those having the “edge-on” orientation, as shown in Table 6.1.

Table.6.1 – Summary of work functions, HOMO levels, ionization energies, DRs, and molecular orientations of pentacene and DHT-ANT on different substrates.

Substrate	**Work function (eV)**	**HOMO (eV)**	**NEXAFS DR**	**Orientation**
	Pentacene			
HMDS-treated Si	4.16	0.91	0.53	upright
PANI-PAAMPSA	4.30	0.99	0.47	upright
Solvent-cleaned Au	4.35	0.91	0.50	upright
HMDS-treated Au	4.78	0.93	-0.26	lying flat
Bare Au	4.77	0.94	-0.22	lying flat
	DHT-ANT			
HMDS-treated Si	3.32	1.48	0.48	edge-on
PANI-PAAMPSA	3.79	1.41	0.39	edge-on
Solvent-cleaned Au	3.38	1.46	0.50	edge-on
HMDS-treated Au	4.28	1.36	-0.50	lying flat
Bare Au	3.35	1.64	0.49	edge-on

Table 6.1 compares the work functions, the highest occupied molecular orbital (HOMO) levels, the DRs extracted from NEXAFS, and the molecular orientation of pentacene and DHT-ANT on the different substrates. We observe a strong correlation between the work functions and the ensemble-average molecular orientation of both pentacene and DHT-ANT. Specifically, both pentacene and DHT-ANT adopting the "lying flat" orientation exhibit higher work functions than those of films with the "upright" or the "edge-on" orientation. These observations suggest that changes in molecular orientation in organic semiconductor thin films have significant impact on the electronic band structures of the materials.

There is, however, a possibility that changes in the work function may be a result of molecular-level shifts due to band bending at the molecule/substrate interface rather than due to difference in the molecular orientation.[15, 16] To exclude this possibility, we investigated the energetic positions of the valence levels (e.g. HOMO levels) and the C1s core level shifts in the x-ray photoelectron spectroscopy (XPS) spectra taken on the same samples that underwent UPS studies.[16, 43] Specifically, if changes in the work function are correlated with changes in the HOMO levels or in the C1s core level, the changes in work functions is likely caused by molecular-levels shifts.[16] If not, we can conclude the work functions are altered by the change in the molecular orientation of the organic semiconductors.

We have included the HOMO levels for all the cases in Table 6.1. While the work functions of these films vary depending on the molecular orientation, the HOMO levels of these films appear to be the same with a variation that is less than 0.09eV, suggesting that changes in the work function of pentacene (and DHT-ANT) are a result of changes in the molecular structure. This is also supported by the measured C1s core energy levels, which only shifted by 0.1 to 0.3eV across each set of data (not shown here). These shifts are not correlated with changes in the work functions either. The core level data thus supports the proposal that increases in the work functions are likely to attribute to the “lying flat” orientation in pentacene films deposited on the HMDS-treated and the bare gold.

As in the case of pentacene, neither the HOMO levels nor the C1s positions (not shown here) correlate with changes in the work functions in DHT-ANT films. This also suggests that the work function change for DHT-ANT film on HMDS-treated gold is a result of the "lying flat" orientation in DHT-ANT. Considering that the organic semiconductor films are relatively thick, it should be emphasized that the electronic structures we have probed are not interface effects, but more bulk effects, which are correlated with the molecular structure as previously described.

We have reported a direct correlation of the structure and the work functions of two small-molecule organic semiconductors, i.e. pentacene and DHT-ANT. Specifically, the organic semiconductor thin films having the "lying flat" orientation adopts a feather-like or rod-like morphology and exhibits higher work functions. We have also shown that molecular orientation is greatly influenced by molecule-substrate interactions. On gold, controlling the molecular orientation is possible through the modification of the surface chemistry.

FIGURES

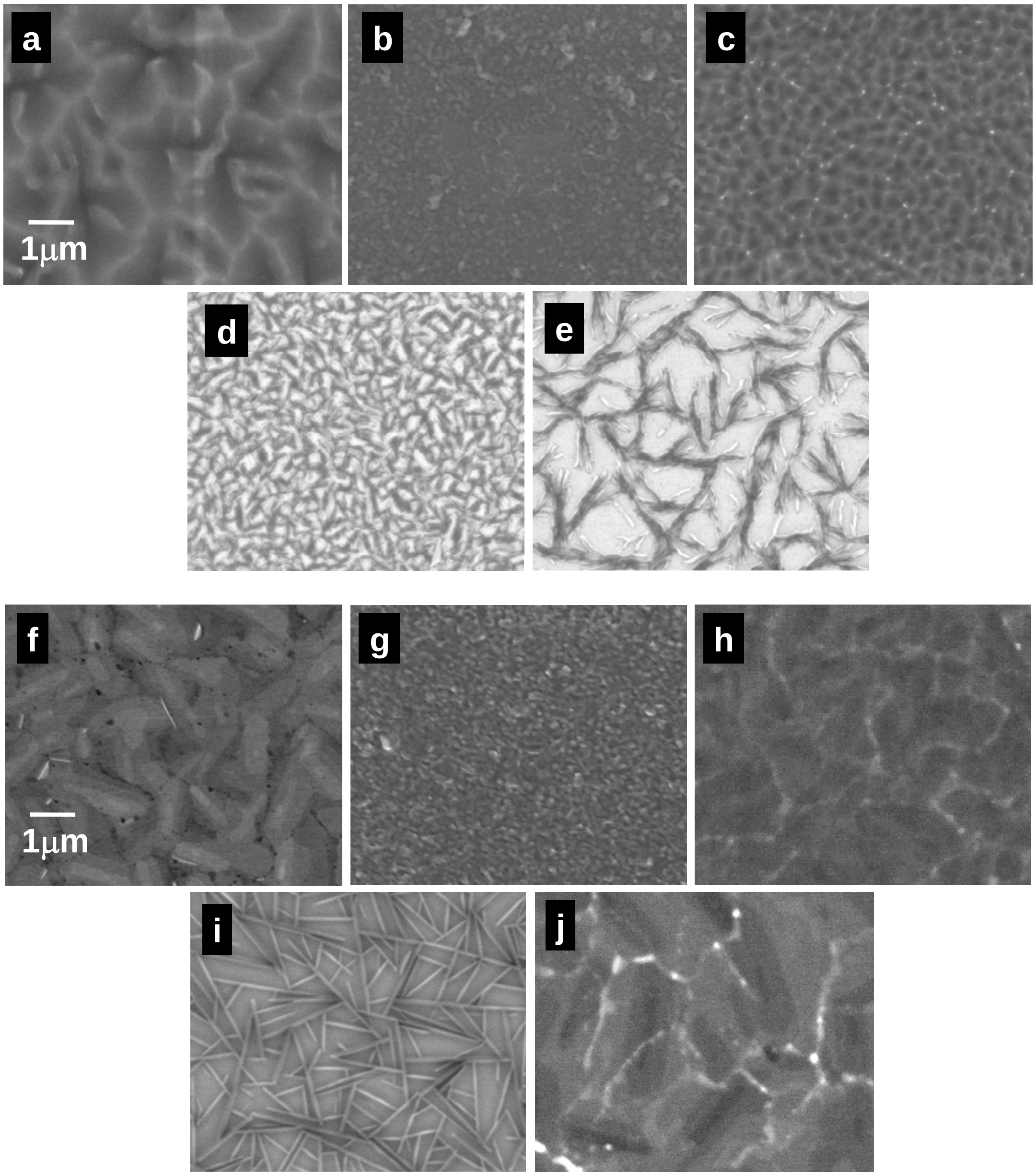

Figure 6.1. SEM images of pentacene thin films on (a) HMDS-treated Si, (b) PANI-PAAMPSA-coated Si, (c) solvent-cleaned gold, (d) HMDS-treated gold, and (e) bare gold; DHT-ANT thin films on (f) HMDS-treated Si, (g) PANI-PAAMPSA-coated Si, (h) solvent-cleaned gold, (i) HMDS-treated gold, and (j) bare gold. All the images are on the same scale.

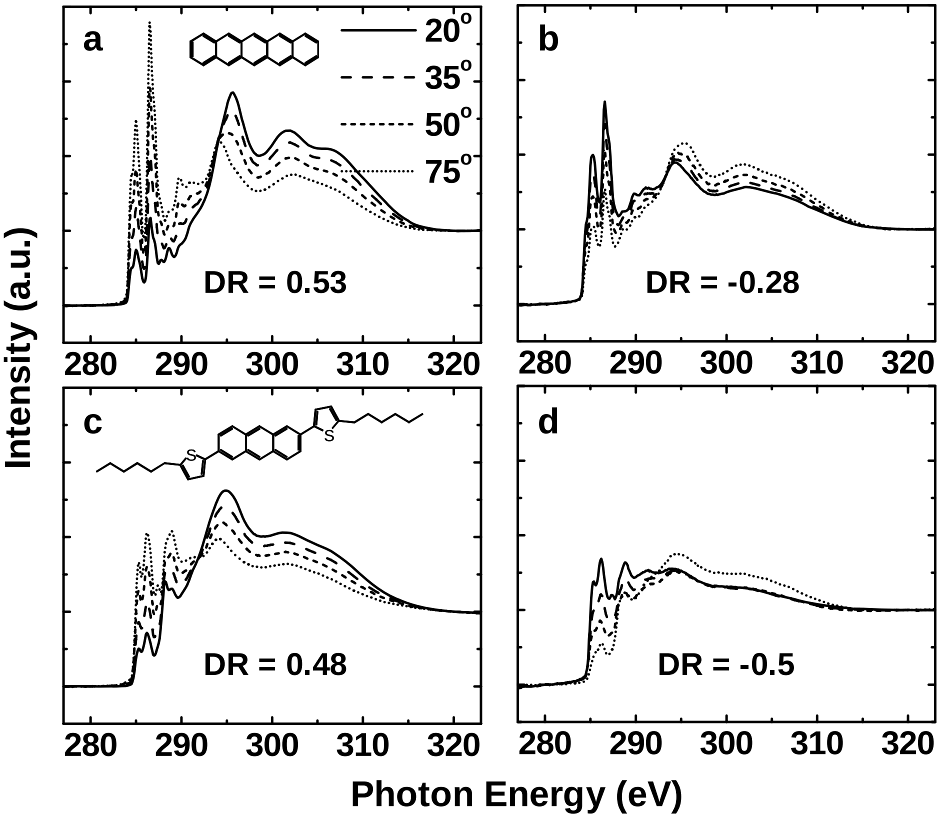

Figure 6.2. Pre- and post-edge normalized carbon-edge NEXAFS spectra as a function of increasing x-ray incident angle of pentacene on (a) HMDS-treated Si and (b) HMDS-treated gold, and those of DHT-ANT on (c) HMDS-treated Si and (d) HMDS-treated gold. Dichroic ratios derived from each set of spectra are included. The chemical structures of pentacene and DHT-ANT are shown as insets in (a) and (c), respectively.

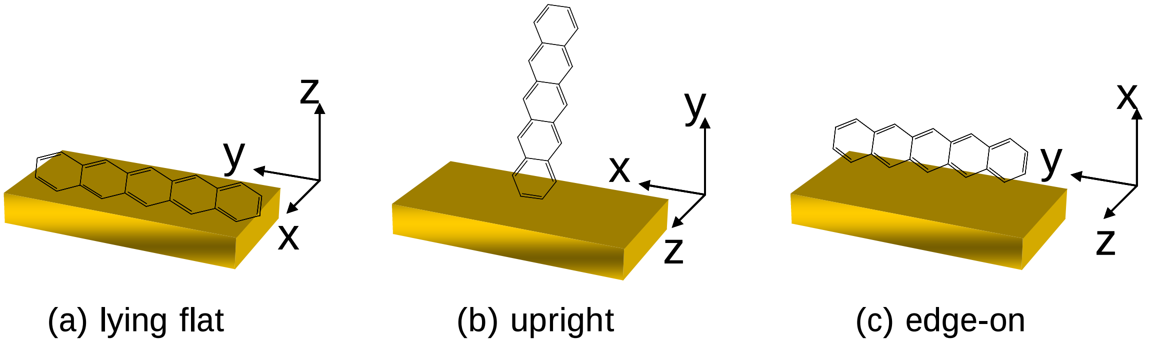

(a) lying flat (b) upright (c) edge-on

Figure 6.3. Three orientations the organic semiconductors of interest can adopt. These orientations are illustrated with pentacene. A coordinate system in which the ***x***-axis is aligned with the long molecular axis of the fused rings, the ***y***-axis along the short molecular axis of the fused rings, and the ***z***-axis is perpendicular to the ring plane is used. (a) pentacene lying flat where the ***x***- and ***y***-axes are parallel to the surface and the ***z***-axis is perpendicular to the surface, (b) pentacene oriented upright in which the ***z***- and ***x***-axes are parallel to the surface and the ***y***-axis is perpendicular to the surface, and (c) pentacene oriented edge-on where the ***y***- and ***z***-axes are parallel to the surface and the ***x***-axis is perpendicular to the surface.

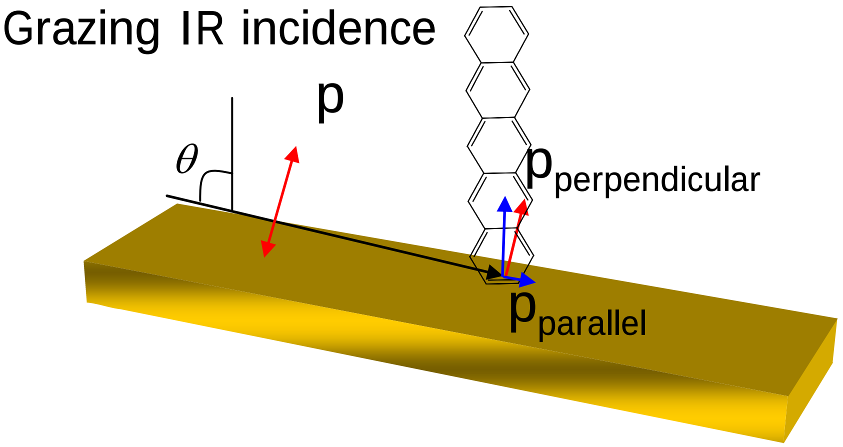

Figure 6.4. Scheme of RAIRS. Grazing IR incidence (80° away from the surface normal) impinges on pentacene. The parallel component of the p-polarized light is nulled due to its interactions with free electrons on the gold surface. Only the perpendicular component of the p-polarized light interacts with the transitional dipole moments of pentacene.

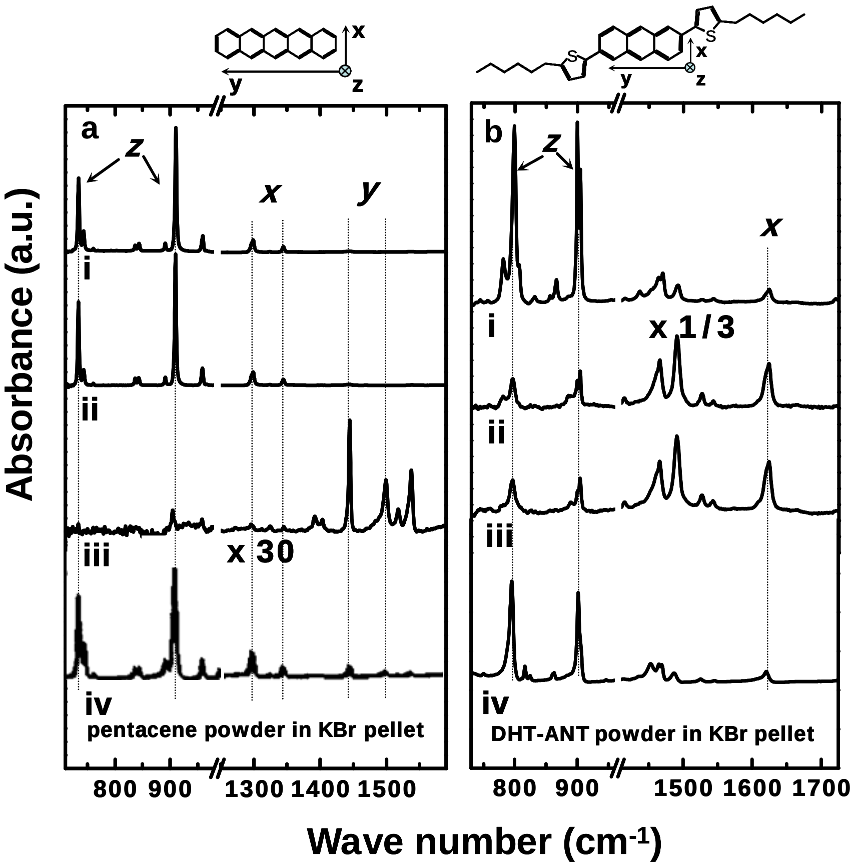

Figure 6.5. RAIRS spectra of (a) pentacene and (b) DHT-ANT on (i) HMDS-treated gold, (ii) bare gold (iii) solvent-cleaned gold, and (iv) transmission IR spectrum of pentacene powder dispersed in a KBr pellet[32]. (a)-iii and (b)-i are multiplied by 30 and 1/3 for clarity. The chemical structures of pentacene and DHT-ANT with the corresponding coordinate systems for their transitional dipole moments are shown on top of (a) and (b), respectively. The ***x***-, and ***y***-axis are aligned to the short and long molecule axis. The ***z*** axis is normal to the ring plane of the molecules.

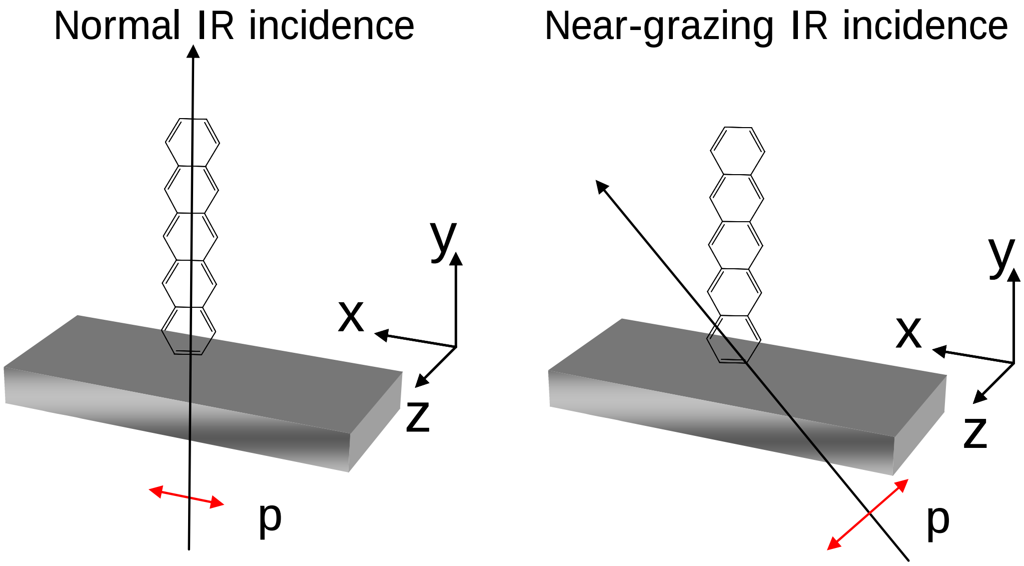

Figure 6.6. Transmission IR with p-polarized IR light experimental setup. When normal IR incidence (0° away from the surface normal) is used, p-polarized light is sensitive to the vibrations of pentacene whose transitional dipole moments are parallel to the surface. When a near-grazing IR incidence (68° away from the surface normal) is used, p-polarized light is sensitive to the vibrations of pentacene whose transitional dipole moments are normal to the surface.

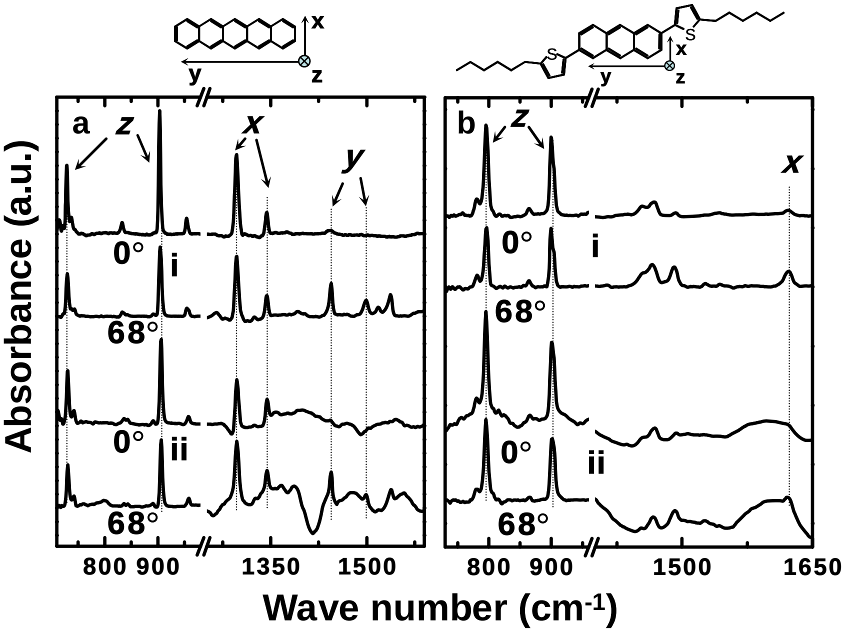

Figure 6.7. Transmission IR spectra of (a) pentacene and (b) DHT-ANT on (a) HMDS-treated Si and (b) PANI-PAAMPSA-coated Si surfaces. The spectra were collected at (i) 0° and (ii) 68° away from substrate normal using p-polarized light. The chemical structures of pentacene and DHT-ANT with the corresponding coordinate systems for their transitional dipole moments are shown on top of (a) and (b), respectively.

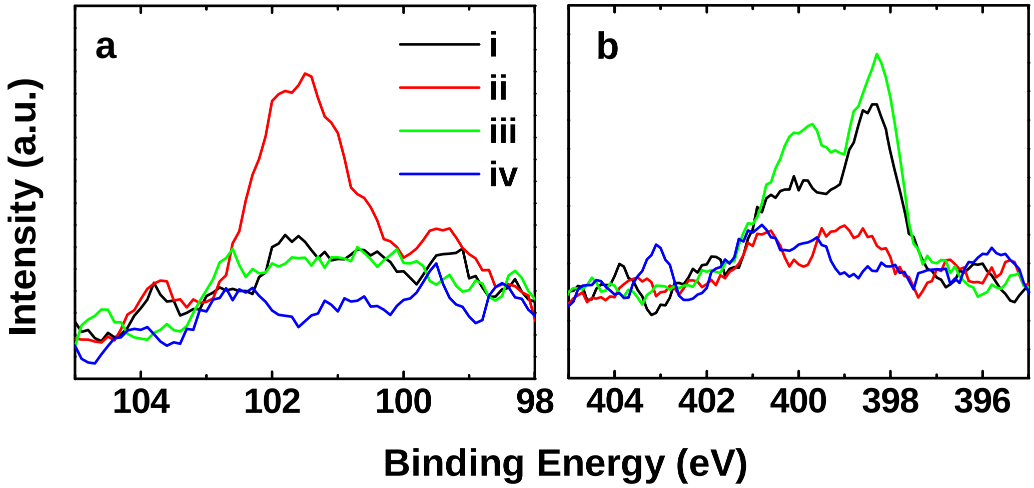

Figure 6.8. XPS collected in the (a) silicon and the (b) nitrogen regions of (i) solvent-cleaned gold, (ii) HMDS-treated gold, (iii) HMDS-treated gold followed by solvent-cleaning, and (iv) bare gold. Each spectrum was baseline-subtracted using a Shirley background and was then smoothed using the boxcar routine with seven points.

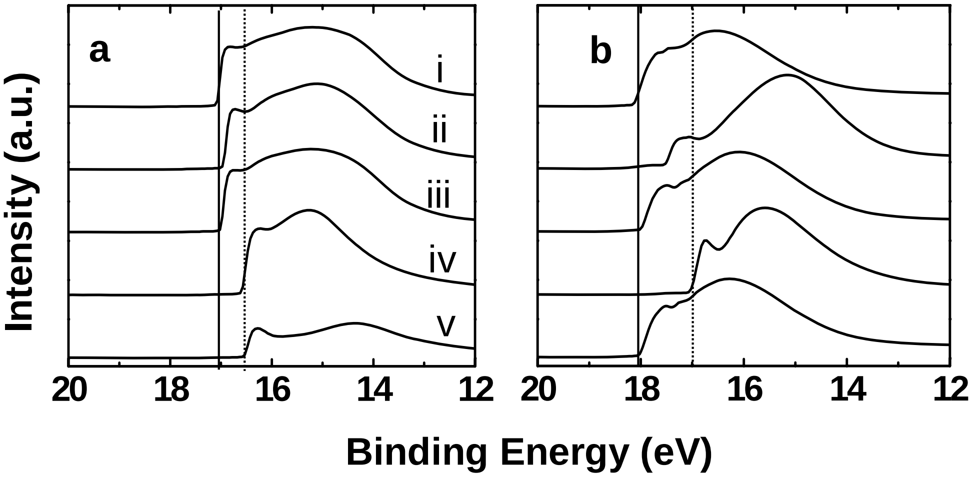

Figure 6.9. UPS spectra of (a) 50nm of pentacene and (b) 40nm of DHT-ANT on (i) HMDS-treated Si, (ii) PANI-PAAMPSA-coated Si, (iii) solvent-cleaned gold, (iv) HMDS-treated gold, and (v) bare gold. The solid and dashed lines indicate the vacuum cut-offs for the respective thin films on HMDS-treated Si and HMDS-gold, respectively.

REFERENCES

1. D. J. Gundlach, Y. Y. Lin, T. N. Jackson, S. F. Nelson, D. G. Schlom, *IEEE Electron Device Letters* **1997**, *18*, 87.

2. R. Ye, M. Baba, Y. Ohishi, K. Mori, K. Suzuki, *Molecular Crystals and Liquid Crystals* **2003**, *407*, 543.

3. X. L. Chen, A. J. Lovinger, Z. Bao, J. Sapjeta, *Chemistry of Materials* **2001**, *13*, 1341.

4. J. Chen, D. C. Martin, J. E. Anthony, *Journal of Materials Research* **2007**, *22*, 1701.

5. K. S. Lee, T. J. Smith, K. C. Dickey, J. E. Yoo, K. J. Stevenson, Y.-L. Loo, *Advanced Functional Materials* **2006**, *16*, 2409.

6. H. Sirringhaus, P. J. Brown, R. H. Friend, M. M. Nielsen, K. Bechgaard, B. M. W. Langeveld-Voss, A. J. H. Spiering, R. A. J. Janssen, E. W. Meijer, P. Herwig, D. M. De Leeuw, *Nature (London)* **1999**, *401*, 685.

7. D. M. DeLongchamp, S. Sambasivan, D. A. Fischer, E. K. Lin, P. Chang, A. R. Murphy, J. M. J. Frechet, V. Subramanian, *Advanced Materials* **2005**, *17*, 2340.

8. S. M. Sze, *Physics of Semiconductor Devices*, John Wiley & Sons, Inc., New York **1981**.

9. W. Chen, M. Dumas, D. Mao, A. Kahn, *Journal of Vacuum Science & Technology B* **1992**, *10*, 1886.

10. R. Duszak, C. J. Palmstrom, L. T. Florez, Y. N. Yang, J. H. Weaver, *Journal of Vacuum Science & Technology B* **1992**, *10*, 1891.

11. C. J. Palmstrom, T. L. Cheeks, H. L. Gilchrist, J. G. Zhu, C. B. Carter, B. J. Wilkens, R. Martin, *Journal of Vacuum Science & Technology a-Vacuum Surfaces and Films* **1992**, *10*, 1946.

12. W. S. Hu, Y. T. Tao, Y. J. Hsu, D. H. Wei, Y. S. Wu, *Langmuir* **2005**, *21*, 2260.

13. D. Kafer, L. Ruppel, G. Witte, *Physical Review B: Condensed Matter and Materials Physics* **2007**, *75*, 085309/1.

14. S. Lukas, S. Soehnchen, G. Witte, C. Woell, *ChemPhysChem* **2004**, *5*, 266.

15. H. Ishii, K. Sugiyama, E. Ito, K. Seki, *Advanced Materials (Weinheim, Germany)* **1999**, *11*, 605.

16. I. G. Hill, A. Rajagopal, A. Kahn, Y. Hu, *Applied Physics Letters* **1998**, *73*, 662.

17. N. Koch, A. Elschner, J. Schwartz, A. Kahn, *Applied Physics Letters* **2003**, *82*, 2281.

18. H. Meng, F. Sun, M. B. Goldfinger, G. D. Jaycox, Z. Li, W. J. Marshall, G. S. Blackman, *Journal of the American Chemical Society* **2005**, *127*, 2406.

19. R. Ruiz, D. Choudhary, B. Nickel, T. Toccoli, K.-C. Chang, A. C. Mayer, P. Clancy, J. M. Blakely, R. L. Headrick, S. Iannotta, G. G. Malliaras, *Chemistry of Materials* **2004**, *16*, 4497.

20. F. Heringdorf, M. C. Reuter, R. M. Tromp, *Nature* **2001**, *412*, 517.

21. H. Yang, T. J. Shin, M.-M. Ling, K. Cho, C. Y. Ryu, Z. Bao, *Journal of the American Chemical Society* **2005**, *127*, 11542.

22. I. Yagi, K. Tsukagoshi, Y. Aoyagi, *Applied Physics Letters* **2005**, *86*.

23. A. S. Killampalli, J. R. Engstrom, *Applied Physics Letters* **2006**, *88*.

24. J. Stohr, *NEXAFS Spectroscopy*, Springer, Berlin **1992**.

25. J. Stohr, D. A. Outka, *Physical Review B: Condensed Matter and Materials Physics* **1987**, *36*, 7891.

26. S. Sohnchen, S. Lukas, G. Witte, *Journal of Chemical Physics* **2004**, *121*, 525.

27. S. Banerjee, T. Hemraj-Benny, S. Sambasivan, D. A. Fischer, J. A. Misewich, S. S. Wong, *J. Phys. Chem. B* **2005**, *109*, 8489.

28. D. A. Krapchetov, H. Ma, A. K. Y. Jen, D. A. Fischer, Y.-L. Loo, *Langmuir* **2005**, *21*, 5887.

29. H. dAgren, O. Vahtras, V. Carravetta, *Chemical Physics* **1995**, *196*, 47.

30. D. Kaefer, G. Witte, P. Cyganik, A. Terfort, C. Woell, *Journal of the American Chemical Society* **2006**, *128*, 1723.

31. A. N. Parikh, D. L. Allara, *Journal of Chemical Physics* **1992**, *96*, 927.

32. D. Ross, R. Aroca, *Journal of Chemical Physics* **2002**, *117*, 8095.

33. N. B. Colthup, L. H. Daly, S. E. Wiberley, *Infrared and Raman spectroscopy*, Academic Press, Boston, MA **1990**.

34. D. A. Krapchetov, H. Ma, A. K. Y. Jen, D. A. Fischer, Y. L. Loo, *Langmuir* **2006**, *22*, 9491.

35. B. de Boer, H. Meng, D. F. Perepichka, J. Zheng, M. M. Frank, Y. J. Chabal, Z. Bao, *Langmuir* **2003**, *19*, 4272.

36. J. G. Radziszewski, J. Michl, *Journal of Chemical Physics* **1985**, *82*, 3527.

37. B. Liedberg, Z. Yang, I. Engquist, M. Wirde, U. Gelius, G. Gotz, P. Bauerle, R. M. Rummel, C. Ziegler, W. Gopel, *Journal of Physical Chemistry B* **1997**, *101*, 5951.

38. V. P. Tolstoy, I. V. Chernyshova, V. A. Skryshevsky, *Handbook of Infrared Spectroscopy of Ultrathin Films*, John Wiley & Sons, Inc., **2003**.

39. O. McDonald, A. A. Cafolla, D. Carty, G. Sheerin, G. Hughes, *Surface Science* **2006**, *600*, 3217.

40. P. G. Schroeder, C. B. France, J. B. Park, B. A. Parkinson, *Journal of Physical Chemistry B* **2003**, *107*, 2253.

41. J. H. Kang, X. Y. Zhu, *Applied Physics Letters* **2003**, *82*, 3248.

42. D. Cahen, A. Kahn, *Advanced Materials* **2003**, *15*, 271.

43. *private discussion with Prof. Antoine Kahn*.

Chapter 7. Conclusions and Future work

CONCLUSIONS

This thesis focuses on the processing-structure-property relationships of a water-dispersible, conducting polymer, polyaniline that is doped with poly(2-acryl-amido-2-methyl-1-propanesulfonic acid), PANI-PAAMPSA. The overall goal of this thesis was to understand how such relationships facilitate the incorporation of PANI-PAAMPSA into functional organic thin-film transistors (TFTs). This goal was achieved through the examination of several aspects of PANI-PAAMPSA: (1) the development of simple patterning techniques of the deposition of PANI-PAAMPSA features on insulating substrates, (2) the assessment of the compatibility of PANI-PAAMPSA with organic semiconductors in TFTs, (3) the improvement of conductivity of PANI-PAAMPSA, and (4) the understanding of the molecular structure-property relationships of organic semiconductors deposited on PANI-PAAMPSA as well as on other substrates.

We have developed simple patterning techniques for depositing PANI-PAAMPSA on insulating by exploiting its wetting and adsorption characteristics. Specifically, conductive PANI-PAAMPSA features can be directly patterned in the hydrophilic regions on a molecular template. The ability to direct pattern PANI-PAAMPSA post-synthesis allows us the opportunity to independently elucidate the structure-property relationships of PANI-PAAMPSA. Because our patterning techniques enable the direct patterning of PANI-PAAMPSA on insulating substrates, PANI-PAAMPSA features can be used as functional electrical components immediately after patterning without subsequent transfer to avoid lateral electrical shortage between individual features. PANI-PAAMPSA features as small as 5μm can be routinely created with average electrical conductivities of 0.2S/cm.

Having developed patterning techniques for PANI-PAAMPSA, we assessed the functionality of PANI-PAAMPSA as source and drain electrodes in bottom-contact pentacene thin-film transistors (TFTs). We found that PANI-PAAMPSA performs effectively as functional contacts to the pentacene active layer. The device performance is shown to vary by approximately an order of magnitude depending on the details with which the molecular template is created. This phenomenon is attributed to the surface roughness of the molecular template in the channel region on which pentacene is deposited. With a smooth molecular template (root mean square roughness, r.m.s=0.2nm), we have achieved bottom-contact pentacene TFTs with PANI-PAAMPSA electrodes that exhibit an average mobility of 0.2cm^2/V-s.[1]

We found that the pentacene/PANI-PAAMPSA interface is less resistive than the pentacene/gold interface in bottom-contact devices. We showed that the structure of pentacene at the channel/electrode interface is directly related to its reduced contact resistance. The morphology and molecular orientation of the pentacene thin film are more favorable for charge injection and extraction when deposited on PANI-PAAMPSA compared to when it is deposited on gold.

The conductivity of PANI-PAAMPSA can be improved by more than two orders of magnitude via a simple solvent treatment. These conductivity improvements are results of drastic changes in the chain conformation of PANI-PAAMPSA. The chain conformation of PANI-PAAMPSA is governed by strong ionic interactions between

PANI and PAAMPSA. With an acid solvent, e.g., dichloroacetic acid (DCA), the ionic interactions can be moderated. PANI-PAAMPSA chains are rearranged from the “compact-coil” to the “extended chain” conformation with exposure to dichloroacetic acid. Efficient charge transport is enabled through the “extended chain” PANI-PAAMPSA conformation. The improvement of PANI-PAAMPSA conductivity is crucial to expand the functionality of PANI-PAAMSA as interconnects and wires for TFT applications. We demonstrated the performance (mobility and on/off ratios) of TFTs utilizing functionalized acene derivatives as active layers and showed that their mobility can be improved by more than an order of magnitude using DCA-treated PANI-PAAMPSA source and drain electrodes.

The details of processing conditions can dramatically affect the morphology and molecular orientation of vacuum-deposited organic semiconductors, e.g., pentacene and dihexylthiophene anthracene (DHT-ANT). Controlling the morphology and molecular orientation of these two molecules is shown to be possible by modifying the surface chemistry of substrates. This process in turn allows us to influence the work functions of these materials. We have thus established a direct correlation between the morphology, molecular orientation, and work function of pentacene and DHT-ANT. Such relationships are essential for establishing designs rules and guidelines for organic electronic materials and devices.

During the last decade, many aspects of organic electronic materials and devices have seen significant progress. As a result, we may witness the full commercialization of low-cost, large area, flexible devices in the near future. For example, Plastic Logic in the U.K. announced earlier this year that it raised $100 million to build the first factory to manufacture flexible active-matrix display modules for “take anywhere, read anywhere” electronic reader products in a commercial scale.[2] For more organic electronic devices to be commercialized in real electronic markets, it will be crucial to further elucidate the processing-structure-property relationships of organic and polymer electronic materials.

FUTURE WORK

We have shown that PAAMPSA can have a significant effect on the materials properties of PANI-PAAMSPA. The surface wetting and adsorption characteristics of PANI-PAAMPSA are solely derived from PAAMPSA. The electrical conductivity of PANI-PAAMPSA is shown to increase by more than an order of magnitude by decreasing the molecular weight of PAAMPSA[3] and its molecular weight distribution[4]. Yet, this phenomenon is not understood. The elucidation of how PAAMPSA influences PANI-PAAMPSA conductivity will be crucial for its further development. Additionally, work should be carried out to examine how other modification of PAAMPSA can influence PANI-PAAMPSA conductivity. Such modifications are not limited to the manipulation of the structure of PAAMPSA, but involve the addition of extra functionalities through the incorporation of PAAMPSA in block copolymers. Our group has demonstrated that block copolymer containing PAAMPSA with narrow molecular weight distribution can be made by atom-transfer radical polymerization.[5-8] The use of PAAMPSA containing block copolymers will provide us the opportunities to determine how various functional blocks affect the molecular conformation of PANI that is template-synthesized with PAAMPSA block copolymers, which in turn imparts charge transport through such materials.

Further investigation on the interfaces between PANI-PAAMPSA and solution processable organic semiconductors, e.g., triisopropylsilyl pentacene (TIPS-pentacene)[9] and difluoro-triethylsilylethynyl anthradithiophene (FTES-ADT) is recommended. These materials are particularly important to realize low-cost electronics by solution deposition techniques. Bottom-contact TIPS-pentacene and FTES-ADT devices with PANI-PAAMPSA (or even with DCA-treated PANI-PAAMPSA), however, exhibit contact-limited performance. As a result, further examination to elucidate the origins of poor electrical contacts between PANI-PAAMPSA and solution-processable organic semiconductors is needed. Efforts should be made to enhance the electrical contact to further device performance.

REFERENCES

1. K. S. Lee, G. B. Blanchet, F. Gao, Y.-L. Loo, Applied Physics Letters 2005, 86, 074102.

2. www.plasticlogic.com.

3. J. E. Yoo, J. L. Cross, T. L. Bucholz, K. S. Lee, M. P. Espe, Y.-L. Loo, Journal of Materials Chemistry 2007, 17, 1268.

4. J. E. Yoo, T. L. Bucholz, Y.-L. Loo, Unpublished results 2007.

5. K. Matyjaszewski, J. H. Xia, Chemical Reviews 2001, 101, 2921.

6. K. B. Guice, Y. L. Loo, Macromolecules 2006, 39, 2474.

7. R. L. Teoh, K. B. Guice, Y. L. Loo, Macromolecules 2006, 39, 8609.

8. T. L. Bucholz, Y. L. Loo, Macromolecules 2006, 39, 6075.

9. M. M. Payne, S. R. Parkin, J. E. Anthony, C.-C. Kuo, T. N. Jackson, Journal of the American Chemical Society 2005, 127, 4986.

References

Adams, P. N., P. Devasagayam, et al. (1998). "A new acid-processing route to polyaniline films which exhibit metallic conductivity and electrical transport strongly dependent upon intrachain molecular dynamics." Journal of Physics-Condensed Matter **10**(37): 8293-8303.

Alam, M. A., A. Dodabalapur, et al. (1997). "A two-dimensional simulation of organic transistors." Ieee Transactions on Electron Devices **44**(8): 1332-1337.

Angelopoulos, M. (2001). "Conducting polymers in microelectronics." IBM Journal of Research and Development **45**(1): 57-75.

Angelopoulos, M. and N. Patel (1994). "Conducting polymers in microelectronic applications." Polymeric Materials Science and Engineering **71**: 222-223.

Anthony, J. E. (2006). "Functionalized acenes and heteroacenes for organic electronics." Chemical Reviews **106**(12): 5028-5048.

Banerjee, S., T. Hemraj-Benny, et al. (2005). "Near-Edge X-ray Absorption Fine Structure Investigations of Order in Carbon Nanotube-Based Systems." J. Phys. Chem. B **109**(17): 8489-8495.

Bao, Z. N. (2000). "Materials and fabrication needs for low-cost organic transistor circuits." Advanced Materials **12**(3): 227-230.

Baude, P. F., D. A. Ender, et al. (2003). "Pentacene-based radio-frequency identification circuitry." Applied Physics Letters **82**(22): 3964-3966.

Blanchet, G. B., C. R. Fincher, et al. (2004). "Contact resistance in organic thin film transistors." Applied Physics Letters **84**(2): 296-298.

Blanchet, G. B., Y.-L. Loo, et al. (2003). "Large area, high resolution, dry printing of conducting polymers for organic electronics." Applied Physics Letters **82**(3): 463-465.

Briseno, A. L., S. C. B. Mannsfeld, et al. (2006). "Patterning organic single-crystal transistor arrays." Nature **444**(7121): 913-917.

Bucholz, T. L. and Y. L. Loo (2006). "Phase behavior of near-monodisperse semifluorinated diblock copolymers by atom transfer radical polymerization." Macromolecules **39**(18): 6075-6080.

Burgi, L., T. J. Richards, et al. (2003). "Close look at charge carrier injection in polymer field-effect transistors." Journal of Applied Physics **94**(9): 6129-6137.

Burgi, L., H. Sirringhaus, et al. (2002). "Noncontact potentiometry of polymer field-effect transistors." Applied Physics Letters **80**(16): 2913-2915.

Cahen, D. and A. Kahn (2003). "Electron energetics at surfaces and interfaces: Concepts and experiments." Advanced Materials **15**(4): 271-277.

Cao, Y., J. Qiu, et al. (1995). "Effect of solvents and co-solvents on the processibility of polyaniline: I. Solubility and conductivity studies." Synthetic Metals **69**(1-3): 187-190.

Cao, Y., P. Smith, et al. (1992). "Counter-ion induced processibility of conducting polyaniline and of conducting polyblends of polyaniline in bulk polymers." Synthetic Metals **48**(1): 91-97.

Caramyshev, A. V., E. G. Evtushenko, et al. (2005). "Synthesis of conducting polyelectrolyte complexes of polyaniline and poly(2-acrylamido-3-methyl-1-propanesulfonic acid) catalyzed by pH-stable palm tree peroxidase." Biomacromolecules **6**(3): 1360-1366.

Chen, J., D. C. Martin, et al. (2007). "Morphology and molecular orientation of thin-film bis(triisopropylsilylethynyl) pentacene." Journal of Materials Research **22**(6): 1701-1709.

Chen, W., M. Dumas, et al. (1992). "Work Function, Electron-Affinity, and Band Bending at Decapped Gaas(100) Surfaces." Journal of Vacuum Science & Technology B **10**(4): 1886-1890.

Chen, X. L., A. J. Lovinger, et al. (2001). "Morphological and Transistor Studies of Organic Molecular Semiconductors with Anisotropic Electrical Characteristics." Chemistry of Materials **13**(4): 1341-1348.

Chiang, J. C. and A. G. Macdiarmid (1986). "Polyaniline - Protonic Acid Doping of the Emeraldine Form to the Metallic Regime." Synthetic Metals **13**(1-3): 193-205.

Collard, D. M. and C. N. Sayre (1997). "Micron-scale patterning of conjugated polymers on microcontact printed patterns of self-assembled monolayers." Synthetic Metals **84**(1-3): 329-332.

Colthup, N. B., L. H. Daly, et al. (1990). Infrared and Raman spectroscopy. Boston, MA, Academic Press.

Crone, B. K., A. Dodabalapur, et al. (2002). "Organic oscillator and adaptive amplifier circuits for chemical vapor sensing." Journal of Applied Physics **91**(12): 10140-10146.

dAgren, H., O. Vahtras, et al. (1995). "Near-edge core photoabsorption in polyacenes: model molecules for graphite." Chemical Physics **196**(1,2): 47-58.

de Boer, B., H. Meng, et al. (2003). "Synthesis and Characterization of Conjugated Mono- and Dithiol Oligomers and Characterization of Their Self-Assembled Monolayers." Langmuir **19**(10): 4272-4284.

DeLongchamp, D. M., E. K. Lin, et al. (2005). "Organic semiconductor structure and chemistry from near-edge X-ray absorption fine structure (NEXAFS) spectroscopy." Proceedings of SPIE-The International Society for Optical Engineering **5940**: 54-64.

DeLongchamp, D. M., S. Sambasivan, et al. (2005). "Direct correlation of organic semiconductor film structure to field-effect mobility." Advanced Materials **17**(19): 2340-2344.

Dickey, K. C., J. E. Anthony, et al. (2006). "Improving organic thin-film transistor performance through solvent-vapor annealing of solution-processable triethylsilylethynyl anthradithiophene." Advanced Materials (Weinheim, Germany) **18**(13): 1721-1726.

Dickey, K. C., S. Subramanian, et al. (2007). "Large-area patterning of a solution-processable organic semiconductor to reduce parasitic leakage and off currents in thin-film transistors." Applied Physics Letters **90**(24): 244103/1-244103/3.

Dimitrakopoulos, C. D. and P. R. L. Malenfant (2002). "Organic thin film transistors for large area electronics." Advanced Materials **14**(2): 99-117.

Drury, C. J., C. M. J. Mutsaers, et al. (1998). "Low-cost all-polymer integrated circuits." Applied Physics Letters **73**(1): 108-110.

Duszak, R., C. J. Palmstrom, et al. (1992). "Dramatic Work Function Variations of Molecular-Beam Epitaxially Grown Gaas(100) Surfaces." Journal of Vacuum Science & Technology B **10**(4): 1891-1897.

Erdemi, H., A. Bozkurt, et al. (2004). "PAMPSA-IM based proton conducting polymer electrolytes." Synthetic Metals **143**(1): 133-138.

Fessenden, R. J. and J. S. Fessenden (1994). Organic chemistry. Pacific Grove, CA, Brooks/Cole.

Fischer, D. A. and B. M. DeKoven (1996). "Dow/NIST Materials Characterizaion Facility at U7A." November 1996 NSLS Newsletter.

Forrest, S. R. (2004). "The path to ubiquitous and low-cost organic electronic appliances on plastic." Nature **428**(6986): 911-918.

Gelinck, G. H., H. E. A. Huitema, et al. (2004). "Flexible active-matrix displays and shift registers based on solution-processed organic transistors." Nature Materials **3**(2): 106-110.

Greczynski, G., T. Kugler, et al. (1999). "Characterization of the PEDOT-PSS system by means of X-ray and ultraviolet photoelectron spectroscopy." Thin Solid Films **354**(1,2): 129-135.

Guice, K. B. and Y. L. Loo (2006). "Azeotropic atom transfer radical polymerization of hydroxyethyl methacrylate and (dimethylamino)ethyl methacrylate statistical copolymers and block copolymers with polystyrene." Macromolecules **39**(7): 2474-2480.

Gundlach, D. J., Y. Y. Lin, et al. (1997). "Pentacene organic thin-film transistors - molecular ordering and mobility." IEEE Electron Device Letters **18**(3): 87-89.

Halik, M., H. Klauk, et al. (2002). "Polymer gate dielectric and conducting-polymer contacts for high-performance organic thin-film transistors." Advanced Materials **14**(23): 1717-1722.

Hatchett, D. W., M. Josowicz, et al. (1999). "Acid doping of polyaniline: Spectroscopic and electrochemical studies." Journal of Physical Chemistry B **103**(50): 10992-10998.

Heeger, A. J. (2001). "Semiconducting and metallic polymers: The fourth generation of polymeric materials (Nobel lecture)." Angewandte Chemie-International Edition **40**(14): 2591-2611.

Heringdorf, F., M. C. Reuter, et al. (2001). "Growth dynamics of pentacene thin films." Nature **412**(6846): 517-520.

Hill, I. G., A. Rajagopal, et al. (1998). "Molecular level alignment at organic semiconductor-metal interfaces." Applied Physics Letters **73**(5): 662-664.

Hopkins, A. R., P. G. Rasmussen, et al. (1998). "Investigation of ordering in polyaniline salt films prepared from hexafluoroisopropanol solutions." Synthetic Metals **97**(1): 47-51.

Horowitz, G. (1998). "Organic field-effect transistors." Advanced Materials (Weinheim, Germany) **10**(5): 365-377.

Hu, W. S., Y. T. Tao, et al. (2005). "Molecular Orientation of Evaporated Pentacene Films on Gold: Alignment Effect of Self-Assembled Monolayer." Langmuir **21**(6): 2260-2266.

Huang, Z., P.-C. Wang, et al. (1997). "Selective Deposition of Conducting Polymers on Hydroxyl-Terminated Surfaces with Printed Monolayers of Alkylsiloxanes as Templates." Langmuir **13**(24): 6480-6484.

Hundley, M. F., P. N. Adams, et al. (2002). "The influence of 2-acrylamido-2-methyl-1-propanesulfonic acid (AMPSA) additive concentration and stretch orientation on electronic transport in AMPSA-modified polyaniline films prepared from an acid solvent mixture." Synthetic Metals **129**(3): 291-297.

Ishii, H., K. Sugiyama, et al. (1999). "Energy level alignment and interfacial electronic structures at organic/metal and organic/organic interfaces." Advanced Materials (Weinheim, Germany) **11**(8): 605-625.

Jacobs, H. O., H. F. Knapp, et al. (1999). "Practical aspects of Kelvin probe force microscopy." Review of Scientific Instruments **70**(3): 1756-1760.

Janata, J. and M. Josowicz (2003). "Conducting polymers in electronic chemical sensors." Nature Materials **2**(1): 19-24.

Jeon, N. L., K. Finnie, et al. (1997). "Structure and Stability of Patterned Self-Assembled Films of Octadecyltrichlorosilane Formed by Contact Printing." Langmuir **13**(13): 3382-3391.

Kaefer, D., G. Witte, et al. (2006). "A Comprehensive Study of Self-Assembled Monolayers of Anthracenethiol on Gold: Solvent Effects, Structure, and Stability." Journal of the American Chemical Society **128**(5): 1723-1732.

Kafer, D., L. Ruppel, et al. (2007). "Growth of pentacene on clean and modified gold surfaces." Physical Review B: Condensed Matter and Materials Physics **75**(8): 085309.

Kang, E. T., K. G. Neoh, et al. (1998). "Polyaniline: A polymer with many interesting intrinsic redox states." Progress in Polymer Science **23**(2): 277-324.

Kang, J. H. and X. Y. Zhu (2003). "Pi-stacked pentacene thin films grown on Au(111)." Applied Physics Letters **82**(19): 3248-3250.

Kelley, T. W. and C. D. Frisbie (2001). "Gate voltage dependent resistance of a single organic semiconductor grain boundary." Journal of Physical Chemistry B **105**(20): 4538-4540.

Killampalli, A. S. and J. R. Engstrom (2006). "Nucleation of pentacene thin films on silicon dioxide modified with hexamethyldisilazane." Applied Physics Letters **88**(14): 143125.

Kim, J. Y., J. H. Jung, et al. (2002). "Enhancement of electrical conductivity of poly(3,4-ethylenedioxythiophene)/poly(4-styrenesulfonate) by a change of solvents." Synthetic Metals **126**(2-3): 311-316.

Klauk, H., G. Schmid, et al. (2002). "Contact resistance in organic thin film transistors." Solid-State Electronics **47**(2): 297-301.

Knipp, D., R. A. Street, et al. (2003). "Pentacene thin-film transistors on inorganic dielectrics: morphology, structural properties, and electronic transport." Journal of Applied Physics **93**(1): 347-355.

Kobayashi, S., T. Nishikawa, et al. (2004). "Control of carrier density by self-assembled monolayers in organic field-effect transistors." Nature Materials **3**(5): 317-322.

Koch, N., A. Elschner, et al. (2003). "Organic molecular films on gold versus conducting polymer: influence of injection barrier height and morphology on current-voltage characteristics." Applied Physics Letters **82**(14): 2281-2283.

Koch, N., A. Kahn, et al. (2003). "Conjugated organic molecules on metal versus polymer electrodes. Demonstration of a key energy level alignment mechanism." Applied Physics Letters **82**(1): 70-72.

Krapchetov, D. A., H. Ma, et al. (2005). "Solvent-Dependent Assembly of Terphenyl- and Quaterphenyldithiol on Gold and Gallium Arsenide." Langmuir **21**(13): 5887-5893.

Krapchetov, D. A., H. Ma, et al. (2006). "High-sensitivity transmission IR spectroscopy for the chemical identification and structural analysis of conjugated molecules on gallium arsenide surfaces." Langmuir **22**(23): 9491-9494.

Kymissis, I., C. D. Dimitrakopoulos, et al. (2001). "High-performance bottom electrode organic thin-film transistors." IEEE Transactions on Electron Devices **48**(6): 1060-1064.

Lee, K. S., G. B. Blanchet, et al. (2005). "Direct patterning of conductive water-soluble polyaniline for thin-film organic electronics." Applied Physics Letters **86**(7): 074102.

Lee, K. S., T. J. Smith, et al. (2006). "High-Resolution Characterization of Pentacene-Polyaniline Interfaces in Thin-Film Transistors." Advanced Functional Materials **16**: 2409-2414.

Lee, W. H., D. H. Kim, et al. (2007). "Solution-processable pentacene microcrystal arrays for high performance organic field-effect transistors." Applied Physics Letters **90**(13): 132106.

Lefenfeld, M., G. Blanchet, et al. (2003). "High-performance contacts in plastic transistors and logic gates that use printed electrodes of DNNSA-PANI doped with single-walled carbon nanotubes." Advanced Materials **15**(14): 1188-1191.

Li, Z. F. and E. Ruckenstein (2002). "Patterned Conductive Polyaniline on Si(100) Surface via Self-Assembly and Graft Polymerization." Macromolecules **35**(25): 9506-9512.

Liedberg, B., Z. Yang, et al. (1997). "Self-assembly of alpha-functionalized terthiophenes on gold." Journal of Physical Chemistry B **101**(31): 5951-5962.

Lin, Y.-Y., D. J. Gundlach, et al. (1997). "Pentacene-based organic thin-film transistors." IEEE Transactions on Electron Devices **44**(8): 1325-1331.

Ling, M. M. and Z. Bao (2004). "Thin film deposition, patterning, and printing in organic thin film transistors." Chemistry of Materials **16**: 4824-4840.

Loo, Y. L. (2007). "Solution-processable organic semiconductors for thin-film transistors: Opportunities for chemical engineers." Aiche Journal **53**(5): 1066-1074.

Lukas, S., S. Soehnchen, et al. (2004). "Epitaxial growth of pentacene films on metal surfaces." ChemPhysChem **5**(2): 266-270.

MacDiarmid, A. G. (2001). ""Synthetic metals": A novel role for organic polymers (Nobel lecture)." Angewandte Chemie-International Edition **40**(14): 2581-2590.

MacDiarmid, A. G. and A. J. Epstein (1994). "The concept of secondary doping as applied to polyaniline." Synthetic Metals **65**(2-3): 103-116.

MacDiarmid, A. G. and A. J. Epstein (1995). "Secondary doping in polyaniline." Synthetic Metals **69**(1-3): 85-92.

Matyjaszewski, K. and J. H. Xia (2001). "Atom transfer radical polymerization." Chemical Reviews **101**(9): 2921-2990.

McDonald, O., A. A. Cafolla, et al. (2006). "Photoemission, NEXAFS and STM studies of pentacene thin films on Au(100)." Surface Science **600**(16): 3217-3225.

Meng, H., F. Sun, et al. (2005). "High-Performance, Stable Organic Thin-Film Field-Effect Transistors Based on Bis-5'-alkylthiophen-2'-yl-2,6-anthracene Semiconductors." Journal of the American Chemical Society **127**(8): 2406-2407.

Menon, R., C. O. Yoon, et al. (1993). "Transport in polyaniline near the critical regime of the metal-insulator transition." Physical Review B: Condensed Matter and Materials Physics **48**(24): 17685-17694.

Meyer zu Heringdorf, F. J., M. C. Reuter, et al. (2004). "The nucleation of pentacene thin films." Applied Physics A: Materials Science & Processing **78**(6): 787-791.

Moon, H., R. Zeis, et al. (2004). "Synthesis, Crystal Structure, and Transistor Performance of Tetracene Derivatives " Journal of American Chemical Society **126**: 15322-15323.

Necliudov, P. V., M. S. Shur, et al. (2002). "Contact resistance extraction in pentacene thin film transistors." Solid-State Electronics **47**(2): 259-262.

Neudeck, G. W. and A. K. Malhotra (1976). "Amorphous Silicon Thin-Film Transistor - Theory and Experiment." Solid-State Electronics **19**(8): 721-729.

Nonnenmacher, M., M. P. O'Boyle, et al. (1991). "Kevin probe force microscopy." Applied Physics Letters **58**(25): 2921-2923.

Palmstrom, C. J., T. L. Cheeks, et al. (1992). "Effect of Orientation on the Schottky-Barrier Height of Thermodynamically Stable Epitaxial Metal Gaas Structures."

Journal of Vacuum Science & Technology a-Vacuum Surfaces and Films **10**(4): 1946-1952.

Parikh, A. N. and D. L. Allara (1992). "Quantitative determination of molecular structure in multilayered thin films of biaxial and lower symmetry from photon spectroscopies. I. Reflection infrared vibrational spectroscopy." Journal of Chemical Physics **96**(2): 927-945.

Park, S. K., C.-C. Kuo, et al. (2005). "High mobility solution-processed OTFTs." Technical Digest - International Electron Devices Meeting: 113-116.

Payne, M. M., S. R. Parkin, et al. (2005). "Functionalized Higher Acenes: Hexacene and Heptacene." Journal of the American Chemical Society **127**(22): 8028-8029.

Payne, M. M., S. R. Parkin, et al. (2005). "Organic Field-Effect Transistors from Solution-Deposited Functionalized Acenes with Mobilities as High as 1 cm2/V.s." Journal of the American Chemical Society **127**(14): 4986-4987.

Pernstich, K. P., S. Haas, et al. (2004). "Threshold voltage shift in organic field effect transistors by dipole monolayers on the gate insulator." Journal of Applied Physics **96**(11): 6431-6438.

Potje-Kamloth, K., B. J. Polk, et al. (2002). "Doping of polyaniline in the solid state with photogenerated triflic acid." Chemistry of Materials **14**(6): 2782-2787.

Puntambekar, K. P., P. V. Pesavento, et al. (2003). "Surface potential profiling and contact resistance measurements on operating pentacene thin-film transistors by Kelvin probe force microscopy." Applied Physics Letters **83**(26): 5539-5541.

Qiao, J. L., T. Hamaya, et al. (2005). "New highly proton conductive polymer membranes poly(vinyl alcohol)-2-acrylamido-2-methyl-1-propanesulfonic acid (PVA-PAMPS)." Journal of Materials Chemistry **15**(41): 4414-4423.

Radziszewski, J. G. and J. Michl (1985). "Symmetry Assignment of Vibrations in Anthracene, Phenazine, and Acridine from Infrared Dichroism in Stretched Polyethylene." Journal of Chemical Physics **82**(8): 3527-3533.

Rannou, P., A. Gawlicka, et al. (1998). "Spectroscopic, structural and transport properties of conductive polyaniline processed from fluorinated alcohols." Macromolecules **31**(9): 3007-3015.

Rogers, J. A., Z. Bao, et al. (2001). "Paper-like electronic displays: large-area rubber-stamped plastic sheets of electronics and microencapsulated electrophoretic inks." Proceedings of the National Academy of Sciences of the United States of America **98**(9): 4835-4840.

Roichman, Y. and N. Tessler (2002). "Structures of polymer field-effect transistor: Experimental and numerical analyses." Applied Physics Letters **80**(1): 151-153.

Ross, D. and R. Aroca (2002). "Effective medium theories in surface enhanced infrared spectroscopy: The pentacene example." Journal of Chemical Physics **117**(17): 8095-8103.

Rotzoll, R., S. Mohapatra, et al. (2006). "Radio frequency rectifiers based on organic thin-film transistors." Applied Physics Letters **88**(12): 123502.

Rozsnyai, L. F. and M. S. Wrighton (1996). "Controlling the Adhesion of Conducting Polymer Films with Patterned Self-Assembled Monolayers." Chemistry of Materials **8**(2): 309-311.

Ruiz, R., D. Choudhary, et al. (2004). "Pentacene Thin Film Growth." Chemistry of Materials **16**(23): 4497-4508.

Sadewasser, S. and M. C. Lux-Steiner (2003). "Correct Height Measurement in Noncontact Atomic Force Microscopy." Physical Review Letters **91**(26, Pt. 1): 266101.

Salleo, A., M. L. Chabinyc, et al. (2002). "Polymer thin-film transistors with chemically modified dielectric interfaces." Applied Physics Letters **81**(23): 4383-4385.

Sayre, C. N. and D. M. Collard (1997). "Depostion of polyaniline on micro-contact printed self-assembled monolayers of w-functionalized alkanethiols." Journal of Materials Chemistry **7**: 909-912.

Schroeder, P. G., C. B. France, et al. (2003). "Orbital Alignment and Morphology of Pentacene Deposited on Au(111) and SnS2 Studied Using Photoemission Spectroscopy." Journal of Physical Chemistry B **107**(10): 2253-2261.

Sheats, J. R. (2004). "Manufacturing and commercialization issues in organic electronics." Journal of Materials Research **19**(7): 1974-1989.

Shirakawa, H. (2001). "The discovery of polyacetylene film: The dawning of an era of conducting polymers (Nobel lecture)." Angewandte Chemie-International Edition **40**(14): 2575-2580.

Shtein, M., J. Mapel, et al. (2002). "Effects of film morphology and gate dielectric surface preparation on the electrical characteristics of organic-vapor-phase-deposited pentacene thin-film transistors." Applied Physics Letters **81**(2): 268-270.

Sirringhaus, H., P. J. Brown, et al. (1999). "Two-dimensional charge transport in self-organized, high-mobility conjugated polymers." Nature (London) **401**(6754): 685-688.

Sirringhaus, H., T. Kawase, et al. (2000). "High-resolution inkjet printing of all-polymer transistor circuits." Science **290**(5499): 2123-2126.

Smith, T. J. and K. J. Stevenson Rev. Sci. Instrum. in preparation.

Sohnchen, S., S. Lukas, et al. (2004). "Epitaxial growth of pentacene films on Cu(110)." Journal of Chemical Physics **121**(1): 525-534.

Stohr, J. (1992). NEXAFS Spectroscopy. Berlin, Springer.

Stohr, J. and D. A. Outka (1987). "Determination of molecular orientations on surfaces from the angular dependence of near-edge x-ray-absorption fine-structure spectra." Physical Review B: Condensed Matter and Materials Physics **36**(15): 7891-905.

Street, R. A., D. Knipp, et al. (2002). "Hole transport in polycrystalline pentacene transistors." Applied Physics Letters **80**(9): 1658-1660.

Street, R. A. and A. Salleo (2002). "Contact effects in polymer transistors." Applied Physics Letters **81**(15): 2887-2889.

Sun, L. and S. C. Yang (1992). "Template-guided Synthesis of Conducting Polymers - Molecular Complex of Polyaniline and Polyelectrolyte." Polymer Preprints **33**: 379.

Sze, S. M. (1981). Physics of Semiconductor Devices. New York, John Wiley & Sons, Inc.

Teoh, R. L., K. B. Guice, et al. (2006). "Atom transfer radical copolymerization of hydroxyethyl methacrylate and dimethylaminoethyl methacrylate in polar solvents." Macromolecules **39**(25): 8609-8615.

Tolstoy, V. P., I. V. Chernyshova, et al. (2003). Handbook of Infrared Spectroscopy of Ultrathin Films, John Wiley & Sons, Inc.

Venables, J. A., G. D. T. Spiller, et al. (1984). "Nucleation and Growth of Thin-Films." Reports on Progress in Physics **47**(4): 399-459.

Xia, Y., M. Mrksich, et al. (1995). "Microcontact Printing of Octadecylsiloxane on the Surface of Silicon Dioxide and Its Application in Microfabrication." Journal of the American Chemical Society **117**(37): 9576-9577.

Xia, Y. and G. M. Whitesides (1998). "Soft lithography." Angewandte Chemie, International Edition **37**(5): 550-575.

Xia, Y. N., J. M. Wiesinger, et al. (1995). "Camphorsulfonic Acid Fully Doped Polyaniline Emeraldine Salt - Conformations in Different Solvents Studied by an Ultraviolet-Visible near-Infrared Spectroscopic Method." Chemistry of Materials **7**(3): 443-445.

Xing, K. Z., M. Fahlman, et al. (1997). "The electronic structure of poly(3,4-ethylene-dioxythiophene): studied by XPS and UPS." Synthetic Metals **89**(3): 161-165.

Yagi, I., K. Tsukagoshi, et al. (2005). "Modification of the electric conduction at the pentacene/SiO2 interface by surface termination of SiO2." Applied Physics Letters **86**(10): 103502.

Yang, D. L., P. N. Adams, et al. (2006). "Impact of hydrogen bonds in polyaniline. AMPSA(n)/acid solutions." Synthetic Metals **156**(18-20): 1225-1235.

Yang, H., T. J. Shin, et al. (2005). "Conducting AFM and 2D GIXD Studies on Pentacene Thin Films." Journal of the American Chemical Society **127**(33): 11542-11543.

Ye, R., M. Baba, et al. (2003). "Growth conditions effects on morphology and transport properties of pentacene thin films." Molecular Crystals and Liquid Crystals **407**: 543-551.

Yoo, J. E., J. L. Cross, et al. (2007). "Improving the electrical conductivity of polymer acid-doped polyaniline by controlling the template molecular weight." Journal of Materials Chemistry **17**(13): 1268-1275.

Yue, J. and A. J. Epstein (1991). "Xps Study of Self-Doped Conducting Polyaniline and Parent Systems." Macromolecules **24**(15): 4441-4445.

Zarras, P., N. Anderson, et al. (2003). "Progress in using conductive polymers as corrosion-inhibiting coatings." Radiation Physics and Chemistry **68**(3-4): 387-394.

Zheng, W., M. Angelopoulos, et al. (1997). "Experimental evidence for hydrogen bonding in polyaniline: Mechanism of aggregate formation and dependency on oxidation state." Macromolecules **30**(10): 2953-2955.

Zuppiroli, L., M. N. Bussac, et al. (1994). "Hopping in Disordered Conducting Polymers." Physical Review B **50**(8): 5196-5203.

Vita

Kwang Seok Lee was born on April 17, 1973, in Seoul, Korea, the second son of Young Ho Lee and Hye Sook Jeon. He graduated from Kwangnam High School in 1992, completed his 26-month military service in 1996 while an undergraduate student at Konkuk University, and earned his Bachelor of Science degree in Textile Engineering in 1999. Upon graduation, Kwang Seok enrolled in the master's program at Seoul National University where he researched short-fiber reinforced polymer composites under the supervision of Professor Jae Ryoun Youn. He was awarded a Master's of Science degree in Materials Science and Engineering in 2001 and a year later, in 2002, Kwang Seok and Jinhee Hwang, members of the same church, were married. Soon afterwards, Kwang Seok entered the Ph.D. program in Chemical Engineering at the University of Texas at Austin where he researched a water-dispersible, conductive polyaniline for organic electronics under the supervision of Professor Yueh-Lin Loo. Upon completion of his doctorate degree, Kwang Seok will begin work with Intel Corporation in Hillsboro, Oregon.

Permanent address: 141-35 Junggok 2dong, Gwangjin-gu, Seoul, Republic of Korea
This dissertation was typed by Kwang Seok Lee.